

ISSN 0377-9416



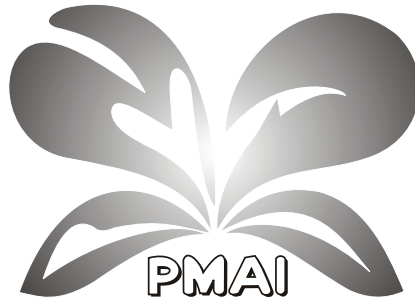
www.pmai.in

TRANSACTIONS OF POWDER METALLURGY ASSOCIATION OF INDIA

Vol. 41 No.2, December 2015

Chief Editor - P. Ramakrishnan

ISSN 0377-9416



www.pmai.in

Vol. 41 No.2, December 2015

Chief Editor - P. Ramakrishnan



Powder Metallurgy Association of India

Office Bearers

President

Shri N. Gopinath

Vice President

Shri Deepak Grover
Shri Narendra Dhokey
Shri Rajendra Sethiya

General Secretary

Dr. Deep Prakash

Hon. Treasurer

Dr. Murli Gopal Krishnamoorthy

Joint Secretary

Shri Aniket Gore
Shri Rajat Varshney



Chief Editor

Prof. Ramakrishnan P.

Editorial Advisory Board

Dr. Ashok S.

Mr. Chandrachud N.L.

Dr. Rama Mohan T. R.

Editorial Board

Dr. Appa Rao G.

Dr. Bhargava Parag

Dr. Dabhade Vikram

Dr. Deep Prakash

Dr. Dhokey N.B.

Dr. Kumar Y.V.S.

Dr. Malobika Karanjai

Dr. Murli Gopal K.

Dr. Panigrahi B.B.

Dr. Sastry I.S.R.

Dr. Tarasankar Mahata

Published by :

Powder Metallurgy Association of India (PMAI)

1002, B-Wing, Kingston, High Street, Hiranandani Complex, Powai, Mumbai - 4000076.

Tel. : +9122 25704588

E-mail : info@pmai.in

Neither the Powder Metallurgy Association of India nor the editor assumes responsibility of opinions expressed by the authors of the papers published in this transaction.

Editorial



This issue of Trans. PMAI. Vol. 41. No.2., contain selected papers from the Intl.PM-15 held at I.I.T., Bombay. First three articles are dealing with the milling of powders and their influence on phase formation to produce high entropy alloy powders, ternary nano structured magnetic alloy powders and ultrafine particles of MAX phases. Following three papers are on the investigation on PM aluminum alloys. Microwave sintering of Al-Mn-Cu alloys have resulted in the improved structure and properties. The compaction and sintering of Al-Si-Cu-Mg-Zn-Fe alloys in pure nitrogen atmosphere have demonstrated the evolution of distinct phases leading to liquid phase sintering. The development of aluminum-nano silicon carbide composites by mechanical alloying, cold isostatic pressing and sintering in argon atmosphere followed by the evaluation of mechanical properties is the subject matter of the third paper. Tribological properties of Fe-P powder metallurgy alloys have been investigated in the next article. The addition of phosphorus in the form of iron phosphate to atomized iron powder resulted in higher density and tribological properties.

This is followed by the development of β Ti_xNb alloys suitable for orthopedic implants, using first principle calculations followed by processing the same by powder metallurgy. Next paper deals with the virtual molding of powder injection molding components using SIGMASOFT(R) software tool to ensure green part quality. This will enable to serve the interest of powder injection molding industry involving several features and material models which improve the reliability and accuracy of the flow and thermal behavior predicted. The article on the investigation on charge carrier reversals in lead modified chalcogenide glasses suggest that the important properties could be related to chemical bonding and network topology of the glass. Using submicron alumina fabrication of parts by micro stereo lithography by different layer recoating techniques have been discussed in the next paper. The effect of viscosity of Titania paste and screen printing parameters on the morphology of printed film has been studied with a view to use in dye sensitized solar cells.

Indian nuclear power program, pressurized heavy water reactor uses natural UO₂ pellets as its fuel material. To improve the recovery of the pellets, ammonium diuranate calcined U₃O₈ additives are used and their effect on the UO₂ pellets characteristics have been investigated. The concluding paper is on the effect of Zinc doping at Cu²⁺ site in Y_{2/3} Cu Ti₄O₁₂ ceramic which are used in various microelectronic devices. YCZTO ceramics have been synthesized by semi wet method and the microstructural studies and dielectric measurements indicated their superior properties.

P. Ramakrishnan.

TRANSACTIONS OF
POWDER METALLURGY ASSOCIATION OF INDIA

Vol. 41 No.2, December 2015

CONTENTS

| | |
|---|-------|
| 1. SYNTHESIS OF FeCrCoMnNi HIGH ENTROPY ALLOY POWDERS BY MECHANICAL ALLOYING Ashif Equbal, Rahul B. Mane, Bharat B. Panigrahi | 1-5 |
| 2. PHASE TRANSFORMATION, NANOSTRUCTURAL AND MAGNETIC PROPERTIES OF TERNARY AlCuFe ALLOY POWDER M.M. Rajath Hegde, Pradeep N, Bharath Kumar, Tenzin Pasang | 6-12 |
| 3. PHASE EVOLUTION DURING SYNTHESIS OF Ti ₃ Si ₂ POWDER THROUGH MECHANICAL ALLOYING Rahul B. Mane, Y. Rajkumar, Bharat B. Panigrahi | 13-17 |
| 4. PROCESSING AND EVALUATION OF ALUMINIUM Mn – Cu ALLOY THROUGH POWDER METALLURGY Arunkumar S, Sathish kumar M, Chandan Byral R, S. Kartikeyan | 18-27 |
| 5. INFLUENCE OF PROCESS CONDITION ON SINTERABILITY OF A PREMIX Al-Si ALLOY A. A. Methe, N. B. Dhokey | 28-35 |
| 6. DEVELOPMENT OF Al-NANO SiC COMPOSITES THROUGH POWDER METALLURGY ROUTE AND TESTING THEIR MECHANICAL PROPERTIES Gaurav Bajpai, Rajesh Purohit, R. S. Rana and Akshat Patil | 36-44 |
| 7. TRIBOLOGICAL PROPERTIES OF Fe-P POWDER METALLURGY ALLOYS Shailesh Kumar Chaurasia, Ujjwal Prakash, Vikram Dabhade | 45-50 |
| 8. DEVELOPMENT OF β Ti-xNb ALLOYS THROUGH FIRST-PRINCIPLES DFT ANALYSIS AND P/M ROUTE FOR ORTHOPEDIC IMPLANTS Rajamallu K, Manish K. Niranjan, Suhash Ranjan Dey | 51-54 |
| 9. VIRTUAL MOLDING OF PIM COMPONENTS Mohamed Ismail Khan, Raman Kumar Jayabalant | 55-60 |
| 10. CHARGE CARRIER REVERSAL IN LEAD MODIFIED CHALCOGENIDE GLASSES Akhyaya K. Pattanaik | 61-63 |
| 11. FABRICATION OF CERAMIC PARTS BY CERAMIC MICROSTEREOLITHOGRAPHY BY DIFFERENT LAYER RECOATING TECHNIQUES Chandrashekar Adake, Prasanna Gandhi, Parag Bhargava | 64-67 |
| 12. SCREEN PRINTING OF DYE SENSITIZED SOLAR CELLS Venumadhav More, Bheem Singh, Parag Bhargava | 68-76 |
| 13. STUDY ON EFFECT OF ADU CALCINED U ₃ O ₈ ADDITIVE ON UO ₂ PELLET CHARACTERISTICS N. Santra, T. K. Sinha, A. K. Singh, D. S. Setty, G. Kalyana Krishnan, N. Saibaba | 77-81 |
| 14. EFFECT OF ZINC DOPING AT Cu ²⁺ - SITE IN Y _{2/3} Cu ₃ Ti ₄ O ₁₂ CERAMIC SYNTHESIZED BY SEMI-WET ROUTE Sunita Sharma, K. D. Mandal | 82-87 |

SYNTHESIS OF FeCrCoMnNi HIGH ENTROPY ALLOY POWDERS BY MECHANICAL ALLOYING

Ashif Equbal, Rahul B. Mane and Bharat B. Panigrahi

Department of Materials Science and Metallurgical Engineering
Indian Institute of Technology Hyderabad, India.

Abstract

High entropy alloys (HEAs) are solid solution of five or more than five elements together in equi-atomic or near equi-atomic composition. These HEAs are having high hardness, high strength and better ductility than conventional superalloys. These can be fabricated through two processing routes, melting casting and mechanical alloying (MA). Objective of this research is to synthesize the high purity single phase FeCrCoMnNi HEA powder through high energy ball milling route and to study the phase stability during sintering. Elemental powders of Fe, Cr, Co, Mn, and Ni were taken in equi-molar ratio and milled up to 40 h using tungsten carbide vials and balls. XRD of milled powders indicate that alloy phase formation starts at 10 h of milling. Alloy with FCC structure was present as major phase. Milled powders were further subjected to thermal treatment and to understand the phase formation behaviour during heating, the powders were analyzed using Differential Scanning Calorimetry (DSC). DSC analysis indicates that the exothermic reactions occurred at 400°C and 800°C, which could be attributed to alloy formation. Post-mechanical alloying annealing treatment at 800°C showed that the XRD peaks have become sharper and intense. Alloy formation was further compared with x-ray diffraction patterns of as-cast HEA of same composition and results were very similar.

Keywords: High-entropy alloys, Mechanical alloying, sintering, annealing

Introduction

The conventional alloy design concept is essentially centered on using one principal element to which other alloying elements are added for improving desired properties [1,2]. Recently, a new alloy design concept has been introduced for developing novel materials which are equiatomic or near equiatomic multicomponent alloys having at least five elements such as High-entropy alloys (HEAs), emerge as novel metallic materials with great potential to be used as high temperature materials, or coating materials requiring high hardness and high wear resistance.[1,4,8]. The research and development of high entropy alloys have been started since 1990s. HEAs by definition contain five or more major metal elements, each at over 5 at% but less than 35

at% [1-7]. These alloys are defined as HEAs by Yeh [8] and named by Cantor [1] as multi-component alloys. Both refer to the same concept. There are also some other names, such as multi-principal-elements alloys, equi-molar alloys, equi-atomic ratio alloys, substitutional alloys, and multi-component alloys. Although being highly concentrated multi-component alloy systems, simple solid solutions tend to form in HEAs, with the absence of intermetallic compounds [10]. This seemingly unexpected phenomenon is partly due to the significant entropic contribution, which lowers the Gibbs energy of the solid solution phases at elevated temperatures [2]. Normally, the formed solid solutions in HEAs are of FCC and/or BCC structures [2]. How to simultaneously achieve both high strength and high tensile ductility in HEAs is a great challenge in the field, and this

SYNTHESIS OF FeCrCoMnNi HIGH ENTROPY ALLOY POWDERS BY MECHANICAL ALLOYING

constitutes the main interest of this research group. Because of the effect of high entropy, solid solutions with multi principal elements tend to be more stable, The multi-component equi-molar alloys should be located at the center of a multi-component phase diagram, and their configuration entropy of mixing reaches its maximum ($R \ln N$; where R is the gas constant and N the number of component in the system) for a solution phase [2]. Cantor [1] pointed out that a conventional alloy development strategy leads to an enormous amount of knowledge about alloys based on one or two components, but little or no knowledge about alloys containing several main components in near-equal proportions. Theoretical and experimental works on the occurrence, structure, and properties of crystalline phases have been restricted to alloys based on one or two main components. The mechanical behaviour of HEAs are greatly affected by the phase constitutions in that generally FCC-typed HEAs are ductile but soft, while the BCC-typed HEAs are hard but brittle [2,11-15] HEAs reportedly exhibit promising properties, such as high strength, good oxidation and corrosion resistance, superior temper-softening resistance, and excellent abrasive wear resistance. [1,2,15] These unique properties of this HEA may have potential for future aerospace applications. Other than the structural properties some combinations of HEAs show some good magnetic properties such as FeCrCoMnNi. W. Ji et al. [7] reported that FeCrCoMnNi shows higher saturated magnetizations and lower remittance ratio.

Typical processing routes for HEAs can be summarized according to the starting states for the alloy preparation, mainly: (1) from the liquid state, (2) from the solid state, (3) from the gasstate, and (4) from electrochemical process. Singh et al. carefully studied the decomposition process of the AlCoCrCuFeNi HEA in arc-melting route and they found

that a high cooling rate tended to promote formation of a single phase [15]. High cooling rates favored the formation of polycrystalline phases with a size of few nanometers [2]. Synthesis of this HEA through arc melting route has its own limitations on controlling the microstructure and grain growth of the alloy. However, relatively low cooling rates led to the formation of typical dendritic and interdendritic microstructures due to elemental segregation. This work clearly demonstrated that for certain "HEAs", a single solid-solution phase can only form at relatively high cooling rates, and their high-entropy state is valid in a metastable condition. Annealing at elevated temperatures or using slow cooling rates induces the formation of multiple phases, resulting in a dramatic reduction in the configurational entropy of mixing due to elemental partitioning among these phases [2]. To overcome these limitations in fabrication of HEA mechanical alloying route has been adopted. Mechanical alloying method is known for its capability for extending the solid solubility limits and making the alloys of those metals which are difficult to form through conventional method. Also in mechanical alloying we can have the control on the grain size of the alloys by changing the different milling parameters. FeCrCoMnNi HEA is one of the initial high entropy alloys which were reported as a single phase and produce through melting casting route. It attracted attention of researchers because of very unique property of high hardness, fracture toughness and high wear resistance. Main objective of this work is to prepare single phase HEA only by mechanical alloying of the Fe-Cr-Co-Mn-Ni equi-atomic composition and study the alloying behavior. Since the powder has to go under sintering process for making components, which is carried out at elevated temperature it is essential to understand the stability of the phase during sintering process.

SYNTHESIS OF FeCrCoMnNi HIGH ENTROPY ALLOY POWDERS BY MECHANICAL ALLOYING

Experimental Procedure

Fe, Cr, Co and Mn powder with mesh of size -325 and about 99% purity were procured from Alfa Aesar and nickel powder with mesh size of -325 and about 99.5% purity was procured from Sigma-Aldrich. All elemental powders were characterized by XRD to conform its purity and phase. Powders were taken in equimolar ratio and then these powders were kept in high energy planetary ball mill system (Fritsch P-5) for mechanical alloying. The vials and ball were made of tungsten carbide. Toluene was used as a process control agent to overcome oxidation of powder and to minimize the heat generation. Ball to powder weight ratio was taken as 10:1 and at a speed of 300 rpm. Some amount of milled powders was taken out at regular intervals of 10 h, 20 h, 30 h and 40 h of milling for characterization and other studies. After mechanical alloying of HEA powder, they have been taken for XRD using X-ray diffractometer (PANalytical, Model: X'Pert PRO) with Cu $\kappa\alpha$ radiation of wavelength 1.54Å as a source. DSC of 30 h and 40 h milled powder have been done up to 1400°C while heating at a rate of 20°C min⁻¹ to study the phase formation. Consequently after DSC result heat treatment were performed at 400°C and 800°C and 1100°C for all the milled HEA samples to study the phase formation. Also the effect of cooling rate after heat treatment was also studied: i.e. alloyed powder was heated to 1150°C followed by cooled in the furnace and another case quenched to room temperature. Behaviour of mechanically alloyed powder was compared with the as-cast FeCrCoMnNi HEA (received from NTHU, TAIWAN) under similar conditions.

Results

Milled powders were extensively characterized using XRD and DSC analysis. Fig. 1 shows the XRD patterns of the milled powders collected for 10 h. Alloy seems to be forming in 10 h of milling. Four strongest peaks were found to be identical to the pure nickel system

representing the (111), (200), (220) and (311) planes, a characteristics of FCC structure. Lattice parameter of 10 h milled FeCrCoMnNi powder were calculated using formula

$$a^2 = \frac{\lambda^2(h^2+k^2+l^2)}{(2\sin\theta)^2}$$

which is found to be equal to 3.59Å that is greater than the lattice parameter of nickel (3.52Å). Few smaller peaks identical to (310) and (222) planes and similar to the pure manganese metal, could be representing the BCC structure.

The trend observed for 10 h during XRD profile, remain same for 20h milled powder also. However, when the milling time is increased to 30 and 40 h (Fig. 2), phase formation sequence seems to be destabilized. The peaks belong to FCC remained there but peaks of other phases have also emerged. The phase stability of mechanically alloyed powder was characterized through the DSC analysis, which has been shown in Fig. 3.

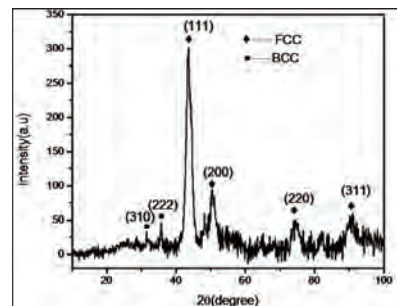


Fig 1: 10hours milled FeCrCoMnNi powder

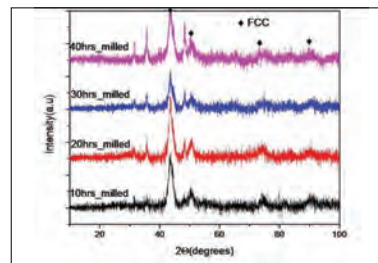


Fig 2: 10, 20, 30 and 40hours ball milled FeCrCoMnNi powder

SYNTHESIS OF FeCrCoMnNi HIGH ENTROPY ALLOY POWDERS BY MECHANICAL ALLOYING

The exothermic peaks were observed at 400 and 800°C. The exothermic peak at 400°C may be attributed to the two phenomena: the release of internal strains and activated reaction of milled elements. The peak at 800°C may be related to the major reaction which yields high entropy alloy phase of FeCrCoMnNi from the partially reacted and mechanically activated phases. At high temperature of about 1250°C, an endothermic peak was observed in the milled powder. This endothermic peak is an indication of melting of alloy. To understand the effect of heating rate on the reaction patterns, i.e. nature of exothermic peaks and their occurrence, DSC runs were carried out at various heating rates (Fig. 3). During very slow heating ($5^{\circ}\text{C min}^{-1}$), the exothermic peaks intensities decreased significantly. On the other hand, the intensity of endothermic peaks, i.e., the quantity of heat absorption seems to be increased significantly with increasing heating rate.

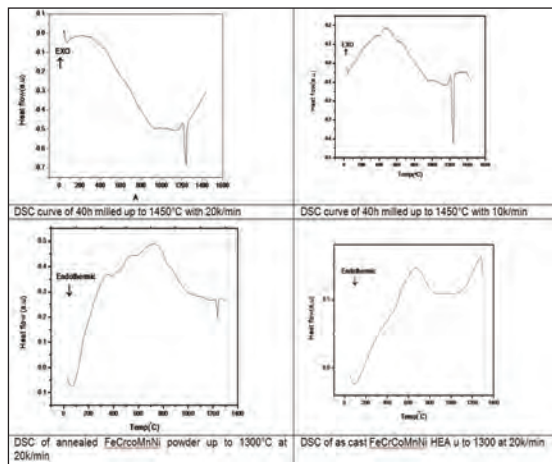


Fig. 3 DSC of FeCrCoMnNi powder and as cast FeCrCoMnNi HEA at different heating rate

Fig. 4 and 5 show the XRD profiles of heat treated alloyed powders at 400 and 800°C. During the heat treatment major phase remained FCC and seems to be stable at elevated temperatures.

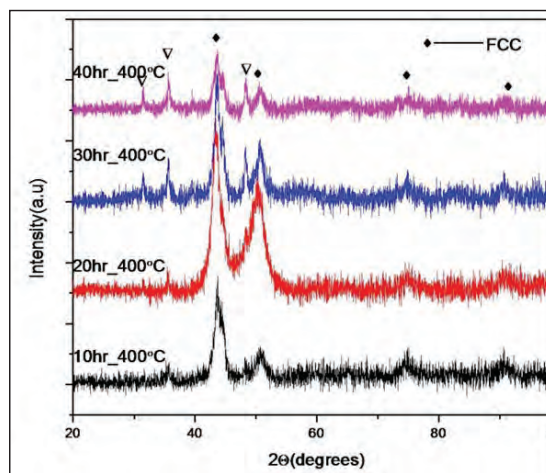


Fig 4 XRD pattern of 10 20 30 40h milled and heated at 400°C

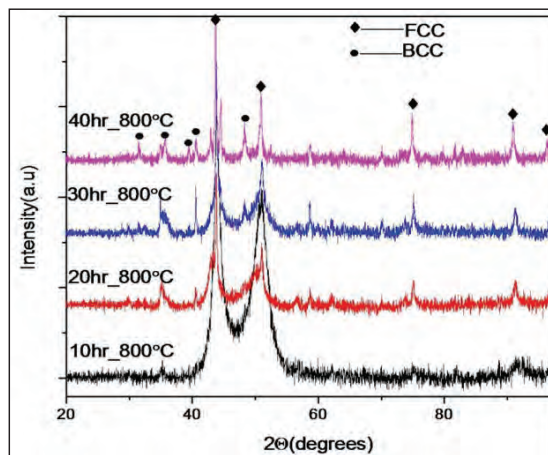


Fig 5 XRD pattern of 10 20 30 40h milled and heated at 800°C

Fig. 6 shows the 30 h and 40 h milled powder heated to 1150°C and quenched to room temperature. It can be seen (Fig. 6) that the quenched sample shows less number of secondary peaks (i.e. secondary phases) compared to furnace cooled samples (Fig. 4 - 5). In fact, peaks other than FCC phase, seem to be the BCC peaks only.

SYNTHESIS OF FeCrCoMnNi HIGH ENTROPY ALLOY POWDERS BY MECHANICAL ALLOYING

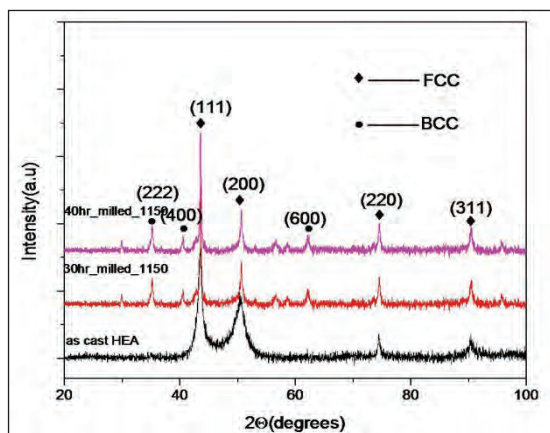


Fig. 6 XRD pattern of 30, 40 h milled and quenched at 1150°C and as cast FeCrCoMnNi HEA

All the above XRD profiles and DSC profiles were further compared with that of the as-cast high entropy alloy (XRD profile of the same, could be seen in Fig. 6. Interestingly, the phase observed during mechanical alloying was similar to that of as-cast alloy.

Conclusion

This work successfully synthesized the FeCrCoMnNi high entropy alloy by mechanical alloying of elemental powders. Prepared alloy powder has FCC structure with very small amount of other phases. The activated reactions, which are exothermic in nature, were observed during heating, further attributed to the phase formation sequences from partially reacted stage.

Acknowledgements:

The SERB-DST (Govt. of India) is gratefully acknowledged for providing the financial support. Authors wish to thank to Dr. Pinaki P. Bhattacharya for useful discussions.

References

[1] B. Cantor, I.T.H. Chang, P. Knight, A.J.B. Vincent *Materials Science and Engineering A* 375-377 (2004) 213-218.

[2] Yong Zhang, Ting Ting Zuo, Zhi Tang, Michael C. Gao, Karin A. Dahmen, Peter K. Liaw, Zhao Ping Lu, *Progress in Materials Science* 61 (2014) 1-93.

[3] P.P. Bhattacharjee, G.D. Sathiaraj, M. Zaid, J.R. Gatti, Chi Lee, Che-Wei Tsai, Jien-Wei Yeh *Journal of Alloys and Compounds* 587 (2014) 544-552.

[4] J.W. Yeh, S.K. Chen, S.J. Lin, J.Y. Gan, T.S. Chin, T.T. Shun, C.H. Tsau, S.Y. Chang, *Adv. Eng. Mater.* 6 (2004) 299-303.

[5] Fan Yuhu, Zhang Yunpeng, Guan Hongyan, Suo Huimin, He Li *Rare Metal Materials and Engineering*, 2013, 42(6): 1127-1129.

[6] S. Praveen, B.S. Murty, R.S. Kottada, *Mater. Sci. Eng. A* 534 (2012) 83-89.

[7] Wei Ji, Weimin Wang, Hao Wang, Jinyong Zhang, Yucheng Wang, Fan Zhang, Zhengyi Fu *Intermetallics* 56 (2015) 24-27.

[8] Yeh JW. Recent progress in high-entropy alloys, *Ann ChimSci Mat* 2006;31:633-48.

[9] C Suryanarayana, E Ivanov, VV Boldyrev. The science and technology of mechanical alloying. *Mater Sci Eng A* 2001;304-306:151-8.

[10] Li Q, Wang G, Song XP, Fan L, Hu WT, Xiao FR, et al. Ti₅₀Cu₂₃Ni₂₀Sn₇ bulk glasses prepared by mechanical alloying and spark-plasma sintering. *J Mater Process Tech* 2009;209:3285-8

[11] Fu ZQ, Chen WP, Xiao HQ, Zhou LW, Zhu DZ, Yang SF. Fabrication and properties of nanocrystalline Co_{0.5}FeNiCrTi_{0.5} high entropy alloy by MA-SPS technique. *Mater Des* 2013;44:535-9.

[12] S Ranganathan. Alloyed pleasures: multimetallic cocktails. *CurrSci* 2003;8:1404-6.

[13] S.G. Chowdhury, S. Datta, B.R. Kumar, P.K. De, R.N. Ghosh, *Mater. Sci. Eng. A* 443 (2007) 114-119.

[14] P.K. Huang, J.W. Yeh, *Scr. Mater.* 62 (2) (2010) 105-108.

[15] Singh S, Wanderka N, Murty BS, Glatzel U, Banhart J. Decomposition in multi-component AlCoCrCuFeNi high-entropy alloy. *Acta Mater* 2011;59:182-90.

PHASE TRANSFORMATION, NANOSTRUCTURAL AND MAGNETIC PROPERTIES OF TERNARY AlCuFe ALLOY POWDER

M.M. Rajath Hegde, Pradeep N, Bharath Kumar, Tenzin Pasang

JNNCE Shimoga, VTU, INDIA

Sahyadri College of Engineering and Management, Adyar Mangalore, INDIA

Abstract

Mixture of elemental powders of Al, Cu and Fe are mechanically alloyed in a planetary ball mill. The initial composition of the powder selected was $Al_{70}Fe_{20}Cu_{10}$ atomic percent. Ball milling induces the formation of ternary alloy (Al(Cu,Fe) of orthorhombic structure) as well as binary alloy (AlCu of monoclinic structure) solid solutions at 15 hours of ball milling time. Further, intermetallic phase (Al_4Cu_9) of cubic structure is formed at the end of 30 hours of ball milling time. Solubility of Fe in Al is limited to a large extent compared to the solubility of Cu in Al. Thus, due to increased onslaught of plastic deformation by ball milling, Fe rebounds back to elemental form at the end of 30 hours of ball milling time. Ball milled powders have been characterized by scanning electron microscopy (SEM) and transmission electron microscopy (TEM) and the analysis has been correlated with that of X-ray diffraction (XRD). Magnetization decreases with increase in ball milling time. However, transition of solid solution to intermetallic phase with increase in temperature causes ferromagnetic to paramagnetic transition.

Key words: ball milling; mechanical alloying; Al-Cu-Fe; nanostructured; magnetization

Introduction

In the last 10 years, Al based intermetallics have become an object of intensive study due to their unusual properties and a considerable promise for possible applications [1-4]. Among all the mechanically alloyed Al-Cu-Fe systems, $Al_{70}Cu_{20}Fe_{10}$, $Al_{65}Cu_{20}Fe_{15}$ and $Al_{63}Cu_{25}Fe_{12}$ are the most extensively studied [5-8], because it is easy to produce them, are nontoxic and thermally stable and they are resistant to oxidation. In addition, their alloying elements are inexpensive. Such ternary alloys are used in aircraft and defense applications as soft and hard magnetic materials. Although mechanical alloying (MA) has been established as a simple viable solid-state processing route for the synthesis of metastable alloys, very few studies have reported the phase formation

of stable Al-Cu-Fe alloy [5]. Synthesis of intermetallic phase is of prime importance, especially with respect to application and superior properties possessed by such an ordered material. Mechanical properties of Al-Cu-Fe intermetallics are comparable to that of diamonds and some ceramics. Although mechanical alloying (MA) has been established as a simple viable solid-state processing route for the synthesis of metastable quasicrystalline alloys, very few research articles have reported the formation of different phases and structure during ball milling of elemental Al, Cu and Fe. However, there is hardly any research article which reports on the characterization of ball milling of elemental powders of Al, Cu and Fe with an initial composition of $Al_{70}-Cu_{10}-Fe_{20}$ atomic percent each.

PHASE TRANSFORMATION, NANOSTRUCTURAL AND MAGNETIC PROPERTIES OF TERNARY AlCuFe ALLOY POWDER

In the present investigation, we examine the formation of different phases as a consequence of mechanical alloying. Characterization during every stage of ball milling has been done by XRD, SEM, TEM and VSM.

Experimental

Mechanical alloying is achieved by high energetic planetary ball milling (Fig. 1 a) of elemental powders of Al, Cu and Fe powders. Ball milling was carried out for a maximum duration of 30 hours and to avoid contamination from the atmosphere, milling process was carried out in a toluene fluid media. Characterization was carried out at every stage of ball milling process. Characterization techniques like XRD (Fig. 1 b), SEM, TEM and vibrating sample magnetometer (VSM) (Fig. 1 c) were utilized to explore phase identification, composition, morphology, topography and magnetic properties. Magnetic analysis was done at room temperature as well as at elevated temperature too. Powder particles were suspended in ethanol solution, further carbon coated Cu grid (200 to 300 mesh) was utilized to hold powder taken out of ethanol, it is dried before inserting into the TEM sample chamber.

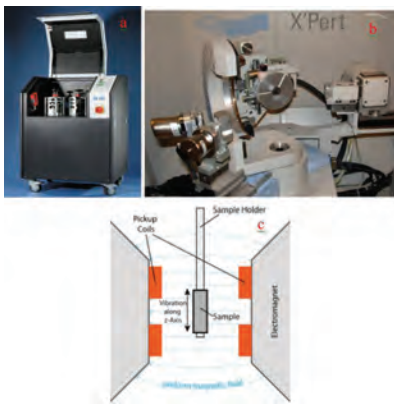


Fig. 1 a) high energetic ball mill (Retsch PM 400), b) X-ray diffractometer (Cu Ka) and c) vibrating sample magnetometer

Results and Discussions:

XRD profiles are shown in Fig. 2

Unmilled powder sample show the following inferences:

- 1) Relative intensity of Al (111) is highest among the diffraction peaks in the profile; the peak possesses a height of 370 counts and with an integrated intensity of 161353.2086.
- 2) Certain Al/Fe diffraction peaks have been superimposed at certain Bragg angles, such diffraction peaks are; 200Al/110Fe, 220Al/200Fe, 222Al/211Fe and 400Al/220Fe.
- 3) In addition, individual diffraction peaks of Al (111, 311) and Cu (111, 200, 220 and 311) are observed in the XRD profile.
- 4) Elemental phases of Al, Cu and Fe have been identified quantitatively in the XRD profile and also qualitatively by indexing as shown in the table 1.
- 5) Mixture of elemental powders of Al, Cu and Fe possessed lattice parameters of 0.4044 nm, 0.3619 nm and 0.2862 nm respectively.
- 6) Integrated intensity of Cu (111) is highest among the ingredients in the mixture of elements.

Elemental powder subjected to 15 hours of ball milling duration show the following inferences

- 1) Compared to the XRD profile of unmilled mixture of elemental powders, Al (111 and 311) diffraction peaks have been reduced in relative intensities with a height of 327 counts and 89 counts respectively.
- 2) Such reduction in the diffraction peak height is due to the diminishing of Al phase and the formation of Al rich solid solution.

PHASE TRANSFORMATION, NANOSTRUCTURAL AND MAGNETIC PROPERTIES OF TERNARY AlCuFe ALLOY POWDER

- 3) The superimposed diffraction peaks of Al/Fe have been broadened and have become slightly asymmetric in shape. Such change in the physical shape of the peaks has caused an emergence of new peaks slightly to the left (lower Bragg angles) of superimposed peaks. The newly emerged diffraction peaks are due to the formation of solid solution phases at the expense of elemental phases[5].
 - 4) The solid solution phase formed is of two types, one, binary solid solution of AlCu of monoclinic structure. While, the other is ternary alloy of Al(Cu,Fe) of orthorhombic type.
 - 5) The lattice parameter of Al (222) expands to 0.4057 nm from 0.4044 nm of elemental phase, the expansion is mainly due to diffusion of Cu and Fe atoms into Al lattice.
 - 6) However, elemental phases of Al and Fe are still visible in the XRD profile; it seems that the lower solubility and diffusivity of Fe than Cu in Al is responsible for this effect.
 - 7) Even unalloyed Cu phase is visible but with a decreased relative intensity and integrated intensity of 129.50 counts and 753866.7627 respectively.
 - 8) Diffusion of Cu in Al is evident from the decrease in lattice parameter of Cu from 0.3622 nm for unmilled to 0.3614 nm for 15 hours milled powder.
 - 9) Thus, the phases that are present at the end of 15 hours of ball milling time are elemental phase of Al, Cu and Fe and solid solution phases of AlCu and Al(Cu,Fe). These phases are shown quantitatively and qualitatively too in the XRD profile and the relevant table respectively.
 - 10) Cu being a very ductile (soft) material, atoms get squeezed into interstitial positions in the solid solution.
- As milling time increases from 15 hours to 30 hours, interesting metallurgical events occur as seen from the XRD profile. Thus, the following inferences could be attained from the XRD profile:
- 1) There is a drastic reduction in the relative intensities of Al (111) and Al/Fe (200/110) diffraction peaks compared to 15 hours of ball milled powder. The intensities are given in terms of height as 127 and 284 counts respectively for 30 hours ball milled powder compared to 327 and 408 counts respectively for 15 hours milled powder.
 - 2) Diffraction peaks (111, 220 and 311) of Cu phase is not visible in the XRD profile, which suggests the vanishing of such a phase in the 30 hours ball milled powder.
 - 3) Such change in the above structural parameters induces the formation of Al₄Cu₉ intermetallic phase of cubic structure.
 - 4) Due to the severe plastic deformation caused by ball milling, ballistic diffusion causes the retracing of Fe atoms from the solid solution (Al(Cu,Fe)) formed at the end of 15 hours of milling time) phase back to elemental phase.
 - 5) Such a type of splitting of solid solution into intermetallic and elemental phase is shown by the expansion of Fe lattice (0.2869 nm) as well as the increase in the integrated intensity (185762.4173) of 200/110 Al/Fe peak
 - 6) Moreover, solubility and diffusivity of Fe in Al is limited to a large extent mainly due to the large difference in the melting points of the two.
 - 7) The macro temperature reached during ball milling could be near room temperature however, the micro temperature could reach upto several hundred degrees.

PHASE TRANSFORMATION, NANOSTRUCTURAL AND MAGNETIC PROPERTIES OF TERNARY AlCuFe ALLOY POWDER

- 8) There is further refinement of grain size (40 nm) and increase in lattice strain (0.443 %) at the end of 30 hours of ball milling time.
- 9) From the above analysis, quantitatively and qualitatively elemental traces of Al and Fe along with intermetallic phase is present at the end of 30 hours of ball milling time.
- 10) Hence, MA could not drive Fe to form CuFe or Al(Cu, Fe) alloy with Cu and Al powders together at the end of 30 hours of milling time. This result is different from previous results (15 hr MA) of mechanically alloyed CuFe alloy that showed that Cu and Fe can easily form metastable alloy solid solution by mechanical alloying [9]. This illustrates that Al atoms in the AlCu alloy prevent Fe from entering the lattice of AlCu alloy.

time. Further, the nano crystalline grains (Fig. 3 b) of Fe and Cu are embedded in the matrix of Al indicating the formation of Al rich solid solution as proved by XRD profile. The nano crystalline grains measured by TEM are in the range of approximately 50 nm, thus XRD crystallite size calculated by scherrer equation is identical with TEM results.

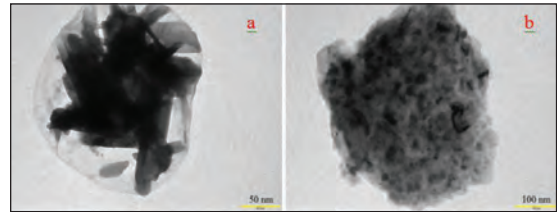


Fig. 3 (a & b) TEM micrographs of mechanically alloyed powders as a function of ball milling duration

Table 1 Structural parameters of unprocessed/ processed elemental powders

| Pos. [2 θ h.] | Unmilled (UM) / milled(M) | hkl phase | FWHM [2 θ h.] | d-spacing [nm] | a lattice parameter nm | D [*] | Strain % | Integrated Intensity |
|----------------------|---------------------------|--------------------------|----------------------|----------------|------------------------|----------------|----------|----------------------|
| 38.4665 | UM | 111(Al) | 0.1585 | 0.23402 | 0.4044 | — | — | 161353.2086 |
| 43.5666 | UM | 111(Cu) | 0.1757 | 0.20499 | 0.3619 | — | — | 75037.4564 |
| 44.7062 | UM | 200Al/110Fe | 0.2517 | 0.20272 | 0.4044@2862 | 60nm | 0.071 | 185443.4285 |
| 50.4518 | UM | 200Cu | 0.3000 | 0.18088 | 0.3417 | — | — | 554625.1189 |
| 38.5673 | 15 hr M | (111)Al (203)Al/Cu/Fe | 0.2655 | 1.55622 | 0.4044 | — | — | 161464.6183 Al |
| 44.7494 | 15 hr M | (200)Al/110Fe | 0.3648 | 1.35010 | 0.4051@0.2864 | 114.5 nm | 0.235 | 184337.1472 |
| 38.5130 | 30 hr M | 111/Al | 0.3911 | 1.55833 | 0.40486 | — | — | 161978.1254 |
| 44.4400 | 30 hr M | Al4Cu9/330 | 0.5062 | 1.35902 | — | 40 nm | 0.443 | 2032963.666 |
| 44.6655 | 30 hr M | 110Fe/200Al | 0.3260 | 1.35251 | 0.2869 | — | — | 185762.4173 |

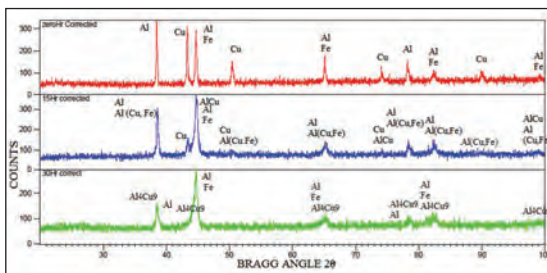


Fig. 2 XRD profiles of unmilled (zero Hr) and ball milled (15 Hr & 30 Hr) powder samples

Transmission Electron Microscopy (TEM):

Transmission electron microscopy (TEM) images (Fig. 3 a) indicate the diffusion of Cu and Fe in Al lattice after 5 hours of ball milling

Room Temperature Magnetization:

Room temperature magnetization curves are in the form of hysteresis loop as shown in Fig. 4 for various ball milled powder samples. VSM is utilized in obtaining the loops and curves. From these magnetization results, we can infer the following discussions:

- 1) Unmilled powder (0 hour) samples exhibits highest MS (148.9 emu/gms) mainly due to the presence of unalloyed elemental Fe, as pure Fe is ferromagnetic.
- 2) MS decreases upon increase in ball milling duration, such change in magnetization is due to progressive alloying. Formation of solid solution (alloy formation) has been proved by XRD and electron microscopy results. The decrease of MS is in the range of 41.79 to 54.96 emu/gms.
- 3) For all the ball milled powder samples, HC is less than 125.664 Oe, hence these mechanically alloyed powders possess soft magnetic properties.

PHASE TRANSFORMATION, NANOSTRUCTURAL AND MAGNETIC PROPERTIES OF TERNARY AlCuFe ALLOY POWDER

- 4) HC (104.249 Oe) is highest for 30 hours ball milled powder sample compared to all other ball milled powder. Such an increase in HC is due to the finer grain size (40 nm) observed in the 30 hour ball milled powder.
- 5) Narrow hysteresis loops (Fig) is shown for all the ball milled powder samples, which indicate soft ($HC < 125.66$ Oe) magnetic properties.
- 6) Least MS is observed in 10 hour ball milled powder, while all the other ball milled powders show a marginal increase in MS due to the formation of solid solution/intermetallic ((Al(Fe Cu))/(Al₄Cu₉)) phases and Fe solubility limit in Al lattice.

Elevated Temperature Magnetization:

Magnetization of ball milled powders have been obtained at different temperatures (in the range of 25 °C to 800 °C), the curves are shown in the Fig. 5. From these results the following inferences could be drawn:

- 1) Unmilled powder (0 hour) shows ferromagnetic property at elevated temperatures, infact magnetisation increases with increase in temperature. Such a behavior is due to Al melting and dissolution of Cu in Al, while Fe almost remains elemental.
- 2) However, at 640 °C, slight Fe could have diffused into the Al lattice causing Al rich ternary alloy formation along with Cu causing a slight decrease in magnetization.
- 3) Similar is the case with 5 hour ball milled powder, however its room temperature magnetisation is quite low due to progressive alloying of all the elemental phases during ball milling.
- 4) Elemental powders subjected to higher duration (10 to 30 hours) of ball milling shows a transition to intermetallic phase

from solid solution upon heating beyond 400 °C. Intermetallic ternary alloys possesses paramagnetic phase approximately in the temperature range of 500 to 580 °C. Steep decrease in the magnetization is noted for these ball milled powder samples.

- 5) Paramagnetic phase is attained due to progressive alloying of ferromagnetic Fe with nonmagnetic elements like Al and Cu. Thus direct ferromagnetic coupling between Fe-Fe is not possible because of the interference of Al and Cu atoms.

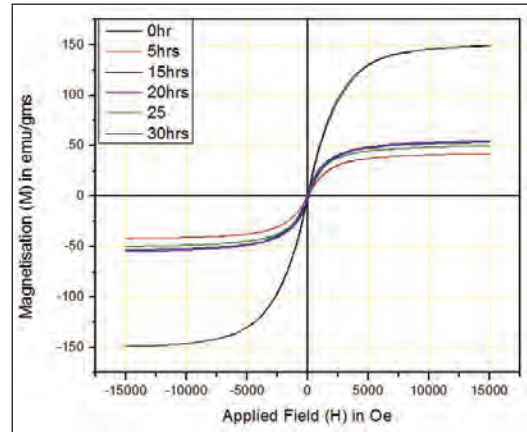


Fig. 4 Room temperature hysteresis curves showing magnetic properties as a function of milling time

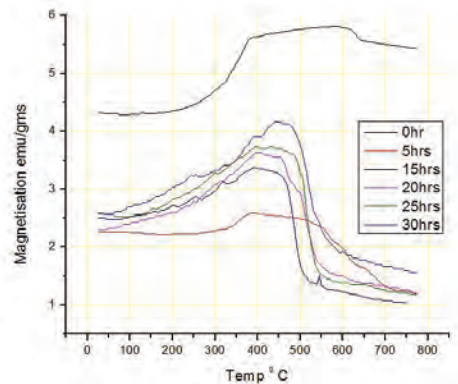


Fig. 5 Thermo magnetic curves as a function of ball milling duration

PHASE TRANSFORMATION, NANOSTRUCTURAL AND MAGNETIC PROPERTIES OF TERNARY AlCuFe ALLOY POWDER

Scanning Electron Microscopy (SEM)

Typical morphology of unmilled and ball milled powders is shown in Fig. 6(a to c), unmilled powders show no welding, deformation and other processing effects. While mixture of elemental powders subjected to ball milling show flattening and layer by layer diffusion. It is similar to pop corn like structure. Fracture of Particle occurs while the size is seen to be reduced with increase in ball milling duration. In Fig. 6 (b), particles are seen to be agglomerated due to welding. Ball milling is a process of repeated welding and fracturing of powder particles as seen from the literature.

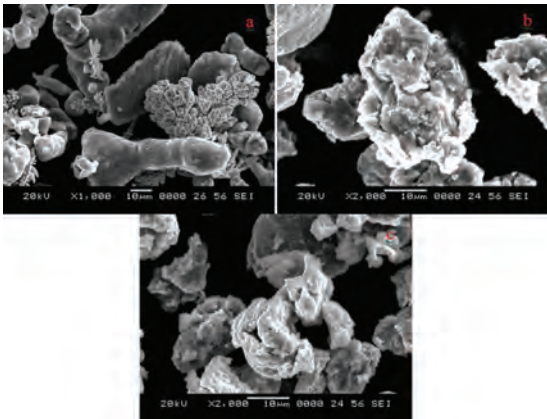


Fig.6 SEM micrographs, morphology of a) unmilled powder and b)15 hrs ball milled, c) 30 hrs ball milled

Conclusions

- 1) Elemental powders have been mechanically alloyed as a function of ball milling time, further the mechanically alloyed powder show the formation of Al (Cu Fe) ternary solid solution phase. Such a phase disappears at the end of 30 hours of ball milling time.
- 2) Compared to Cu, diffusion of Fe in Al is limited, thus elemental peaks of Al and Fe are observed even after 30 hours of ball milling time.

- 3) Each individual ball milled particle is mechanically an alloy of Al-Cu-Fe system with a composition in the vicinity of $Al_{70}Cu_{10}Fe_{20}$.
- 4) Furthermore, powder particle subjected to 30 hours of ball milling time are reduced to nano range (40 nm) and exhibit a composition of Al_4Cu_9 intermetallic phase (as proved by XRD).
- 5) The particle size in the micrographs too indicate nano scale regime.
- 6) With increase in ball milling duration, the magnetic properties of the milled powder sample decreases. The decrease is due to progressive alloying of elemental phase which reduces the direct ferromagnetic interaction between Fe-Fe atoms.
- 7) The entire ball milled powders show soft magnetic properties.
- 8) Due to ballistic diffusion as a result of SPD, solubility of Fe gets drastically reduced resulting in the Fe atom getting out of the solid solution. Thus, Fe atoms remain in the elemental form.
- 9) Powder samples mechanically alloyed for a longer ball milling duration show a transition to paramagnetic phase beyond 500 °C. Such a phase is attained mainly due to the formation of intermetallic phase from solid solution phase which existed at ambient temperature.
- 10) TEM images have indicated the formation of solid solution phase with Cu and Fe particles embedded in the Al matrix.

Acknowledgement:

We would like to thank Dr K. Narayan Prabhu H.O.D & professor, Dr Rajendra Udupa professor, Dr A. O. Surendranathan professor and Dr Udaya Bhatt associate professor in the department of metallurgical and materials engineering at NITK SURATHKAL for

providing the infrastructure to conduct various experiments. Our sincere thanks to SAIF IIT-B Mumbai and ACMS IIT Kanpur for helping us analyze various ball milled powder samples.

References

- [1] Huttunen-Saarivirta E., Microstructure, fabrication and properties of quasicrystalline Al-Cu-Fe alloys: a review, *J Alloys Compd.* 363, pp. 150-174, (2004).
- [2] Sordelet D.J., Widener S.D., Tang Y., Besser M.F., Characterization of a commercially produced Al-Cu-Fe-Cr quasicrystalline coating, *Mater. Sci. Eng A* 294-296, pp. 834-837, (2000).
- [3] Schurack F., Eckert J., Schultz L., Synthesis and mechanical properties of cast quasicrystal-reinforced Al-alloys, *Acta Mater.*, 49, pp. 1351-1361, (2001).
- [4] Tang F., Anderson I.E., Biner S.B., Microstructures and mechanical properties of pure Al matrix composites reinforced by Al-Cu-Fe alloy particles, *Mater. Sci. Eng. A* 363, pp. 20-29, (2003).
- [5] P. Barua, B.S. Murty, V. Srinivas, *Mater. Sci. Eng.* A304-306, 863 (2001).
- [6] B.S. Murty, R.V. Koteswara Rao, N.K. Mukhopadhyay, *J. Non Cryst. Solids* 334-335, 48 (2004).
- [7] V. Srinivas, P. Barua, T.B. Ghosh, B.S. Murty, *J. NonCryst. Solids* 334-335, 540 (2004).
- [8] P. Barua, B.S. Murty, B.K. Mathur, V. Srinivas, *J. Appl. Phys.* 91, 5353 (2002).
- [9] P.J. Schilling, J.-H. He, J. Cheng, E. Ma, *Appl. Phys. Lett.* 68, 767 (1996).

PHASE EVOLUTION DURING SYNTHESIS OF Ti_3SiC_2 POWDER THROUGH MECHANICAL ALLOYING

Rahul B. Mane, Y. Rajkumar and Bharat B. Panigrahi

Indian Institute of Technology, Hyderabad, Yeddumailaram, India

Abstract

The aim of the present study is to produce Ti_3SiC_2 powder with ultrafine particles at relatively lower temperatures. In this work, the mechanical alloying of reactant powders has been employed to increase the reactivity and to lower the synthesis temperature. Mechanical alloying behaviors of two different sets of reactant mixtures were studied. In the first set the elemental powders of titanium, silicon and graphite were milled, in a molar ratio of 3:1:2, and in the second set, titanium and graphite powders ball milled for different duration followed by heating to prepare titanium carbide powders. These titanium carbides were further reacted with silicon powder. Both sets of milled reactants were heated at 700°C under flowing argon. X-ray diffraction analysis of the product reveal the formation of Ti_3SiC_2 phase during heat treatment of ball milled elemental powders.

Key words: Ball milling, ultrafine powder, MAX phase.

Introduction

MAX phases are ternary carbides or nitrides having $M_{n+1}AX_n$ as a general formula, where 'M' is a early transition element from the periodic table, 'A' is group 'A' element, mostly they are IIIA and IVA group elements and 'X' is either carbon or nitrogen^[1]. MAX phases have layered hexagonal crystal structure^[1,2]. The reason for growing interest in the MAX phases lies in their unusual and unique set of properties, which makes them suitable for structural as well as functional applications^[2]. Unlike conventional ceramics; in MAX phase compounds basal dislocations are mobile at room temperature as well as at high temperatures, which provides ductility to the material^[2]. The ductility increases with increasing temperature^[3]. So far, a large number of M_2AX (211 phase) and M_3AX compounds were reported. There may be several new phases with 413 configurations such as Ti_4AlC_3 , V_4SiC_3 , and Ti_4SiN_3 etc. However, not much literature available in these compounds^[3,4].

TSC is the most widely studied compound in this group. However there were difficulties in producing single phase TSC due to the very narrow region in the Ti-Si-C ternary diagram^[5]. It was first synthesized by Jeitschko & Nowotny via chemical reaction^[6]. Later it was produced through different synthesis routes^[7, 8 and 9]. It was produced using various combinations of raw materials, like elemental powders^[7, 8], TiC+Si and TiC +SiC etc^[10]. Depending upon the starting material; different synthesis routes were used, such as direct synthesis from elemental powders and two stage synthesis processes (where presynthesized carbides were reacted with Si^[11]). To obtain the high purity TSC phase various methods were employed, such as use of excess Si, small amounts of Al and B_2O_3 powders etc. It was reported that, at 1300°C, about 83% TSC phase was obtained after addition of B_2O_3 ^[8]. It was reported that the addition of Al decreased the synthesis temperature significantly. Solid state reaction between TiC_x and Si was reported to yield TSC phase with very low amount of TiC_x

PHASE EVOLUTION DURING SYNTHESIS OF Ti_3SiC_2 POWDER THROUGH MECHANICAL ALLOYING

and intermetallic impurities^[12]. The differential scanning calorimetry (DSC) analysis of mixed TiC_x and Si powder revealed that exothermic nature of the reaction^[8]. At about 800°C reaction was started followed by a huge exothermic peak at 985°C for major phase formation^[7]. Young et al^[13] had reported the effect of varying silicon content in Ti/Si/TiC reactant mixture and concluded that the optimum silicon content should exceed the stoichiometric composition by about 10 wt%. They mentioned that excess silicon, compensated for Si loss by evaporation^[13]. On the other hand too much Si increased the undesired titanium silicides formation. Radhakrishnan et al.^[10] reported that a reaction of 3TiC/2Si powders firstly generated $TiSi_2$ intermediate phase at a temperature of 1170°C. In a second step it was converted in to TSC while SiC was also formed simultaneously. There were attempts to synthesis through self-propagating high temperature synthesis but it was yield 86-88% purity only^[8 & 9]. Some investigators^[14, 15 & 16] employed high energy mills to produce fine powders. Li et al.^[17] was reported the formation of large number of binary compounds such as TiC, Ti_5Si_3 and $TiSi_2$ phases during milling of elemental powders. Silicon content was attributed one of the deciding factor for the product purity. Ti_3SiC_2 powder with increased purity was produced by prolonged milling of elemental powders (120 hours) followed by reaction at 1100°C, however, in industrial point of view this method is not helpful^[18]. It appears that the formation of Ti_3SiC_2 phase occurs normally at very high temperature which had detrimental effect on purity. The objective of the present investigation is to study the effect of high energy ball milling on the formation of Ti_3SiC_2 phase during post milling annealing treatments.

Experimental Procedure

Titanium powder of 99.5 % purity having particle size of ~ 44 μm , the graphite powder of 99% purity having particle size of ~50 μm and silicon powder of 99.5% purity having particle size ~ 44 μm were obtained from Alfa Aesar. Syntheses of TSC were carried out through two different routes:

(a) In the first method Ti and graphite powders were mixed in a molar ratio of 3:2 and ball milled upto 20 hours at 300 rpm, [using Pulverisette P-5, Fritsch, Germany] with a tungsten carbide (WC) vial and the balls (10 and 15 mm diameter). Small amount of powders were taken for XRD study. All milled powders were compacted at very low pressure (25 MPa) and taken into alumina crucible, then thermally treated at 1100°C for a holding time of 2 hours, under high purity argon. These synthesized TiC_x powders and Si powder were mixed in the molar ratio of 3:1, and heated at 700°C, for 2 hours of holding time, under high purity argon gas. After cooling samples were pulverized and small amount of powders were taken for XRD study.

(b) In the second method: the elemental powders of titanium, graphite and silicon were taken in molar ratio of 3:2:1 and ball milled upto 30 hours. Small amount of powders were taken for XRD study at various milling intervals. Further, the milled powders were heated at 700°C for 2 hours. After cooling down to room temperature the samples were removed and ground easily into the fine size with the help of agate mortar and pestle. Characterization of all samples were carried out using X-ray diffraction (XRD-Panyaltical model: X' Pert PRO) using Cu $\lambda = 1.540560 \text{ \AA}$ and SEM (Carl-Zeiss, Model: Supra 40).

PHASE EVOLUTION DURING SYNTHESIS OF Ti_3SiC_2 POWDER THROUGH MECHANICAL ALLOYING

Result and Discussion

(a) Milling of TiC_x: XRD patterns of the titanium and graphite powders milled for 5, 10, 15 and 20 hours have been shown in Fig.1 Peaks were indexed according to JCPDS data of TiC and Titanium (No. 893828, 895009). Titanium carbide phase started forming with progression of milling. However major amounts of graphite and titanium were formed remains unreacted even after 20 hours of milling.

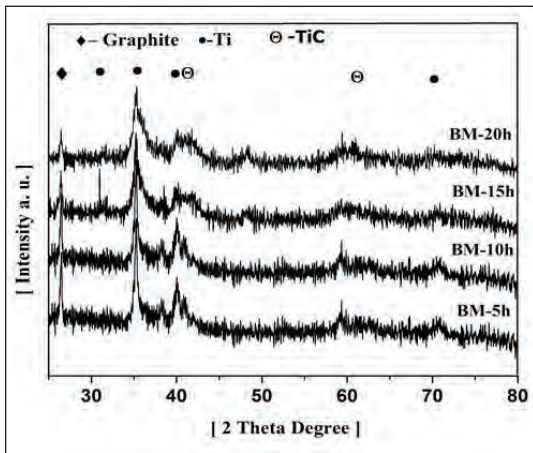


Fig. 1 XRD patterns of ball milled titanium and graphite (3:2 molar ratio) powder at 5, 10, 15 and 20 hours.

XRD pattern of thermally treated milled powders of titanium and graphite have been shown in Fig. 2; a high degree of conversion to TiC_x was observed. There is no significant change in the phase formation behavior for differently milled powders, however, variation in the XRD peak profile (i. e. relative intensities and broadening) could be clearly seen (Fig. 2). (b) Reaction of TiC_x and Si: In the next stage when these carbides were reacted with Si powders at 700°C, Ti_3SiC_2 phase could not form. The XRD patterns (Fig. 3) show the peaks corresponding to unreacted TiC_x and Si along with very small peaks of TiO_2 . This TiO_2

peaks was a result of oxygen content of Ar gas used.

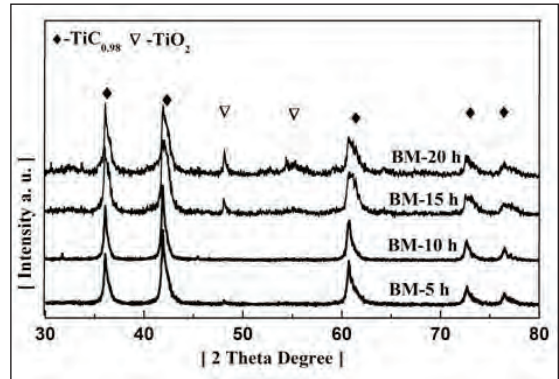


Fig. 2 XRD patterns of heat treated (1100°C) ball milled titanium and graphite (3:2 molar ratio) powder for different duration.

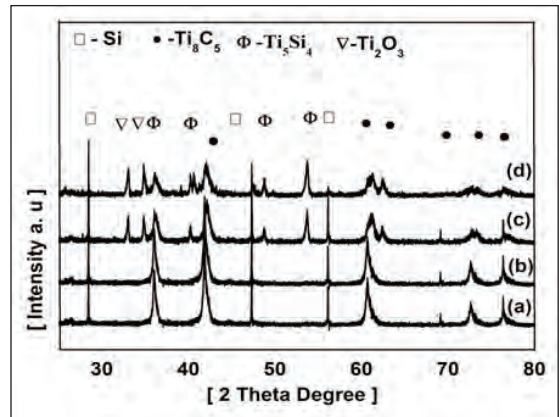


Fig. 3 XRD patterns of the reaction product of $TiC_x + Si$ At 700°C; where titanium and graphite milled for different duration followed by heating at 1100°C for 2 hours were reacted with Si powder. titanium and graphite milled for a) 5 b) 10 c) 15 d) 20 hours.

(c) Milling of elemental powders: Fig. 4 shows the XRD patterns of ball milled titanium, silicon and graphite powders for different duration. 10, 20 and 30 hours (Fig.4). TiC_x and Si peaks were observed, but no Ti_3SiC_2 formation was witnessed.

PHASE EVOLUTION DURING SYNTHESIS OF Ti_3SiC_2 POWDER THROUGH MECHANICAL ALLOYING

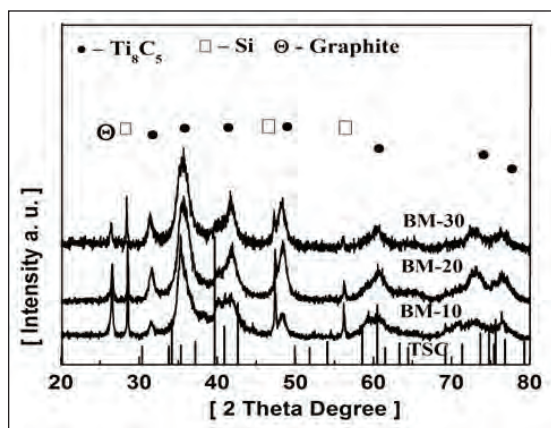


Fig. 4 XRD patterns of standard Ti_3SiC_2 and Ball milled titanium, silicon and graphite powder at 10h, 20h and 30h

When ball milled elemental powders were heat treated at $700^\circ C$, the formation of Ti_3SiC_2 phase was clearly observed (Fig. 5), while major portion of TiC_x and Si phases were remains unreacted, milling duration doesn't seems to affect much on the phase formation, however it needs further study.

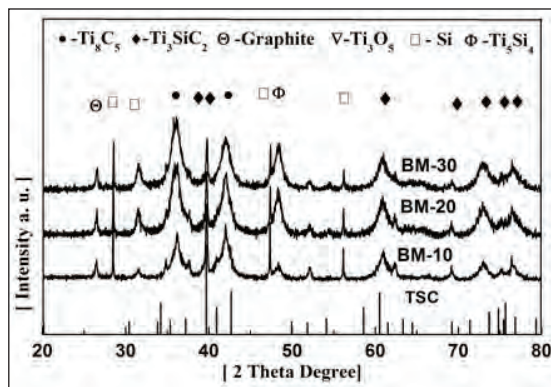


Fig. 5 XRD patterns of ball milled 3Ti-Si-2C at 10, 20 and 30 hours followed by heating at $700^\circ C$ for 2 hours.

SEM micrographs of the powder synthesized using 10 hours reactants have been shown in Fig. 6. Powders are mostly in submicron range, when powders was seen at higher

magnification, some particles with stepped surface were found; it is an indication of Ti_3SiC_2 formation. This was very encouraging observation while optimizations of many parameters are still required to achieve high purity MAX phase powders at such lower temperatures.

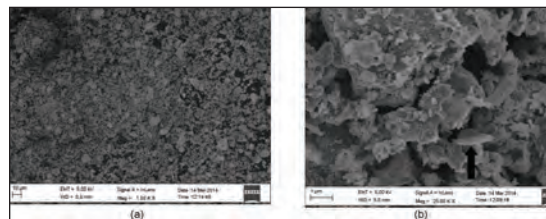


Fig. 6 Images of synthesized powder using elemental powders milled for 10h, (a) most of the particles having size below $10 \mu m$ and (b) at higher magnification some particles shows stepped surface (shown by arrow).

Conclusion

This investigation studied the effect of mechanical activation on the production of Ti_3SiC_2 MAX phase powders, and attempted to lower the reaction temperature. Ti_3SiC_2 phase formation was observed at $700^\circ C$ after the heat treatment of ball milled elemental powder mixtures of Ti, Si and graphite, although other impurity phases were also present. Further optimization of composition, milling parameters and annealing conditions are required to get high purity phase.

Acknowledgements:

The SERB-DST (Govt. of India) is gratefully acknowledged for providing the financial support.

References

- [1] Michel W. Barsoum, "The MAX Phases: A New Class of Solids Thermodynamically Stable Nanolaminates," *Porg. Solid State Chem.*, Vol.28, (2000) 201-281.

PHASE EVOLUTION DURING SYNTHESIS OF Ti_3SiC_2 POWDER THROUGH MECHANICAL ALLOYING

- [2] Michel W. Barsoum, Miladin Radovic "Elastic and Mechanical Properties of the MAX Phases," Annual rev. Material Res., Vol.41, (2011) 195-227.
- [3] Z. M. Sun, "Progress in research and development on MAX phases: a family of a layered ternary compounds," International Materials Reviews, Vol.56 (2011) 143.
- [4] Michel W Barsoum, Tamel EL-Raghy, "Synthesis and characterization of a remarkable Ceramic Ti_3SiC_2 ," J. Amr. Ceram. Soc. Vol.79 (1996) 1953-1956.
- [5] Ke Tang, Chang-an Wang, Young Huang and Jinxia Xia, " An X-ray diffraction study of the texture of Ti_3SiC_2 fabricated by hot pressing," journal of the European ceramic Society Vol. 21 (2001) 617-620.
- [6] Jeitschko, W., H. Nowotny. "Die Kristallstruktur von Ti_3SiC_2 ein neuer Komplexcarbidge-Typ," Monatshefte für Chemie und verwandte Teile anderer Wissenschaften 98.2 (1967) 329-337.
- [7] B. B. Panigrahi, M. C. Chu, A. Balakrishnan, S. J. Cho, "Synthesis, pressureless densification and sintering kinetics of Ti_3SiC_2 powder," J. Mater. Research, Vol.24 (2009) 487-492.
- [8] B. B. Panigrahi, N. S. Reddy, A. Balakrishnan, M-C Chu, S-J Cho, J. J. Gracio, "Nickel assisted sintering of Ti_3SiC_2 powder under pressureless conditions" J. Alloys and Compounds, 505 (2010) 337-342.
- [9] Li SB, Xie JX, Zhang LT, Cheng LF. "Synthesis and some properties of Ti_3SiC_2 by hot pressing of titanium, silicon and carbon powders part 1-effect of starting composition on formation of Ti_3SiC_2 and observation of Ti_3SiC_2 crystal morphology" Mater Sci Technology, Vol.19 (2003) 1442-1446.
- [10] Radhakrishnan R, Bhaduri SB, Henager Jr CH, "Analysis on the sequence of formation of Ti_3SiC_2 and Ti_3SiC_2/SiC composites," Adv Powder Metall Part Mater Vol.13 (1995) 129-137.
- [11] M. A. El Saeed, F. A. Deorsola and R. M. Rashad "Optimization of the Ti_3SiC_2 MAX phase synthesis," international journal for refractory metals and hard materials, Vol.35 (2012) 127-131.
- [12] Mohamad Johari Abu, Julie Juliewatty Mohamed, Zainal Arifin Ahmad, "Effect of Excess Silicon on the Formation of Ti_3SiC_2 Using Free Ti/Si/C Powders Synthesized via Arc Melting," ISRN Ceramics, Vol.10 (2012) 5402.
- [13] Debashis Bandyopadhyay, "The Ti-Si-C System" JPEDAV 25 (2004) 415-420
- [14] SB Li, HX Zhai, Y Zhou, ZL Zhang, "Synthesis of Ti_3SiC_2 powders by mechanically activated sintering of elemental powders of Ti, Si and C", Materials Science and Engineering: A (2005) 315-321.
- [15] Michel W. Barsoum, Miladin Radovic "Elastic and Mechanical Properties of the MAX Phases" Annual rev. Material Res., 41 (2011) 195-227.
- [16] Z. M. Sun, "Progress in research and development on MAX phases: a family of a layered ternary compounds" International Materials Reviews, 56 (2011) 143.
- [17] Z. M. Sun, "Progress in research and development on MAX phases: a family of a layered ternary compounds" International Materials Reviews, 56 (2011) 143.
- [18] Fanling Meng, Laurent Chaffron, Yanchun Zhou "Synthesis of Ti_3SiC_2 by high energy ball milling and reactive sintering from Ti, Si, and C elements" Journal of Nuclear Materials 386-388 (2009) 647-649.

PROCESSING AND EVALUATION OF ALUMINIUM Mn – Cu ALLOY THROUGH POWDER METALLURGY

Arunkumar S, Sathish kumar M, Chandan Byral R, Prof. S. Kartikeyan

VIT University, Vellore, Tamil Nadu.

Abstract

This investigation is carried out to improve the mechanical properties of Al-Mn-Cu alloy through powder metallurgy technique. The samples are prepared with varying weight percentage of copper (0.12%, 0.25%, 0.50%, 1%) present in the alloy and the densification parameter hardness (Rockwell Hardness Tester) value were calculated. The powders were in a traditional way by using mortar for more than 40 minutes for each sample. The powders were then compacted (360 MPa) under UTM (TUE-CN-1000) by using Titanium Carbide die for making the sample size of 25mm diameter and 15mm height. The compacted green samples were sintered in a horizontal box sintering furnace (DST.SERB) and in microwave sintering furnace to compare the conventional & Microwave sintering effects on the alloy in hand. And the densification parameter, hardness (Rockwell hardness tester) value were calculated. The microstructural characteristics were investigated using optical microscope (OP). The results shows that, as the percentage of copper present in the Al-Mn-Cu alloy increases the hardness value. The microstructure of the conventional sintered samples revealed that the primary phase of Al_6Mn was present in the grain boundaries. From the result, it is clear that the maximum hardness value (39.5 HRB) was obtained for the sample of mixture Al-1.2Mn-1Cu. And also it was having maximum densification parameter value of 0.46. The microwave sintered compacts showed absence of intermetallics phase (Al_6Mn) due to lesser time available for the precipitation of intermetallic phases. Porosity distribution is uniform in microwave sintered samples whereas porosities are concentrated more at the core in conventional sintered samples. The microstructure of microwave sintered samples are hardly altered by the microwave sintering process. For the microwave sintering maximum hardness value (43 HRB) was obtained for the sample of mixture Al-1.2Mn-1Cu with the densification parameter of 0.39.

Keywords: Al-Mn-Cu alloy, densification parameter, Dilatometric analysis, OM, microwave sintering.

Introduction

The component which is produced from powder metallurgical (PM) techniques are being utilised in the automotive and structural applications [1], where low cost and light weight materials are the essential design criteria. The P/M aluminum alloys are replacing small Al die casting which requires precision net shaping and better material utilization [1]. Sintering of aluminum alloys were considered to be very difficult due to the presence of the thermodynamically stable oxide layer on

powder particle surface, which limits their use to niche applications in the aerospace industry. Conventional press-and-sinter P/M is an exemplary net shape process and therefore offers inexpensive manufacturing. In recent years, increasing interest in high precision and cost effective processing of lightweight materials has created an opportunity for powder metallurgical (P M) processing of aluminum alloys. Due to their lightweight, high compressibility, exceptional specific strength and economical processing, P M

PROCESSING AND EVALUATION OF ALUMINIUM Mn - Cu ALLOY THROUGH POWDER METALLURGY

aluminium alloys have potential to replace components fabricated by cast and wrought route in automotive industry [2-4].

Researchers have established that metal powder can be efficiently heated by microwave energy. Where in the dielectric loss and eddy current loss have important roles.

Now a day's most of the aluminium alloys produced through powder metallurgy and the aluminium 3000 series alloy having advantages over the other material due to their light weight, thermal conductivity and anticorrosion properties. The Al-Cu based alloys are mostly used in recent years.

Many of Al-Cu alloy consists up to 0.8% Mn and inclusion of very small (up to 0.2%) amount of transition elements like Zr, V, Ti, etc. The TM particle produced during homogenization process having larger grain size because of high temperature (530^oc) of this process [3]. Further the increase of the mechanical properties of the alloy was improved addition of transition element like Mn [4]. Then the rapid solidification technique was successfully applied to improve the mechanical properties of aluminium alloy which containing higher amount of Mn [5].

The aim of present study is to understand the effect varying percentage of copper which is present the Al-Mn-Cu alloy by determining the densification parameter, investigating microstructure characteristic and calculating mechanical properties. And also comparing the conventionally sintered & microwave sintered densities and hardness values for the same samples.

Table 1: Chemical composition of Al 3003 alloy:

| Sample | %Cu | %Mn | %Al |
|--------|------|-----|-------|
| 1 | 0.12 | 1.2 | 98.6 |
| 2 | 0.25 | 1.2 | 98.55 |
| 3 | 0.5 | 1.2 | 98.3 |
| 4 | 1 | 1.2 | 97.8 |

Experimental Procedure

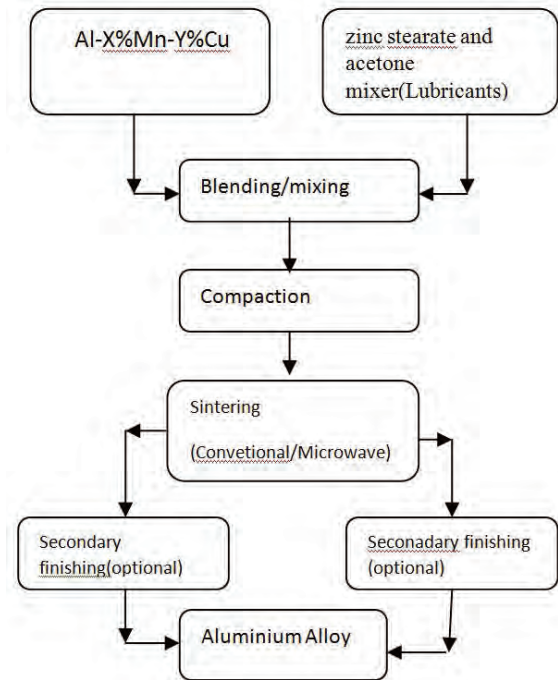


Fig. 1. Flow chart represents process flow for the Al alloy produced.

Conventional Sintering:

In the present study Al-Mn-Cu alloy was prepared by using aluminium (99.97% of pure), manganese (99.9% of pure), and copper (99.9% of pure). The different composition samples were prepared by the varying the percentage amount of copper present. Totally four compositions were taken and that is tabulated in Table 1. The mass of each samples were calculated theoretically and that was around 20 grams. Then the weighing of powders were completed using weighing machine which having accuracy in milligrams. For getting homogenous mixing, the prepared powders were mixed in a traditional way of using mortar for more than 40min of each. The powders were compacted in UTM machine (TUE-CN-1000, Fine Spray

PROCESSING AND EVALUATION OF ALUMINIUM Mn - Cu ALLOY THROUGH POWDER METALLURGY

Associates and Engineers, Miraj) by using titanium carbide die for making pallet size of 25mm diameter and 15mm height. Samples were pressed uniaxially with the pressure of 360 Mpa that means around 18 tons. To performing lubrication effect zinc stearate and acetone mixer was applied to inner side of die and upper portion of punch. Then the green densities of compacted pallets were found by measuring mass, diameter and length. Flow chart of the process is shown in Fig. 1.

To study the density behaviour, the micro structural and mechanical properties, the compacted green samples were sintered in a horizontal Box sintering furnace (DST. SERB, INDFRR SUPERHEAT FURNACES). The compacts were heated at a rate of 5°C per min up to 500°C. Then to ensure the uniform temperature distribution the samples were maintained at 500°C for 1hr. The mass, diameter and height of samples were measured to getting sintered density.

The sintering density was expressed in grams per cubic centimetre and this was normalised with respect to the theoretical density based on the weight fraction (w) of the respective component. The theoretical density for a given composition p_{th} was calculated using inverse rule of mixture and is expressed as

$$\frac{1}{\rho T} = \sum_{i=1}^N \frac{w_i}{\rho_i}$$

The sinterability of the samples were calculated through a densification parameter which is expressed as

$$\text{Densification parameter} = \frac{\text{sintering desity} - \text{green density}}{\text{theoretical desity} - \text{green density}}$$

The hardness values of samples were measured using Rockwell hardness tester (NRS, TMC Associates, Fine Engineering industry, Miraj) at 100kg load. B scale was used to calculating hardness value of aluminium alloy samples.

Totally eight reading were noted down and average value of reading was taken. Then sintered sample was polished using emery paper of different size (220, 400, 600, 800, 1000) for 30mins each. The polished samples were etched with 92 ml of Distilled water, 6 ml of Nitric acid, 2 ml of Hydrofluoric acid, to examine clear microstructures. The optical microscope was used to determine the microstructure of the sintered sample.

In conventional sintering thermal gradients, which are produced because of conductive and radioactive heat transfer can be minimized to a greater extent. By eliminating temperature gradient it is possible to reduce internal stresses, which further initiates the cracking of parts during sintering. It also creates a more uniform microstructure, which may lead to improved mechanical properties and reliability.

Pressure and density distributions after compaction:

As a result of compaction, the density of the part, called the green density is much greater than the starting material density, but is not uniform in the green. The density and therefore mechanical properties vary across the part volume and depend on pressure in compaction as shown in Fig. 2.

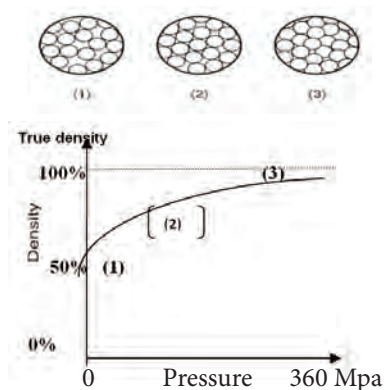


Fig.2 Pressure and density distributions after compaction

Microwave sintering:

The basic idea of using microwave energy for the heat treatment of materials is well known: deposit the energy directly within the product and possibly create a uniform temperature distribution. A remarkable energy and time saving can be obtained and the resulting products present often enhanced mechanical properties with respect to conventional treated ones (Anklekar et al., 2001; Gerdes and Willert-Porada, 1994; Gupta and Wong, 2006), because the heating is more uniform and volumetric. On the other hand, treatment repeatability often represents a limit in microwave assisted processing, due to the numerous and interacting factors that can alter the electromagnetic field distribution near the samples, and therefore the way they will be heated.

All the four samples listed in table 1. were sintered in a microwave furnace (multimode cavity) at 2.45GHz (Cober Electronics, MS6K) using suscept or materials as auxiliary heating elements. An input power of 1.8kW was used in the sintering processes. The final densities of the compacts were measured by the Archimedes method. The microstructures of the microwave-sintered samples were observed. The density and densification parameters are calculated as same that of the conventional sintering.

Another possible reason for the samples' densification behaviour could be the stage of sintering of the bodies. The Strongest influence of the microwave effect (Janney et al., 1992; Wang et al., 2006) occurred in the intermediate stages of sintering, with the effect decreasing as the densification increased. An incident wave on a conductive metallic material is mainly reflected, and the rest cannot pass through the superficial layer of the metal itself. The penetration depth of the microwaves at a given frequency " f " depends

on the electrical and magnetic properties of the material and it is a very important parameter, because it constitutes an upper limit to the thickness of the material which can be heated directly by microwaves. The skin depth " d " (m) is defined as the depth into the conductor from the surface at which the current density is $1/e$ of its value at the surface (Meredith, 1998), given by:

$$d = \sqrt{\frac{1}{\pi f \sigma \mu_0}}$$

Microwave energy has been in use for variety of applications for over 50 years. These applications include communication, food processing, wood drying, rubber vulcanization, medical therapy, polymers, etc. Use of microwave technology in material science and processing is not rather new. The areas where it has been applied includes: process control, drying of ceramic sanitary wares, calcination, and decomposition of gaseous species by microwave plasma, powder synthesis, and sintering.

Result and discussion

The higher sintered density was observed for microwave nitrogen sintered samples and thereafter a decreasing trend, whereas conventional samples resulted in better densification at higher temperatures. At lower sintering temperature, Al-Cu alloys experiences either swelling or shrinkage behavior. The higher sintering temperature results in initial swelling; followed by shrinkage such that alloy attains the solid-liquid state region. It can be seen that microwave sintered samples in N₂ decrease in density after 590°C, due to the faster heating rate during microwave heating, Cu, have less time to diffuse into Al lattice and therefore the spreading reduces causing to slow down the homogenization process. Hence it can be

PROCESSING AND EVALUATION OF ALUMINIUM Mn - Cu ALLOY THROUGH POWDER METALLURGY

hypothesized that microwave sintering in N₂ at 590°C has attained an alloy homogenization, and contained sufficient volume fraction of permanent liquid. The electrical conductivity depends on the surface micro structural characteristics. Higher sintering temperature (630°C) resulted in higher sintered density that implies less porosity and better electrical conductivity. Results are shown in Table 2.

Table 2. Shows the comparison of Conventional Sintering Vs Microwave sintering Properties

| Sample | Conventional sintering | | | Microwave sintering | | |
|--------|-------------------------|---------|----------|-------------------------|---------|----------|
| | Densification Parameter | Density | Hardness | Densification Parameter | Density | Hardness |
| 1 | 0.192 | 96.9 | 33.1875 | 0.181 | 98.2 | 35.12 |
| 2 | 0.141 | 87.15 | 36 | 0.123 | 92.5 | 38.2 |
| 3 | 0.47 | 96.2 | 39 | 0.38 | 106.6 | 40.35 |
| 4 | 0.46 | 97.08 | 39.5 | 0.44 | 108.15 | 42.8 |

Densification parameter:

The effect of varying percentage of copper present in the alloy and the sintered density are shown in the Fig 3. It is clear that sintered density of the compacted samples get increases as the percentage of copper increases.

The effect of different percentage of copper and densification parameter values is given in the Fig 4. It was noted that densification parameter value for Al-1.2Mn-1Cu was much higher than the remaining. The presence of copper in the aluminium alloy improves the diffusion rate. So that densification parameter value also increases.

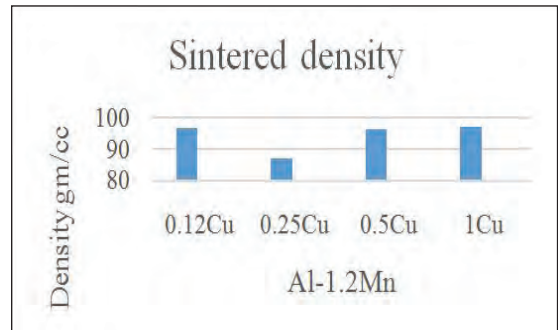


Fig. 3: Effect of varying percentage of copper in the mixture and the sintered density

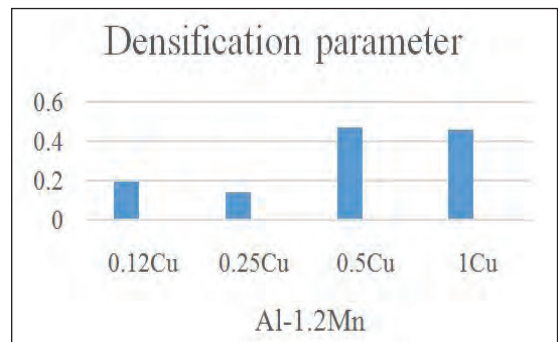


Fig. 4: Effect of different percentages of copper and densification parameter

Sintered density and densification parameter for the Microwave sintering is shown in Fig.5 & Fig.6.

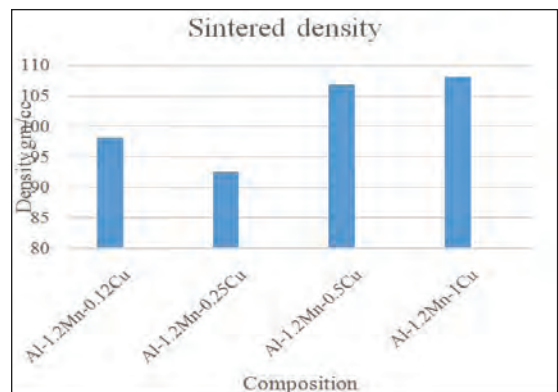


Fig. 5: Effect of varying percentage of copper in the mixture and the sintered density

PROCESSING AND EVALUATION OF ALUMINIUM Mn - Cu ALLOY THROUGH POWDER METALLURGY

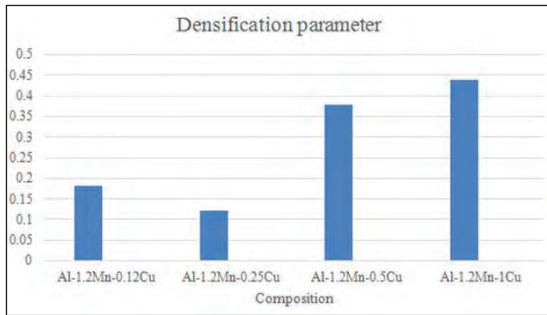


Fig. 6: Effect of different percentages of copper and densification parameter

Sintered density is the major factor influencing the mechanical properties of the material processed through powder metallurgy. Sinter densities of the compacts were determined by the rule of mixture. Powder metallurgy products are prone to porosity. Since, the alloy developed in this work is focused for structural applications, the porosity estimation as well as reduction of porosity is essential. Technically, porosity is inversely proportional to density, i.e. higher porosity and lower density leads to poor mechanical and chemical property. Therefore, it is necessary to obtain good density P/M components by adopting newer consolidation technique like hot compaction and microwave sintering. Fig.3 shows the density values of sintered materials at different composition. In fact, density of the conventional P/M alloy is dependent on many variables such as powder morphology, particle distribution, compaction parameters, sintering parameters, etc. The density obtained in this work is around 97% of the theoretical density of alloy/composites with the remaining 3% porosity density increasing due to hot compaction and microwave effect. Hot compaction gives better densification. Volumetric and rapid heating of material through microwave results in high shrinkage and less porosity.

Hardness study:

For the prepared mixture of alloy, the hardness evaluation test was carried out through the Rockwell Hardness tester with loading condition at 100 kg. The results of which shows that Al-1.2Mn-1Cu alloy shows the maximum hardness (39.5 HRB) when compared to other three samples as described in Fig. 7 & 8.

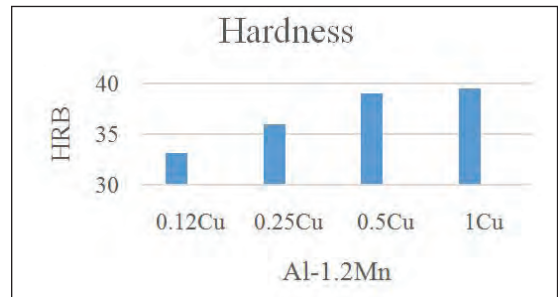


Fig. 7: Effect of different percentages of copper on Hardness in Conventional sintering.

Microstructure study:

Microstructure with well defined grains and small amount of porosity mostly at inter particulate regions can be seen in pure Al compacts. Porosity distribution is uniform in microwave sintered samples whereas porosities are concentrated more at the core in conventional sintered samples (indicating reduced the heat flux in the core).

In conventional sintering the grains of Al are coarser indicating re-crystallization and grain growth. While in microwave sintering the contact points are welded without much heating of grains and hence the strength properties of microwave composites are much better.

PROCESSING AND EVALUATION OF ALUMINIUM Mn - Cu ALLOY THROUGH POWDER METALLURGY

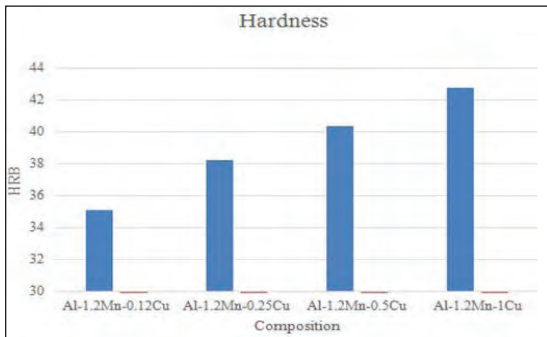


Fig. 8: Effect of different percentages of copper on Hardness in Microwave sintering.

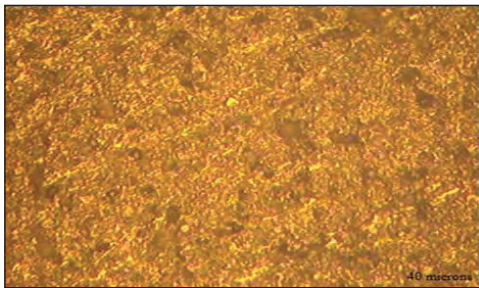


Fig 9: Al-1.2Mn-0.12Cu

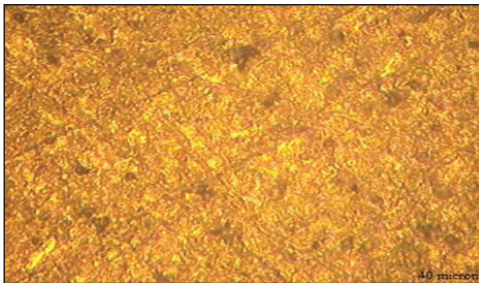


Fig 10: Al-1.2Mn-0.25Cu

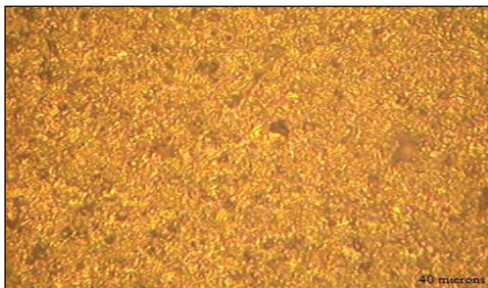


Fig 11: Al-1.2Mn-0.5Cu

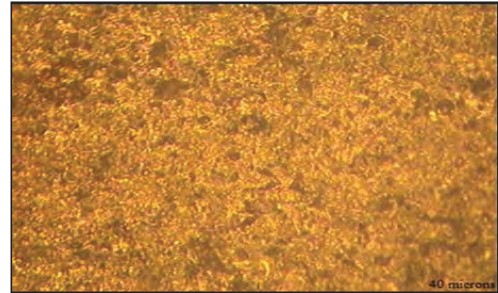


Fig 12: Al-1.2Mn-1Cu

The microstructure images of all the four samples are shown in the above four figures (Fig 9, Fig 10, Fig 11 and Fig 12). Out of four structures, the Al-1.2Mn-1Cu alloy sample has more particle distribution and shows a good uniform mixture of Cu and presence of Al_6Mn at the grain boundaries. Based on this we can conclude that, the Al-1.2Mn-1Cu shows good hardness value and better density which was proved in the previous chapter.

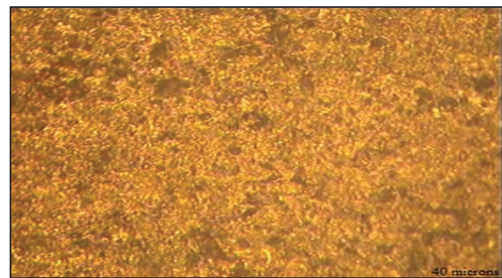


Fig 13: Al-1.2Mn-0.12Cu (Conventional sintering)



Fig 14: Al-1.2Mn-0.12Cu (Microwave Sintered)

PROCESSING AND EVALUATION OF ALUMINIUM Mn - Cu ALLOY THROUGH POWDER METALLURGY

Microwave sintered compacts showed absence of intermetallics phase (Al_6Mn) due to lesser time available for the precipitation of intermetallic phases. Conventionally sintered compacts at $630^{\circ}C$ resulted in higher density and improved mechanical properties which can be attributed to grain refinement in sintering microstructure and Al_6Mn precipitates as shown in Fig. 13&14.

The size and distribution for intermetallic particles contribute to the sequence of events leading to fracture. As an example, coarse Mn-containing dispersoids played an important role in controlling fracture resistance, since the voids formed at the larger constituent particles were linked through the secondary void formation at dispersoids. Alternatively, very fine Mn-dispersoids act as barriers to the dislocation motion promoting cross-slip, which leads to a uniform homogeneous deformation. Consequently, crack initiation is delayed and the fatigue life is extended compared to an Al-alloy without the Mn dispersoids. The average grain size for the composites/alloys can be calculated by the following formula:

$$\text{Grain Size} = Pz [(1-V_f)/V_f]^{1/3}$$

Wear Behaviour

It shows that the composite wear loss strongly depends on reinforcement loading in the alloy. As the alloying phase content increases from 5 to 15 wt%, the wear loss decreases. The Al3003 alloy is tested reinforced with 0.12, 0.25, 0.5 and 1 wt% copper under an applied load of 10 N - 20 N at 500 r.p.m. it can be shown that increase in the applied load from 10 N to 20 N sharply increases the wear rate and with the increase in the reinforcement the wear rate is decreased. The alloys with high hardness abraded at lower rates. The Al_6Mn reinforcement phases impeded the indentation and removal by scratching of material from the surface by the abrasive particles; this resulted

in the lower wear rates. It is apparent that with the increase in the reinforcement, the wear rate decreases. Moreover; the wear loss of the composites/alloy increases rapidly with increasing sliding distance indicating that the counter body can deform and remove the material from alloys progressively. However, a much slower increase in wear loss is observed at lower load (10 N) whereas, the wear loss varies almost linear with the sliding distance under specific loading conditions. The wear loss increases with the sliding distance and applied load. At higher load (20 N) the wear loss of the composite is high. The hardness of the counter body is 39.5 HRB, which is higher than the hardness of the microwave sintered Al3003 composites. The Al3003 alloy and composites are removed by the hard counter body and this removal is faster at 20 N load. Since, at lower load the wear loss is very small, the mechanism operative at 10 N is the polishing wear. As the load is increased to 20 N the wear loss increases due to the plastic ploughing and grooving of alloy and alloys with the higher sliding distances. At higher load and longer sliding distances the polishing wear mechanism is accompanied by the plastic ploughing and grooving wear mechanisms and cause more wear loss from the composite surface. At higher loads and less reinforcement loading (0.5% Cu) the matrix deformation and removal is inevitable.

Dilatometric analysis:

Dilatometric evaluation of Al-Mn-Cu alloy carried out for better understanding the phenomenology of the densification of the Al-Cu compacts the dimensional changes were measured in situ during sintering using dilatometry. However, owing to the instrument's limitations, dilatometric evaluation could be performed through conventional heating mode only. The dilatometric data of shrinkage and shrinkage

PROCESSING AND EVALUATION OF ALUMINIUM Mn - Cu ALLOY THROUGH POWDER METALLURGY

rate vs. temperature for the as-pressed Al-1.2Mn-1Cu compacts prepared using premixed and prealloyed binder. It is evident that both compacts undergo gradual densification during heating till 360°C. Subsequent heating beyond 840°C results in sudden increase in the axial shrinkage and shrinkage rate.

From the dilatometric results it can be discerned that the Al-1.2Mn-1Cu alloy exhibits slightly higher densification particularly at lower temperatures. For compacts heated or sintered at higher temperatures, the densification in both the compacts is not too different and is attributed to homogenization of the premixed matrix through interdiffusion. It is well known that Cu and Mn have mutual intersolubility. Hence, it is quite reasonable to assume that the premixed Mn-Cu powders will get completely homogenized during conventional sintering.

Conclusion

The microwave sintering of aluminum alloys resulted in saving of sintering time upto 50% as compared with conventional sintering. The absence of swelling in microwave vacuum sintered samples combined with higher sintering temperature showed the further chance of extending their use in industrial applications. Based on the experiments carried out the following are the results that are found out:

- 1) Sintered density of Al-1.2Mn-1Cu samples of Aluminium alloy for conventional sintering is 2.6505 gm/cc. For the Same alloy composition with microwave sintering exhibits 3.9296 gm/cc
- 2) Densification parameter of Al-1.2Mn-1Cu samples of Aluminium composites was 0.46 and for microwave sintering was 0.39.
- 3) Hardness of Al-1.2Mn-1Cu conventionally sintered samples of Aluminium alloy was 39.5 HRB & that of the Microwave Sintered one is 42.5.
- 4) Microwave sintering of mechanically alloyed Al3003 alloy and composites resulted in good density, i.e. 94% of theoretical density.
- 5) The effect of copper in 3003 alloy was studied with respect to hardness value. There was a trend that hardness value increased with increase copper content.
- 6) The wear rate was low with increasing Cu content.
- 7) Diffusion process intensifies by using microwave due to its enhanced mechanism.
- 8) The effect of oxidation on sintering of metal powder by microwave is less effective phenomenon in comparison to conventional sintering.
- 9) For a given heat treatment with an increase in V_f and P_z , an increase in hardness values in the alloy will result.
- 10) During microwave sintering, at lower temperatures surface diffusion and at higher temperatures volume diffusion are dominant diffusion mechanisms as in the case of pure copper powder.

Other conclusions of the investigation include the following description.

Porosity distribution is uniform in microwave sintered samples whereas porosities are concentrated more at the core in conventional sintered samples. The microstructures of microwave sintered samples are hardly altered by the microwave sintering process. In conventional sintering process the grain is recrystallized and becomes soft. It is therefore apparent that in contradiction to the standard paradigm, the properties of pressed-and-sintered aluminium alloys are not limited by the "oxide problem". Aluminium P/M alloys can be improved without recourse to hot working or master alloy powders if their design is based on an understanding of the underlying

PROCESSING AND EVALUATION OF ALUMINIUM Mn - Cu ALLOY THROUGH POWDER METALLURGY

sintering processes and the characteristics of an ideal liquid phase sintering system. Once an alloy has been optimised for sintering, a variety of new options can be realised. Free formed, functionally graded, aluminium matrix composites and high strength materials are two such examples.

In all the tests carried out, the Al-1.2Mn-1Cu alloy shows better results when compared to other compositions. Hence this percentage mixture (1% of Cu) of composites can be used for the applications like automobile, structural, etc. Thus, to realize its maximum potential, the P/M industry will inevitably need to take advantage of this key technique.

Acknowledgement

We sincerely thank for the people in the labs, Strength of Material lab, Materials Engineering and technology lab and metal matrix composites lab for their kind help and also I would like to thank CMTI staff for their kind concern in providing testing facilities.

References

- [1] R. M. German: 'Powder metallurgy science', 2nd edn; 1994, Princeton, NJ, Metal Powder Industries Federation.
- [2] B.A. Chen, L. Pan, R.H. Wang, G. Liu, P.M. Cheng, L. Xiao, J. Sun, Effect of solution treatment on precipitation behaviors and age hardening response of Al-Cu alloys with Sc addition, *Mat. Sci. Eng. A* 530 (2011) 607-617.
- [3] CAI Yuan-hua, CUI Hua, ZHANG Ji-shan. Microstructures and precipitation behaviour of cryomilled Al-Zn-Mg-Cu-Mn powders [J]. *Materials Science and Technology*, 2010, 26(3): 352 - 355.
- [4] SHARMA M M, AMATEAU M F, EDEN T J. Mesoscopic structure control of spray formed high strength Al-Zn-Mg-Cu alloys [J]. *Acta Materialia*, 2005, 53(10): 2919 - 2924.
- [5] SHIMIZU H, OSAMURA K, ADACHI H, KUSUI J, KIKUCHI K. Influence of additional Mn and Cu contents on mechanical properties of Al-Zn-Mg ternary based alloys [J]. *Journal of Japan Institute of Light Metals*, 2004, 54(1): 2 - 8.
- [6] C. Padmavathi, S.S. Panda, D. Agarwal, A. Upadhyaya, *Innovative Processing and Synthesis of Ceramics, Glasses and Composites: Processing*, Proceeding of MS&T 2006, Cincinnati, OH. pp517-528.
- [7] C. Padmavathi, A. Upadhyaya and D. Agrawal, *Scrip. Mater.* V.57, 2007, pp.651-654.
- [8] W. H. Hunt, Jr: *Int. J. Powder Metall.*, 2000, 36, (6), 51-60.
- [9] Dieter, G. E. (1988). *Mechanical metallurgy*. McGraw-Hill Book Comp. Ltd. U.K.
- [10] H. Jones, in: H.M. Flower (Ed.), *High Performance Materials in Aerospace*, Chapman & Hall, London, 1995, pp. 340-356.
- [11] P.E. Matthews, *Int. J. Powder Metall.* 4 (1968) 39.
- [12] W. Kehl, H.F. Fischmeister, *Powder Metall.* 23 (1980) 113.
- [13] W. Kehl, H.F. Fischmeister, Observations on dimensional changes during sintering of Al-Cu compacts, in: D. Kolar, S. Pejovnik, M.M. Ristic (Eds.), *Sintering – Theory and Practice*, Proceedings of the Fifth International Round Table Conference on Sintering, Yugoslavia, Elsevier, Amsterdam, 1981.
- [14] I.E. Anderson, J.C. Foley, J.F. Flumerfelt, Simplified aluminum powder metallurgy processing routes for automotive applications, in: W.F. Jandeska, R.A. Chernenkoff (Eds.), *Powder Metallurgy Aluminum and Light Alloys for Automotive Applications*, MPIF, Dearbon, MI, 1998.
- [15] T. Watanabe, K. Yamada, Effects of Copper Adding Methods on the Strength of Sintered Aluminium-Copper Alloys, Vol. 19, *Castings Research Laboratory*, Waseda University, 1968.

INFLUENCE OF PROCESS CONDITION ON SINTERABILITY OF A PREMIX Al-Si ALLOY

A. A. Methe, N. B. Dhokey

College of Engineering, Pune, India.

Abstract

Aluminium-Silicon premix alloy has been of particular interest as this alloy offers the advantage of high strength and good temperature resistance. In the proposed research, the standardization of sintering parameters viz. mixing period, sintering time and compaction pressure were carried out on the (Al -7.5Si-2.5Cu-0.8Mg-1.63Zn-1Fe) premix alloy. The effects of alloy additions (i.e. Si, Cu and/or Mg) on sintering and heat treatment response were also investigated in this study. The mixing period was varied between 4 h to 8 h with a time interval of 2 h. The Compaction pressure was varied between 250 to 400 MPa with an interval of 50 MPa. The blended powder was compacted and sintered in ultra-high purity nitrogen atmosphere in tubular sintering furnace at 560°C. The mixing time of 6 h gave 92% theoretical sintered density and hardness of 71 HRH with a uniform distribution of alloying elements at compaction pressure of 250 MPa and 30 min sintering time. On further increasing the compaction pressure to 400 MPa gave 94% theoretical sintered density and hardness of 94 HRH. The maximum transverse rupture strength of 154MPa was obtained. By varying compacting pressure, the sintered alloy demonstrates evolution of distinct phases leading to liquid phase sintering.

Keywords: Compaction Pressure, Milling Period, Sintering time

Introduction

Aluminium-Silicon P/M alloys have attracted attention for automotive and aerospace applications because of their good mechanical properties with high thermal properties. The fabrication of Al-Si binary alloy by compaction and sintering was found to be unfeasible in term of obtaining high density. The main drawback in P/M components is porosity. Sintered materials are typically characterized by residual porosity after sintering, which is quite detrimental to the mechanical properties of these materials. The nature of porosity can be controlled by several processing variables such as compaction pressure, sintering temperature and time, alloying additions and particle size of initial powders [12]. Utilization of deoxidization mechanism of magnesium (Mg) is an effective method to remove the oxide films at aluminum (Al) alloy powder surface. The continuous

amorphous oxide film at Al alloy surface are broken and removed by deoxidization of Mg. Crystalline particles of $MgAl_2O_4$ or MgO, or both of them, are formed, which depend on Mg content in Al alloy powder and sintering temperature. After that the metal/metal contact is caused, and solid state sintering of Al alloy powder is facilitated. The electrical resistivity and tensile properties of powder compacts are improved by Mg addition [3]. Mechanical properties of aluminium alloys can be improved either on a micro (≤ 0.5 wt. %) or macro (1–20 wt. %) scale with small additions of some alloying elements such as Cu, Mg, Zn, Si and specifically trace additions of Sn along with high sintering temperatures and modified heat treatments. Addition of tin and magnesium facilitates liquid phase sintering where magnesium addition is necessary for reduction of oxide layer on

INFLUENCE OF PROCESS CONDITION ON SINTERABILITY OF A PREMIX Al-Si ALLOY

aluminium powder particle The sintering response of Al-Sn system (0.4 to 0.8% Sn by wt) and Al-Mg system (0.5 to 2% Mg by wt) has indicated the impact of mixing techniques on sintered properties of these binary premix alloy systems [16]. During densification of the phases, the grain size enlargement takes place which results in higher density values. Pores are mainly formed at the aluminium particle boundaries and at boundaries of various undissolved phases formed by the alloying elements and these phases formed precipitates during solution heat treatment due to which grain size enlargement and pore size reduction takes place [9].

In this research work the effects of alloy additions (i.e. Si, Cu and/or Mg) on sintering and heat treatment response is investigated in this study. By varying compacting pressure, the sintered alloy demonstrates evolution of distinct microstructural features leading to liquid phase sintering.

Experimental Procedure and Methods

Selection of powders

The principal matrix powder was elemental Aluminium (Al) and other elemental powders of Copper (Cu), Silicon (Si) and Magnesium (Mg) were used as an alloying element.. Their corresponding physical and chemical properties are listed in Table 1.

Table 1: Powder properties

| Sr. No | Type of powders | Apparent density, g/cc | ASTM Particle size (μm)/Mesh |
|--------|----------------------------|------------------------|---|
| 1 | Aluminium Powder | 1.23 | 170 (90 μm) |
| 2 | Electrolytic Copper Powder | 1.62 | 325 (45 μm) |
| 3 | Silicon Powder | 0.96 | 170 (90 μm) |
| 4 | Magnesium Powder | 0.72 | 270 (52 μm) |
| 5 | Iron Powder | 2.638 | 45 μm |

Blending and fabrication of sintered compacts

The powder was mixed in a stainless steel ball mill by keeping ball to powder ratio of 10:1 by weight. Mixing techniques were carried out by varying the mixing time while keeping the

speed constant as 60 rpm. The powder was milled for varying period from 4 to 8 h at time interval of 2 hour and compacted to desired size of diameter 16mm and 5 mm height in a Hydraulic compaction machine of 50 tonne for varied compacting pressures ranging from 250 to 400 MPa.

Sintering

The compacted samples were sintered in an atmosphere controlled tubular sintering furnace temperature. Samples were sintered at 560 °C and soaked for different periods 30, 45, 60 minutes and then water quenched. Green compacts were sintered in a gasified liquid nitrogen atmosphere with a flow rate of 3 litres per min.

Characterization

The green and sintered density was measured using Archimedes's principle and compared with the theoretical density calculated by using Rule of Mixture (ROM). Specimens were polished by using electrolytic polishing machine (make- Eletropol Metatech) in an electrolyte solution consisted of Methanol-730 ml, Butyl Cellosolve- 98ml, Perchloric acid-78 ml and Distilled water-100ml. Additionally, the etching was carried out using Keller's reagent for revealing grain boundaries of matrix. Microstructures were observed using optical microscope (make Carl Zeiss) and Scanning electron microscope (SEM) and Energy Dispersive Spectroscopy (EDS) techniques (make-JOEL, Japan) for spot analysis. The phase analysis was done by XPERT-PRO X-ray diffractometer (Copper target, K-alpha-1.54060Å). Bulk hardness was measured on Rockwell H-scale (HRH) with a 60 kg load and 1/8 inch ball indenter. The dimensions (height and diameter) were measured using Mitutoyo digital micrometer having least count of 1 μm . For cylindrical samples, diameter was checked at three positions top, middle and end along

INFLUENCE OF PROCESS CONDITION ON SINTERABILITY OF A PREMIX Al-Si ALLOY

longitudinal direction. The hardness and dimensional changes reported in this paper were resulted from average.

Result and Discussion

Fig. 1 (a) shows the effect of variation in mixing period and sintering time on the sintered density at constant pressure of 250MPa. It indicates that there is homogenous mixing of powder as the sintering period increased till 6 h. This give rise to increase in density till 6 h milling period but hardness remains unchanged as shown in Fig. 1 a and b. However beyond 6 h, sintered density drastically drops which is attributed to high strain energy associated with milled particles. This may entrap gases in the pores due to increase necking of particles and thus undergo expansion of the entrapped gases. Beyond 6 h milling time, the sintered compact does not show appreciable drop in hardness for 30 and 90 min sintered compact but marginal drop in hardness for 60 min sintered compacts. As the neck size ratio increases it does not allow entrapped gases to escape. It may be noted that as the mixing period increases there is reduction in particle size which leads to high grain coordination thereby inhibits densification [12].

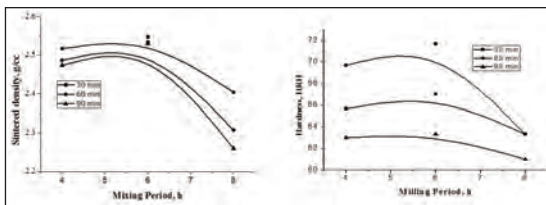


Fig. 1: Effect of milling period on (a) sintered density and (b) hardness for varying sintering period (sintered at 560 °C)

Effect of mixing period on and sintering time on Microstructure

Comparative study of milling period and sintering time on microstructural basis is carried out in this section. Effect of sintering

time on 4 h, 6 h, 8 h milled powder is explained in the subsequent sub section.

(a) Effect of sintering time on 4 h milled powder

(b) Fig. 2(a) shows the microstructure of 4 h mixed and 30 min sintered specimen. It is observed that there is non uniform distribution of copper and also there is some amount of porosity present. This might be due to insufficient mixing and sintering time. Further increasing the sintering time to 60 min there is significant grain boundary migration observed. On further increasing sintering time occurrence of grain growth and rounding of particles is observed

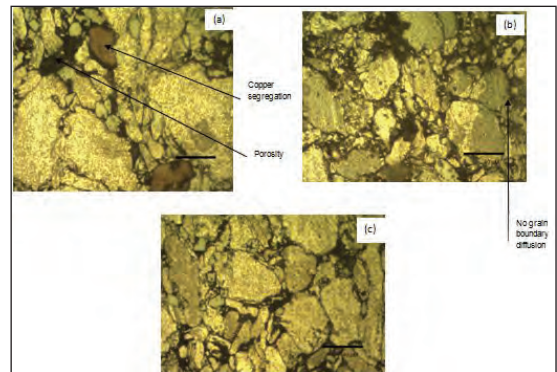


Fig. 2 : Microstructure of 4 h mixed, (a) Indicating no uniform distribution of copper and porosity for 30 min sintered specimen (b) 60min sintered specimen indicating no surface diffusion due to insufficient grain boundary energy (c) 90 min sintered specimen showing necking and diffusion of particles

(b) Effect of sintering time on 6 h milled powder

As mixing period is increased to 6 h, there is substantially uniform powder mixing of alloys and also straining of particles thereby increasing the surface energy. It is evident from microstructure as shown in Fig 3.(b) that

INFLUENCE OF PROCESS CONDITION ON SINTERABILITY OF A PREMIX Al-Si ALLOY

the particles are getting merged with each other by annihilating substantial discontinuity along the particle periphery. As the sintering period is further increased to 60 min there is subgrain evolution and closing of the pores thus results in densification and increase in hardness as evident in Figs 3.(c). At 90 min sintering period, it give rise to expansion of gases in the entrapped pores thereby overall increase in volume. This results in decrease in density as well as decrease in hardness as shown in Fig. 1. Besides such sub-grains undergo polygonisation which lead to grain growth.

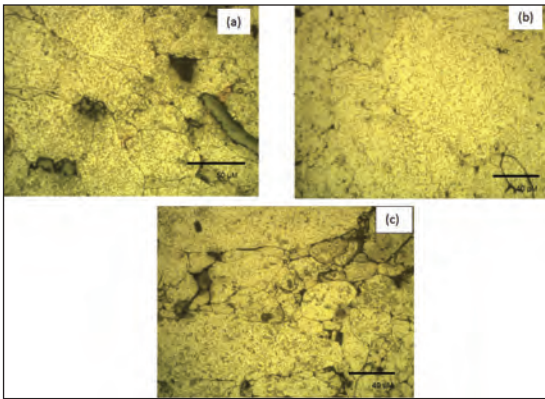


Fig. 3 : Microstructure of 6 h mixed, (a) showing merging of particles 30 min sintered specimen (b) showing grain growth and closed pores, 60 min sintered specimen (c) showing rounding of the particles and isolated pores, 90 min sintered specimen

(c) Effect of sintering time on 8 h milled powder

Fig. 4 (a) shows the effect on 8 h milled powder sintered for 30 min. As mixing period is further increased to 8 h, the particles have undergone severe deformation. During sintering, the elongated deformed particles undergo neck formation at early stage thereby entrapment of gases at junction of the particles. Thus leading to decrease in density

and hardness as shown in Fig. 1 (a) and (b). Fig. 4(b) shows the effect mixing period of 8 h and 60 min sintering time. As the sintering period is increased to 60 min, strain relieving takes place by grain growth and rounding of the particle and leading to pore growth. It is seen from Fig. 1 (a) that as the sintering time is increased to 60 min, there is decrease in density. As the sintering period is further increased to 90 min, it leads to polygonisation of the subgrains. Also there is drastic drop in the sintered density accompanied by marginal effect on hardness of specimen as shown in the Fig. 1. Thus grain coarsening, rounding of particle shape and expansion of circular pores led to drop in density as evident from Fig. 5 as mixing period is increased to 6 h, there is substantially uniform powder mixing of alloys and also straining of particles there by increasing the surface energy. It is evident from microstructure as shown in Fig. 3.(b) that the particles are getting merged with each other, by annihilating substantial discontinuity along the particle periphery. As the sintering period is further increased to 60 min there is subgrain evolution and closing of the pores thus results in densification and increase in hardness as evident in Figs 3 (c). At 90 min sintering period, it give rise to expansion of gases in the entrapped pores thereby overall increase in volume. This result in decrease in density.

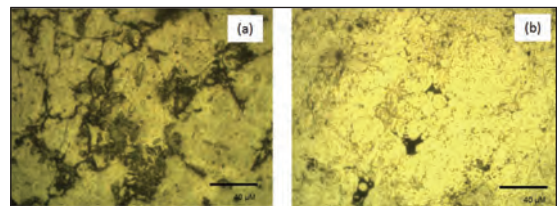


Fig. 4 : Microstructure of 8 h mixed, (a) showing entrapped gases and highly strained particles for, 30 min sintered specimen (b) showing grain growth and closed pores, 60 min sintered specimen

INFLUENCE OF PROCESS CONDITION ON SINTERABILITY OF A PREMIX Al-Si ALLOY

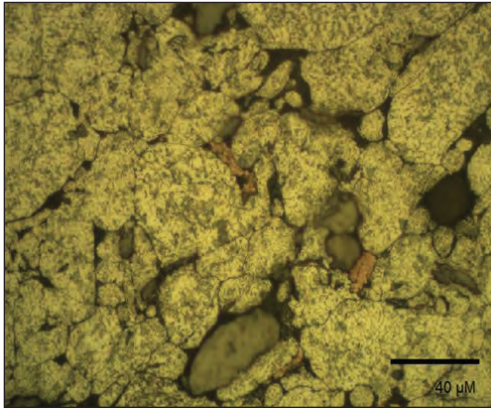


Fig. 5 : Microstructure of 8 h mixed (c) showing rounding of the particles and isolated pores, 90 min sintered specimen

Effect of Compaction Pressure

Specimens were compacted at various pressures and sintered at 560°C. The sintering period was 30 to 60 min with time interval of 15 min followed by water quenching. It is observed from Fig. 6 that the green density is maximum for samples compacted at 400 MPa. On further increasing compaction pressure, few minor cracks were observed on green compacts which might have occurred due to excessive plastic deformation that exceeds the fracture strength of the material and hence it leads to crack formation

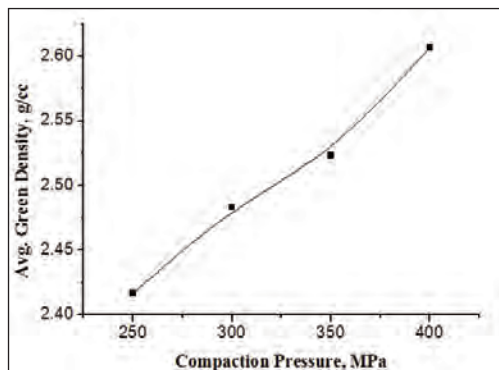


Fig. 6 : Effect of Compaction pressure on green density

Due to low compacting pressure of 250 MPa, the premix alloy powder is loosely compacted and hence less surface contact i.e neck contacts which gives rise to high amount of porosity (see Fig. 7). During solidification of hypoeutectic Al-Si alloys, primary Al dendrites nucleate at the liquidus temperature and β (Al, Si, Fe) particles in the solute field ahead of these growing dendrites at a temperature or slightly above the eutectic temperature of the alloy. Eutectic Si nucleates on β (Al, Si, Fe) particles and eutectic Al nucleates on the eutectic silicon as evident in Fig.7, which is compacted at 250 MPa and sintered 30 min.



It is observed that there is no continuous phase formation along the particle boundary. Presence of β (AlSiFe) phase is confirmed by the EDS spectrum at location EDS spot 1 as shown in Fig. 8 and the presence of eutectic phase along the α -Al grain is indicated by EDS 2 as shown in Fig.9. Eutectic phase is segregated along the grain boundary at small area which may be due to merging of particles.

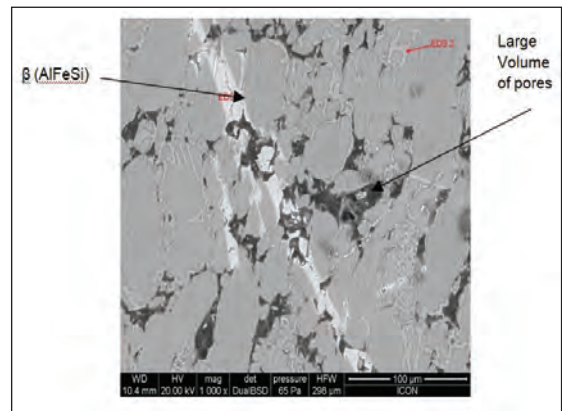


Fig. 7: SEM image (250MPa,30 min) Sintered specimen showing distinct needles of β (AlFeSi)

INFLUENCE OF PROCESS CONDITION ON SINTERABILITY OF A PREMIX Al-Si ALLOY

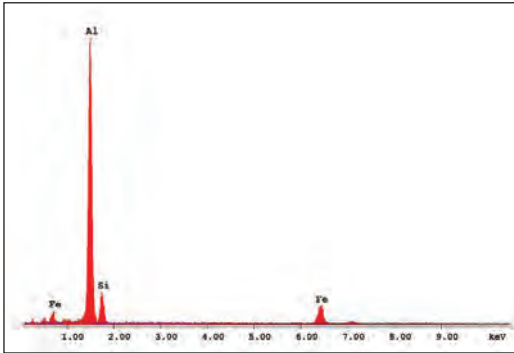


Fig. 8: EDS 1 Spectrum of phase in showing needles of $\beta(\text{AlSiFe})$

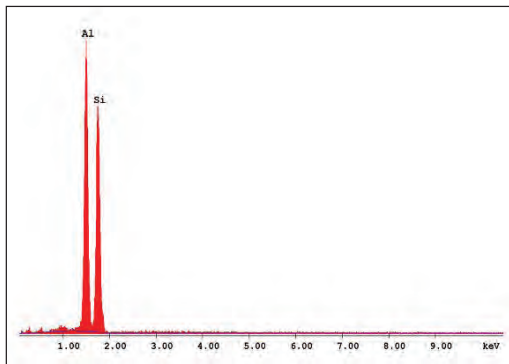


Fig. 9: EDS 2 Spectrum of phase in showing a Al+Si along the grain boundary

At higher compacting pressure of 400 MPa, deformed particles remain in immediate contact with each other thereby enhancing mass transport of atomic species due to large driving force. Compared to earlier observations, particles surrounded by liquid phase eutectic precipitated is the distinct observation noted for specimen compacted at 400 MPa. Besides, particles are having rounded morphology as indicated from Fig. 10. Fig. 11 shows the SEM image of 400 MPa compacted and 30 min sintered specimen. It is observed that there is uniform distribution of eutectic mixture of Al and Cu with some amount of Si along the grain boundaries of α -Al grain. Uniform distribution of liquid phase along the grain boundary results in rounding of Al particles.

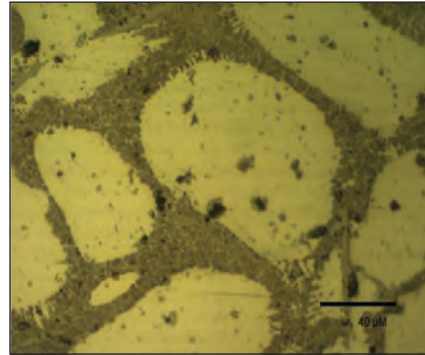


Fig. 10: Optical microstructure showing rounded Al particles surrounded by eutectic mixture

It is observed that there is significant density and hardness is obtained at this compaction pressure and sintering period. This is due to increase in the eutectic mixture of Al and Cu which enhances strength of the compact. The precipitation of Al-Cu phase along the grain boundary inhibits the motion of dislocations by formation of solid state solution [13]. On the other hand, it is observed that there are sharp needles of $\beta(\text{AlSiFe})$ phase which are brittle in nature leading to reduce strength. The overall microstructure consists of $\beta(\text{AlSiFe})$, eutectic mixture and α -Al grains as confirmed by EDS spot analysis given in Fig.12 (a), (b) and (c) respectively.

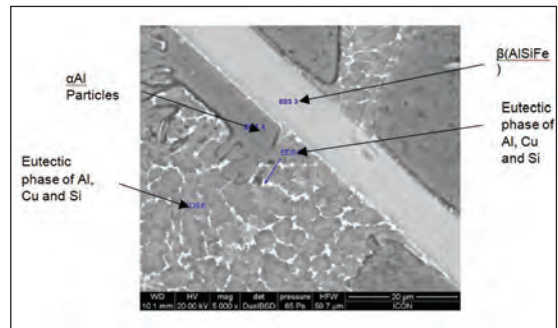


Fig. 11: SEM image of specimen compacted at 400 MPa and sintered for 30 min showing Al particles surrounded by eutectoid mixture and needles of $\beta(\text{AlSiFe})$

INFLUENCE OF PROCESS CONDITION ON SINTERABILITY OF A PREMIX Al-Si ALLOY

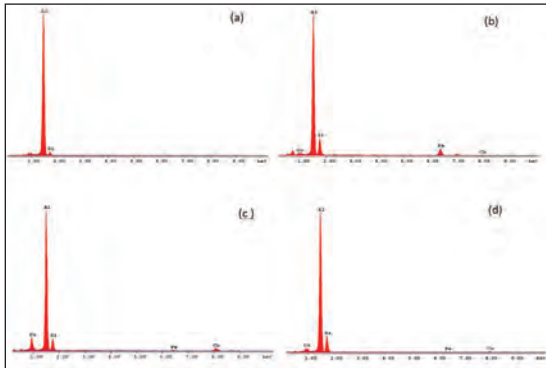


Fig. 12 : (a)EDS 3 spectrum of phase in Fig.11 showing β (AlSiFe) phase, (b) EDS 4 Spectrum of phase in Fig. 11 showing α Al phase (c) EDS 5 Spectrum of phase in Fig. 11 showing Eutectic mixture (d) EDS 5 Spectrum of phase in showing Eutectic mixture

Conclusion:

1. The premix composition blended for 6 h showed with maximum density of 2.54 g/cc for 30 min sintered compact. On further increasing the mixing period to 8 h the density decreases to 2.28 g/cc for the same compacting pressure
2. Increasing compacting pressure from 250 MPa to 400 MPa gives rise to evolution of new phase such as eutectic mixture (250 MPa), β (AlFeSi) and eutectic mixture (350 MPa) and β (AlFeSi), eutectic mixture along with phase (400 MPa). This is attributed to enhanced atomic mass diffusion across the particles boundaries.

Reference:

- [1] M. Gupta*, S. Ling, Microstructure and mechanical properties of hypo/ hyper-eutectic Al-Si alloys synthesized using a near-net shape forming technique, *Journal of Alloys and Compounds* 287 (1999) 284-294
- [2] T. Okada, M. Toriyama, S. Kanzaki, Direct nitridation of aluminum compacts at low temperature, *Journal of materials science* 35 (2000) 3105 - 3111
- [3] G.B. Schaffer, T.B. Sercombe, R.N.Lumley, Liquid phase sintering of aluminium alloys, *Materials Chemistry and Physics* 67 (2001) 85-91
- [4] Patama Visuttipitukul¹, Tatsuhiko Aizawa¹ and Hideyuki Kuwahara², *Advanced Plasma Nitriding for Aluminum and Aluminum Alloys*, *Materials Transactions*, Vol. 44, No. 12 (2003) pp. 2695 to 2700
- [5] Guoqiang Xie^{1*}, Osamu Ohashi¹, Takahiro Sato¹, Norio Yamaguchi¹, Minghui Song², Kazutaka Mitsuishi² and Kazuo Furuya², *Effect of Mg on the Sintering of Al-Mg Alloy Powders by Pulse Electric-Current Sintering Process*, *Materials Transactions*, Vol. 45, No. 3 (2004) pp. 904 to 909 #2004 The Japan Institute of Metals
- [6] D. Casellas, A. Beltran, J.M. Prado, A. Larson, A. Romero, *Microstructural effects on the dry wear resistance of powder metallurgy Al-Si alloys*, *Wear* 257 (2004) 730-739
- [7] G.B. Schaffer, *Powder processed aluminium alloys*, *Materials Forum* 28 (2004) 65-74
- [8] Shankar S. , Riddle Y. W. , Makhlof, Makhlof M. (2004). *Eutectic Solidification of Aluminum-Silicon Alloys*. *Metallurgical and Materials Transactions A-Physical Metallurgy and Materials Science*, 35A(9), 3038-3043
- [9] N. Showaiter and M. Youseffi, *Compaction, Sintering and Mechanical Properties of Elemental 6061 Al Powder with and without Sintering Aids*, *Journal of Materials and Design* Vol. 29, No. 4, 2008, pp. 752-762.
- [10] M. Rahimian, N. Ehsania, N. Parvin and H. Baharvandi, *The Effect of Particle Size, Sintering Temperature and Sintering Time on the Properties of Al-Al₂O₃ Composites, Made by Powder Metallurgy*, *Journal of Material Proc-essing Technology*, Vol. 209, No. 14, 2009, pp. 5387- 5393
- [11] Haris Rudianto^{1,2}, Sangsun Yang¹, Ki-Woo Nam² and Yong-Jin Kim¹, *Mechanical properties of al-14si-2.5cu-0.5mg Aluminum-silicon p/m alloy*, *Rev.Adv.Mater.Sci.*28 (2011) 145-149

INFLUENCE OF PROCESS CONDITION ON SINTERABILITY OF A PREMIX Al-Si ALLOY

- [12] S.Solay Anand^{1*}, B.Mohan², T.R.Parthasarathy³,
Effect of Slow Cooling in Reducing Pore Size
in a Sintered Powder Metallurgical 6061
Aluminium Alloy, Materials Sciences and
Application, 2011, 2, 870-877
- [13] Azim Gokce, Fehim Findik, Ali Osman Kurt,
Microstructural examination and properties of
premixed Al-Cu-Mg powder metallurgy alloy,
Materials Characterization 62 (2011) 730-735
- [14] Haris Rudianto^{1,2}, Sangsun Yang¹, Ki-Woo
Nam² and Yong-Jin Kim¹, Sintering behavior of
hypereutectic aluminum-silicon metal matrix
composites powder, Advanced Materials
Development and Performance (AMDP2011)
International Journal of Modern Physics:
Conference Series Vol. 6 (2012) 628-633
- [15] A. Manonukul^{1*}, A. Salee², Relationship between
Atmospheric Dew Point and Sinterability of
AlSi Based Alloy, J. Mater. Sci. Technol., 2013,
29(1), 70-76
- [16] N. B. Dhokey^{1*}, V. A. Athavale¹, N. Narkhede²,
M. Kamble, Effect of processing conditions on
transient liquid phase sintering of premixed
aluminium alloy powders, Adv. Mat. Lett.
2013, 4(3), 235-240. (Add second paper as well).

DEVELOPMENT OF Al-NANO SiC COMPOSITES THROUGH POWDER METALLURGY ROUTE AND TESTING THEIR MECHANICAL PROPERTIES

Gaurav Bajpai¹, Rajesh Purohit², R. S. Rana² and Akshat Patil³

¹Indian Institute of Technology, Indore, India

²Maulana Azad National Institute of Technology, Bhopal, India

³NRI Institute of Science and Technology, Bhopal, India

Abstract

In present scenario weight reduction and strength enhancement is the main concerns, for increasing the use of composite materials in various industries. Today composite materials are widely used in several industries such as automobile, aerospace, defence, insulator and radar domes. They find widespread applications in various systems viz. mechanical, structural, tribological, electromagnetic etc. Metal matrix composites are light-weight, having high strength and wear resistance. Metal matrix composites are composed of a metallic base material which is reinforced with ceramic fibre, whisker or particulate as reinforcement material. In the present work nano-SiC particulates have been used as reinforcement in aluminium metal matrix with different weight % of Nano SiC. The composites were fabricated using powder metallurgy process through cold isostatic compaction chamber. The various properties viz. hardness, density, porosity, compressive strength and indirect tensile strength were measured. The microstructure of polished and etched surfaces of powder metal Al-Nano SiC composite samples was studied using scanning electron microscope. Micrograph shows the uniform distribution of Nano SiC particles in the Aluminum matrix.

Key words: Cold isostatic compaction (CIP), Al-Nano SiC composites, Powder metallurgy process, Scanning electron microscope.

1. Introduction:

The increasing demand for light weight, high strength materials in technologically advanced industries supported by the advances in the field of material science. Due to their light-weight, high strength, stiffness and resistance to high temperature, aluminum based metal matrix composites (MMCs) have been extensively used for automotive, aerospace and military applications [1]. The reinforcement of silicon carbide (SiC), boron carbide (B₄C) and aluminum oxide (Al₂O₃) in MMCs have significant advantage over conventional materials. Generally, the micron size ceramic particles are used to improve the yield and ultimate strength of the metals or alloys. However the ductility of the MMCs decreases

with high ceramic particle concentration. Nano-particle reinforcements can significantly improve the mechanical properties of the matrix by more effectively promoting the particle hardening mechanisms than micron size particles [2]. It is expected that MMCs reinforced with ceramic nanoparticles (less than 100 nm), termed as metal matrix nanocomposites (MMNCs), can overcome those disadvantages associated with the conventional MMCs. The properties of MMNCs is improved considerably even with lower volume fraction of nano-particles. MMNCs can provide significantly improved performance at elevated temperatures [3]. Therefore Al nano SiC composites have seen most wide spread applications because of their tailorable

DEVELOPMENT OF Al-NANO SiC COMPOSITES THROUGH POWDER METALLURGY ROUTE AND TESTING THEIR MECHANICAL PROPERTIES

properties, good forming characteristics and the availability of comparatively low cost, high volume production methods.

There are various methods used for fabrication of Al matrix nano-composites like infiltration^[4], squeeze casting^[5], mechanical alloying^[6], powder metallurgy^[7], ball milling^[8], and stir casting^[9]. Nevertheless powder metallurgy is one of the best technique because, it is relatively inexpensive, and offers a wide variety of material and processing conditions. Powder metallurgy (PM) is a widely used fabrication method for producing metal matrix composites. This usually involves three major stages: blending of the metal and ceramic powders, pressing or cold compaction, and sintering. The last two steps are often combined in hot pressing. Although PM allows to produce components with complex geometries in bulk, there are some disadvantages associated with conventional powder metallurgy such as porosity and segregation of the reinforcing particles between the metal matrix particles. This often leads to degradation of the mechanical properties. These problems become more important when the difference in particle size between the reinforcement and the matrix alloy powders is large or when the volume fraction of the reinforcement is high^[10]. Rolling, forging or extrusion followed by heat treatment is often applied to eliminate defects such as porosity or particle segregation, and improve the physical and mechanical properties of metal matrix composites produced by powder metallurgy process^[11]. For example, the combination of conventional powder metallurgy and extrusion offer several advantages including strengthening due to grain refinement, homogenization of the distribution of the secondary particles, higher productivity, and lower costs^[12]. To this end, Lee et al. have shown that extrusion and forging of a powder metallurgy fabricated Al/SiC composite resulted in an increase

from 71 to 430 MPa in tensile strength and an increase from 29 to 103 HV in hardness^[13] and Smagorinski et al. have indicated that rolling can completely eliminate pores in PM composites^[14]. Yang et al.^[15] studied the effect of nano sized SiC particles reinforced in molten aluminium alloy by ultrasonic dispersion. Lan et al.^[16] reported the studies on microstructure and microhardness of SiC nano particles reinforced magnesium composites fabricated by ultrasonic method. Rostamzadeh et al.^[17] studied Al-5 (Vol.) % SiC_p nano-composite powder has been successfully synthesized by high-energy planetary milling of Al and SiC powders for a period of 25 h and reported that nano-composite powders were composed of near-spherical particles and moreover, the SiC particles were uniformly distributed in the aluminum matrix. Mazahery et al.^[18] did work on the A356 aluminum alloy reinforced with nano SiC particles through stir casting and reported that yield strength, ultimate tensile strength and the elastic modulus were improved and ductility decreased with the addition of nano particles. They also observed that the highest yield strength and ultimate tensile strength were obtained with the addition of 3.5% SiC nano-particles. There is very less research available in the fabrication of nano SiC composites through powder metallurgy process till now.

2. Fabrication of Al-nano SiC composites through powder metallurgy process

Standard samples of Al-nano SiC composites with 1, 2 and 3 weight % of nano SiC were fabricated through powder metallurgy route.

2.1 Particle Size analysis of the powders

Aluminum powder of approximate 50 μm size range and nano SiC particulates of about 40 to 90 nm were taken separately and used in the present work. Fig. 1 shows scanning electron micrograph of the aluminum powder & Fig. 2 shows Transmission electron micrograph of

DEVELOPMENT OF Al-NANO SiC COMPOSITES THROUGH POWDER METALLURGY ROUTE AND TESTING THEIR MECHANICAL PROPERTIES

Nano SiC particles. The micrographs show that the aluminum powders are of about 50 μm size range and the nano SiC particulates are of about 40 to 90 nm size.

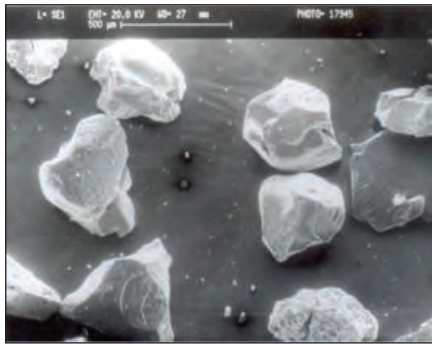


Fig. 1 Scanning electron micrograph of the aluminum powder

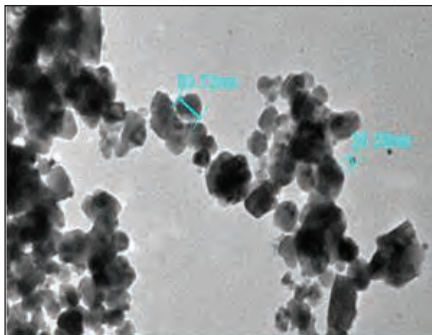


Fig. 2 Transmission electron micrograph of Nano SiC particles

2.2 Mixing of powders

After particle size analysis, aluminium & nano SiC powders were weighed individually and mixtures of three different compositions (viz. 1, 2 and 3 weight percent of nano SiC) were prepared. The mixtures were put in plastic containers and mixing was done manually for half an hour to ensure proper mixing.

2.3 Mechanical alloying

Mechanical alloying results in mixing at molecular level. The nano SiC particles got embedded into Al powder particles and

powder particles of Al-nano SiC composite have been obtained. The powder mixtures were transferred to horizontal ball mill. Fig. 3 shows photograph of the horizontal ball mill. The horizontal ball mill already contained the hardened steel balls as milling media. In order to minimize the extreme tendency of aluminum to get self welded during milling, 2.0 wt. % of ethyl acetate was added as process control agent. The milling was performed in argon atmosphere to prevent contamination from atmospheric air. The ball milling done with speed of 100 rpm for 8 hours. The powder became hot during milling therefore it was allowed to cool for 3-4 hours, then it was taken out of the ball mill and stored in plastic containers.



Fig. 3 Photograph of the horizontal ball mill

2.4 Mould Cavity

For the manual compaction of Al nano SiC composites in the shape of solid cylindrical pins of 15 mm diameter and 25 mm length, a die and punch of mild steel have been fabricated. The die was lubricated to ensure easy extraction of the powder compacts. The Al nano SiC composite powders of weighed amount were mixed with 2.0 wt. % ethyl acetate & Gum and poured into the die. The powder compact was ejected out of the die and put in a flexible mould and its mouth was tied tightly with the help of a string. The flexible mould should be of appropriate size in order

DEVELOPMENT OF Al-NANO SiC COMPOSITES THROUGH POWDER METALLURGY ROUTE AND TESTING THEIR MECHANICAL PROPERTIES

to avoid wrinkles on the mould surface. The flexible mould should be 100 percent leak proof to prevent the leakage of oil into the powder sample during iso-static compaction. Al nano SiC composite specimens were fabricated with ball milled powder samples with 1, 2 & 3 weight % of nano SiC particulates.

2.5 Cold Isostatic Compaction

CIP is a compaction process in which iso-static fluid pressure is applied to a powder mass at room temperature to compact it into desired shape. The powder parts can be compacted up to 80-95% of their theoretical densities. Water or oil can be used as pressurizing medium. High density near-net shape green compacts, long thin walled cylinders, parts with undercuts can be readily fabricated. In this process, pressure is applied simultaneously and equally in all directions using a liquid medium with powder in flexible mould at room temperature. Cold Isostatic compaction process results in better and more uniform properties as compared to die compaction because of uniform application of pressure from all directions and absence of die wall friction.

2.6 Sintering of Al-nano SiC Compacts

The cold iso-statically pressed green compacts were sintered in a programmable argon atmosphere furnace by gradually raising the temperature to 645°C and the specimens were kept at this temperature for 1 hour and 25 minutes. The compacts were furnace cooled. Sintering was performed in continuous flow of argon gas.

3. Testing of properties

3.1 Hardness

Rockwell hardness was measured on the polished surfaces of the Alnano SiC composite samples using B scale on Rockwell hardness tester. A 1/16 inch hardened steel ball indenter with fixed indentation load of 100 kg was used for all tests. Five readings were taken for the

samples of each composition and the average hardness was determined. Fig. 4 shows Digital Rockwell cum Brinell hardness tester.



Fig. 4 Digital Rockwell cum Brinell hardness tester

3.2 Porosity

Porosity of the sintered as well as un-sintered compacts was determined by Archimedes principle. The compacts were first weighed in air and then tied with string and weighed while hanging in water. The density was determined using the following formula:

$$\rho_s = (m_a \times \rho_w) / (m_a - m_w) \text{ ----- (1)}$$

Where,

ρ_s = Density of sintered specimen (gm/ cm³)

ρ_w = Density of water (gm/ cm³)

m_a = Weight of sample in air (gm)

m_w = Weight of sample in water (gm).

The porosity was determined using the following formula:

$$E = 1 - \rho_s / \rho_t \text{ ----- (2)}$$

Where,

E = porosity (%)

ρ_s = Density of sintered part (gm/cm³)

ρ_t = Theoretical density (gm/cm³)

DEVELOPMENT OF Al-NANO SiC COMPOSITES THROUGH POWDER METALLURGY ROUTE AND TESTING THEIR MECHANICAL PROPERTIES

The theoretical density was determined by comparing the sum of volume (weight divided by the density) of constituents and the volume of composite. For example, the density of Al-3 wt. % nano SiC composites was determined as follows:

Density of SiC = 3.7 gm/cm³

Density of aluminum = 2.7 gm/cm³

$$\frac{100}{\rho} = \frac{3}{3.7} + \frac{97}{2.7} \text{-----} (3)$$

Which gives the theoretical density (ρ) for Al-3 wt. % nano composites:

$$\rho = 2.722 \text{ gm/cm}^3$$

Similarly the theoretical densities of other compositions of Al nano SiC composites were determined.

3.3 Compressive Strength

Compression test was performed on Al-nano SiC composites specimens with length to diameter ratio of 1.5. Tests were performed on Computerized UTM of 1000 KN capacity. The sample was compressed between two flat platens and the maximum failure load was recorded.

3.4 Indirect Tensile Strength

The indirect tensile strength of the powder metal Al- nano SiC composites with 1, 2 and 3 weight % of nano SiC were measured. For this purpose Al-nano SiC composite samples of right circular cylindrical shape were fabricated by powder metallurgy process. The indirect tensile strength was measured on 1000 KN universal testing machine. In this test a right circular cylinder is compressed diametrically between two flat plates. The maximum tensile stress is developed normal to the loading direction with a constant magnitude between two lines of contact. The tensile stress G is given by

$$G = 2P / \pi.d.t \text{-----} (4)$$

Where,

P = Applied load (N)

d = Specimen diameter (m)

t = Specimen thickness (m)

3.5 Microstructural Analysis

The microstructures of the Al nano SiC composites were studied using scanning electron microscope. For this purpose small samples were cut from the cylindrical pins fabricated by powder metallurgy process. The samples were first machined on lathe and then polished using polishing papers of gradually increasing fineness. The polished samples were then lapped on polishing machine using diamond-lapping paste and velvet cloth for about 40 minutes so that mirror finish is obtained on the samples. The samples were etched with 1 % Keller Reagent for about 45 seconds and washed with distilled water before the microstructural analysis. Then the scanning electron micrographs of powder metal Al- Nano SiC composite samples with 1 to 3 weight % of Nano SiC were taken and studied for microstructural analysis.

4. Results and Discussions:

The Rockwell hardness, density, porosity, compressive strength and indirect tensile strength of Al-nano SiC composites were measured. The microstructural analysis was also done.

4.1 Rockwell hardness

The Rockwell hardness (B scale) of the Al-nano SiC composites are shown in the Fig.5. This depicts that the Rockwell hardness of Al- 2.0 wt. % Nano SiC Composites is more than that of the Al- 3.0 wt. % Nano SiC Composites. This is because of the clustering of nano alumina particles at higher weight percent, which reduces hardness.

DEVELOPMENT OF Al-NANO SiC COMPOSITES THROUGH POWDER METALLURGY ROUTE AND TESTING THEIR MECHANICAL PROPERTIES

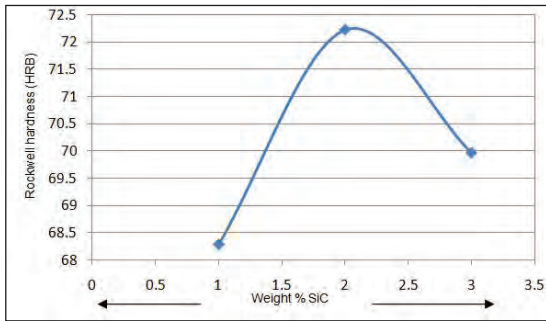


Fig. 5 Rockwell hardness of iso-statically pressed Al-Nano SiC composites

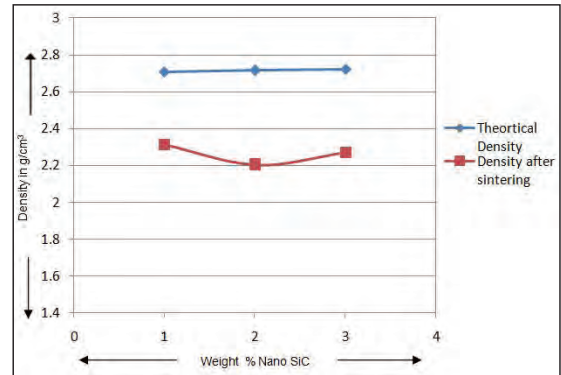


Fig. 7 Density of sintered Al - Nano SiC composites

4.2 Porosity

The density and porosity of Al-nano SiC composites were measured before as well as after the sintering. The experimental density, theoretical density and porosity of Al- Nano SiC Composites before and after sintering are measured and graph is plotted in Fig.6, Fig.7 and Fig.8 respectively. These figures show that the density increases with increase in wt. % of nano SiC because the density of SiC is higher than aluminum. This is because the volatile material like ethyl acetate, moisture etc. are evaporated and relieving of residual compressive stresses (obtained while compaction), during sintering which results in density reduction and hence increase in porosity.

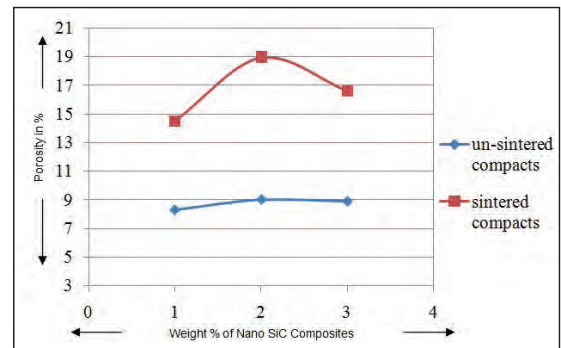


Fig. 8 Porosity of Al-Nano SiC composites in sintered & un-sintered conditions

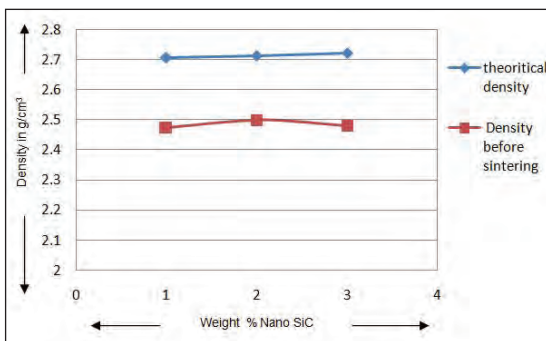


Fig. 6 Density of un-sintered Al - Nano SiC Composites

4.3 Compressive strength

The compressive strength of Al-nano SiC composites measured on universal testing machine. Fig. 9 shows Compressive strength of Al-Nano SiC Composites. As it is illustrated, Al-2.0 wt. % Nano SiC Composites have higher compressive strength than Al-3.0 wt.% Nano SiC Composites. This is because of clustering of very fine nano SiC particles at higher reinforcement content which reduces the amount of effective nano particles available and the particle strengthening effect diminishes.

DEVELOPMENT OF Al-NANO SiC COMPOSITES THROUGH POWDER METALLURGY ROUTE AND TESTING THEIR MECHANICAL PROPERTIES

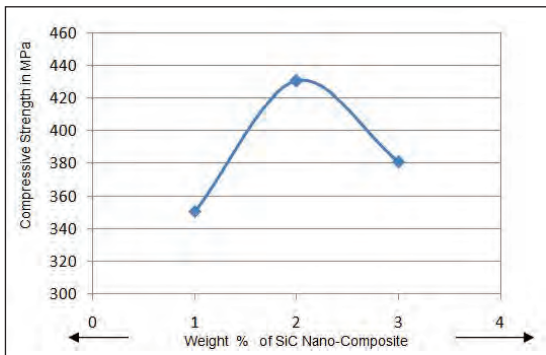


Fig. 9 Compressive strength of Al-Nano SiC Composites

4.4 Indirect tensile strength

The indirect tensile strength of Al-nano SiC composites measured on universal testing machine. Fig. 10 shows that Al-2.0 wt. % nano SiC Composites has higher tensile strength than Al-3.0 wt. % nano SiC Composites. This is because of clustering of very fine nano SiC particles at higher reinforcement content.

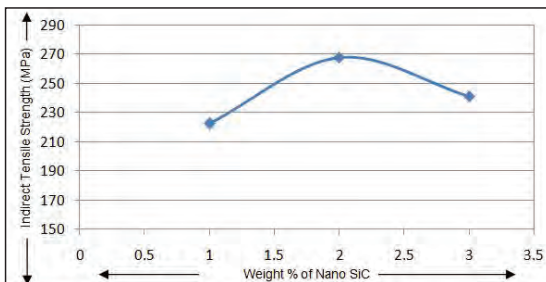


Fig. 10 Indirect Tensile strength of sintered Al-Nano SiC Composites

Clustering of nano particles causes stress concentration and hence provides sites for crack initiation which reduces the strength. The strength of nano composites was influenced by several factors such as

- Milling consequent deformation and work hardening.
- Increase in dislocation density because of difference in thermal expansion coefficient of aluminum and alumina particles.

- Grain refinement and sub grain production because of increase in dislocation density.
- Distribution of SiC particles.

4.5 Microstructural Analysis

4.5.1 SEM Analysis of Un-Sintered Al-1, 2 & 3 wt.% Nano SiC Composites

Fig. 11(a) shows SEM Image of Al-1 wt. % nano SiC Composite before sintering. This image shows that the Al-nano SiC are not properly bonded to each other before sintering and some moisture is present. Fig.11(b) shows SEM Image of Al-2 wt. % Nano SiC Composite before sintering. This image also shows that the Al-nano SiC are not properly bonded to each other. The SEM images show that nano particles are uniformly distributed in the aluminum matrix. Fig.11(c) shows SEM Image of Al-3 wt.% Nano SiC Composite before sintering. This image shows that there is clustering of nano particles at some of the places.

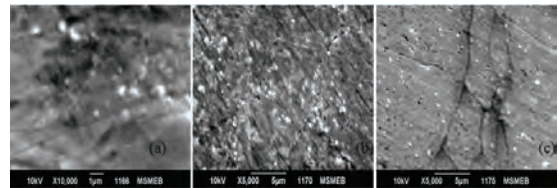


Fig.11 (a) SEM Image of Al-1 wt. % nano SiC Composite before sintering, (b) SEM Image of Al-2 wt. % Nano SiC Composite before sintering and (c) SEM Image of Al-3 wt. % Nano SiC Composite before sintering

4.5.2 SEM Analysis of Sintered Al-1, 2 & 3 wt. % Nano SiC Composites

The etched and dried specimens were prepared and subsequently mounted on specially designed aluminum stubs using holder. The specimens thus mounted were viewed under Jeol JSM 6510 LV scanning electron microscope at a voltage of 10 kV. Fig.12 (a), 12 (b) and 12(c) show the SEM micrograph of the different Al-

DEVELOPMENT OF Al-NANO SiC COMPOSITES THROUGH POWDER METALLURGY ROUTE AND TESTING THEIR MECHANICAL PROPERTIES

nano SiC composites. Fig.12 (a) shows SEM image of Al-1 wt. % nano SiC Composite. This image shows that the Al-nano SiC are properly bonded to each other. Fig. 12 (b) shows SEM image of Al-2 wt. % nano SiC Composite. This image also shows that the Al-nano SiC are properly bonded to each other but some extent greater than former one. The SEM images show that nano particles are uniformly distributed in the aluminum matrix. Fig. 12 (c) shows SEM image of Al-3 wt. % Nano SiC Composite. This image shows that there is clustering of nano particles at some of the places.

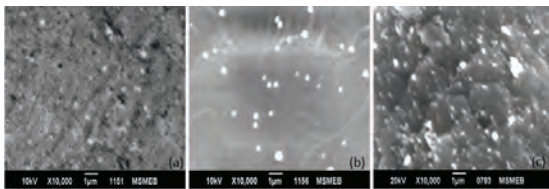


Fig. 12 (a) SEM Image of Al-1 wt. % Nano SiC Composite after sintering (b) SEM Image of Al-2 wt. % Nano SiC Composite after sintering, and (c) SEM Image of Al-3 wt. % Nano SiC Composite after sintering

5. Conclusions:

1. Mechanical alloying of aluminum and Nano SiC powders for 8 hours of ball milling resulted in fine homogeneous equiaxed nano composite powder structure.
2. Cold isostatic compaction at 600 MPa followed by Argon Atmosphere sintering at 645°C has been successfully used to produce Al- Nano SiC composites.
3. During Cold isostatic compaction of powders, the quality of final product depends upon the quality of initial manual compact; therefore the manual compact should be prepared carefully and should be given proper allowances in dimensions to get the desired final product.

4. The tensile strength, compressive strength and hardness of Al-Nano SiC composites first increases up to 2 wt. % nano SiC and then decrease at 3 wt. % of nano SiC reinforcement. This is because of clustering (agglomeration) of nano SiC particles at higher weight percent. The clustering of nano particles reduces the amount of effective nano particles available and hence the strength and hardness decreases.
5. Scanning electron micrographs of powder metal Al-nano SiC composites reveals that the Argon atmosphere sintering results in proper bonding between aluminium and nano SiC particles. The micrographs also show uniform distribution of nano SiC particulates in aluminium matrix up to 2 wt. % Nano SiC and some amount of porosity was observed.

References:

- [1] N. Mohd Abbas, D.G. Solomon, Md. Faud Bahari, A review on current research trends in electric discharge machining, International Journal of Machining & Tool Manufacturing 47 (2006) ,1214–1228.
- [2] R.K. Garg, K.K. Singh, Anish Sachdeva, Vishal S. Sharma, Kuldeep Ojha, Sharanjit Singh, Review of research work in sinking EDM and WEDM on metal matrix composite materials, International Journal of Advanced Manufacturing Technology 50 (2010), 799–809.
- [3] I. Narasimha Murthy, D. Venkata Rao, J. Babu Rao, Microstructure and mechanical properties of aluminium-flyash nanocomposites made by Ultrasonic method, Material & Design 35 (2012), 55–65.
- [4] Reyes M, Canul M, Torres J., Development of aluminum hydroxides in Al-Mg-Si/SiCp in infiltrated composites exposed to moist air, Journal of Ceramic International 37(2011), 12719–2722.
- [5] Li G, Zhao Y, Wang H, Chen G, Dai Q, Cheng X. Fabrication and properties of in situ (Al₃Zr + Al₂O₃) p/A356 composites cast by permanent

DEVELOPMENT OF Al-NANO SiC COMPOSITES THROUGH POWDER METALLURGY ROUTE AND TESTING THEIR MECHANICAL PROPERTIES

- mould and squeeze casting, *Journal of Alloys and Compound* 471(2009), 530-535.
- [6] Safari J, Chermahini M, Akbari G., The effect of Mg content on microstructure and mechanical properties of Al-xMg/5Al₂O₃ nanocomposite prepared by mechanical alloying, *Journal of Powder Technology*, 234(2013), 7-12.
- [7] Wang H, Jiang Q, Wang Y, Ma B, Zhao F., Fabrication of TiB₂ particulate reinforced magnesium matrix composites by powder metallurgy. *Journal of Material Letters*, 58(2004), 3509-3513.
- [8] Qu H, Zhu S, Li Q., Influence of sintering temperature and holding time on the densification, phase transformation, microstructure and properties of hot pressing WC-40 vol.% Al₂O₃ composites, *Journal of Ceramic International*, 38(2012), 1371-1380.
- [9] Naher S, Brabazon D, Looney L., Development and assessment of a new quickquench stir caster design for the production of metal matrix composites, *Journal of Material Processing & Technology*, 166(2004), 430-439.
- [10] Lee, J., Kim, N.J., Jung, J.Y., Lee, E.S., Ahn, S., The influence of reinforced particle fracture on strengthening of spray formed Cu-TiB₂ composite, *Scripta Materialia*, 39(1998), 1063-1069.
- [11] ASM Metals Handbook, Properties and Selection: Nonferrous Alloys and Special-Purpose Materials, ASM International, 2(1992).
- [12] Liu, Y.B., Lim, S.C., Lu, L., Lai, M.O., Recent development in the fabrication of metal matrix-particulate composites using powder metallurgy techniques. *Journal of Materials Science*, 29(1994), 1999-2007.
- [13] Lee, H.S., Yeo, J.S., Hong, S.H., Yoon, D.J., Na, K.H., The fabrication process and mechanical properties of SiC_p/Al-Si metal matrix composites for automobile air-conditioner compressor pistons. *Journal of Materials Processing Technology*, 113(2001), 202-208.
- [14] Smagorinski, M.E., Tsantrizos, P.G., Grenier, S., Cavasin, A., Brzezinski, T., Kim, G., The properties and microstructure of Al-based composites reinforced with ceramic particles, *Materials Science and Engineering, A* 244(1998), 86-90.
- [15] Yang Y., Lan J., Li X., Study on bulk aluminium matrix nano-composite fabricated by ultrasonic dispersion on nano sized SiC particles in molten aluminium alloy, *Materials Science and Engineering- A*, 380(2004), 378-383.
- [16] Lan J., Yang Y., Li X., Microstructure and microhardness of SiC nano particles reinforced magnesium composites fabricated by ultrasonic method, *Materials Science and Engineering- A*, 386(2004), 284-290.
- [17] T. Rostamzadeh1 and H. R. Shahverdi, Microstructure study on al-5%SiC nano composite powders, *Iranian Journal of Materials Science & Engineering*, 8(2011), 32-39.
- [18] A. Mazahery and M. O. Shabani, Characterization of cast A356 alloy reinforced with nano SiC composites, *Transactions of Nonferrous Metals Society of China*, 22(2012), 275-280.

TRIBOLOGICAL PROPERTIES OF Fe-P POWDER METALLURGY ALLOYS

Shailesh Kumar Chaurasia, Ujjwal Prakash, Vikram Dabhade

Dept. of Metallurgical and Materials Engineering
Indian Institute of Technology Roorkee, Uttarakhand, India

Abstract

With the development of material science and technology, Iron-based powder metallurgy (P/M) alloys are gradually used as wear resistant materials to automobiles and others. Therefore, the great effort has been undertaken to minimize wear cost by design or material changes. In this study, three alloys of different composition of phosphorus were developed by hot powder forging technique. For this purpose, atomized iron powder and ortho-phosphoric acid (H_3PO_4) were used to develop the alloys. The hot forged product was homogenized at 1100°C for 1hour in the muffle furnace. The specimens were annealed by keeping them in muffle furnace at 920°C for 20 minutes and then cooling in the furnace. The annealed specimens were characterized in terms density, microstructure and wear properties. The microstructural characterization includes porosity measurement and grain size measurement. The density of forged and homogenized samples was measured and it was ensured that density increases with increasing the phosphorus content in the iron-phosphorus alloy. It was also observed that the hardness increased linearly with addition of phosphorus. By using a pin-on-disc wear testing machine the effect of phosphorus content on the wear characteristics of iron-phosphorus alloys were studied. The wear tests were carried out at a constant load of 2.5 kg and a sliding speed of 1.57m/s for 30 min. The wear was evaluated by measuring the mass loss of materials during the wear process. It was seen that the loss of material from the surface/wear rate of specimen reduced by increasing the phosphorus content in the iron.

Keywords: Iron, Phosphorous, Tribology, Mechanical Properties, Powder forging.

Introduction

Wear is among the most serious of issues to deal with when contacting surfaces in machine parts are in relative motion, such as in bearings, joints, gears, shafts, hydraulic parts, mining industry machines, components in aeronautical industry, inside scroll compressor, braking components and others. According to some estimates, losses due to friction and wear in the United States are to about 6% of its gross national product and approximately one-third of the world's energy resources ^[1]. Wear is one of the important mechanical properties expected from steels in actual service condition for some of the aerospace and automobile parts. Most of these parts are made by PM technique

and are required to exhibit good wear resistance ^[2]. Tribology is crucial to modern machinery which uses sliding and rolling surfaces. In such a scenario, Fe-P powder metallurgy alloys have gained growing interest in recent years. Among various powder metallurgy techniques, hot powder forging has been recognized as one of the most feasible and cost-effective technique to produce an Iron-phosphorus alloy which will improve the wear and corrosion property. One of the characteristic features of ancient Indian iron is the relatively high concentration of phosphorus (P) in solid solution. The presence of a relatively high amount of P in ancient Indian iron results in several interesting effects.

TRIBOLOGICAL PROPERTIES OF Fe-P POWDER METALLURGY ALLOYS

The superior atmospheric corrosion resistance of ancient Indian iron has been attributed to the high P content [3].

In the present work, the microstructural studies, wear properties of powder metallurgy phosphorus steels are studied. Since phosphorus provides a high solid solution strengthening of the matrix and activates the sintering process, which allows the formation of an appropriate rounded pore morphology [4]. Further, it has been pointed out that sintering in the two phase ferrite-austenite region can bring about a heterogeneous distribution of phosphorus in ferrite, which positively influences the mechanical properties of the alloys [5]. The beneficial effect of alloying with phosphorus can be explained by the following three mechanisms [6]: (a) Liquid phase sintering. (b) Ferrite stabilization: phosphorus stabilizes ferrite and thereby a transformation from austenite to ferrite occurs as phosphorus diffuses into the iron particles during sintering. (c) Solid solution hardening: small amount of phosphorus in iron has a strong solution hardening effect and contributes to the high strength of phosphorus alloyed sintered steels.

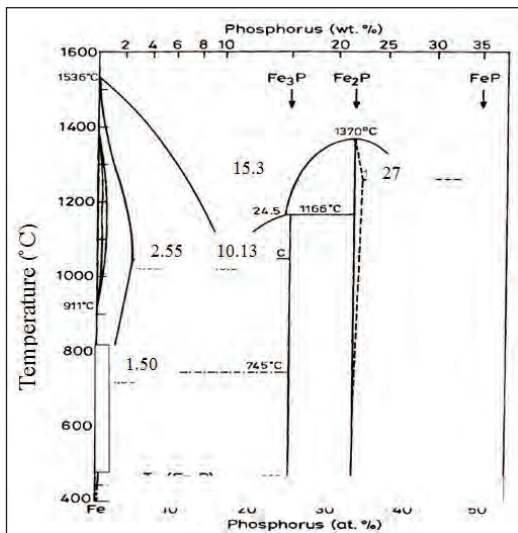


Fig.1 Fe-P binary phase Diagram [8].

Increase of the phosphorus concentration in iron makes allows of forming of the iron phosphides Fe_3P and Fe_2P . This increases its hardness and wear resistance in the process of dry sliding friction [7]. The primary aim of our research has been to study the effect of phosphorus with varying concentration in order to investigate the influence of composition on the wear properties of the developed alloys.

Experimental

The specimens used in this work were produced by powder forging a mixture of Iron powder and master alloy (coated powder) with appropriate amount so that the end product contain 0.00wt%P, 0.35wt%P and 0.65wt%P. The master alloy powder was developed by using water atomized iron powder and orthophosphoric acid which have the following specifications as below:

(a) Specification of atomized iron powder

Atomized iron powder grade No: AHC100.29

Manufactured by : M/S HOGANAS AB,
Sweden

Upper particle size : 0.17mm

Apparent density : 2.59 gm/cc

Flow : 25-28 second per 50 gm.

Compressibility : 6.65-6.68 gm/cc

Hydrogen loss percentage : 0.1-0.2 (i.e. reducible oxygen content)

Carbon content : 0.01-0.02

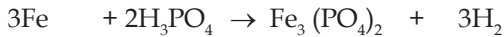
(b) Specification of orthophosphoric acid

Purity : 83-98%

1cc contains : 1.75 gm H_3PO_4

The iron powder, dipped in diluted orthophosphoric acid was left in open air to form iron phosphate and dry. If required, it was also put in the oven at low temperature. The ortho-phosphoric acid would react with the

surfaces of iron particles and form $\text{Fe}_3(\text{PO}_4)_2$ on the iron particle surface by the reaction:



The composite (i.e. coated) powder so produced is decanted and allowed to dry as described. The mechanically mixed powder is encapsulated in mild steel cylindrical can (capsule). The encapsulated powders are thus heated in a tubular furnace at 1050°C for 30 minutes in dry hydrogen atmosphere. The H_2 atmosphere would remove the oxide layer from the surfaces of the powders heated at the high temperatures. The product at the iron particle surface i.e. $\text{Fe}_3(\text{PO}_4)_2$ would be converted to iron-phosphide (Fe_3P), during heating at 1050°C for 30 minutes in H_2 atmosphere, whereas the core of the iron particles remained unaffected. The reaction would be as follows:

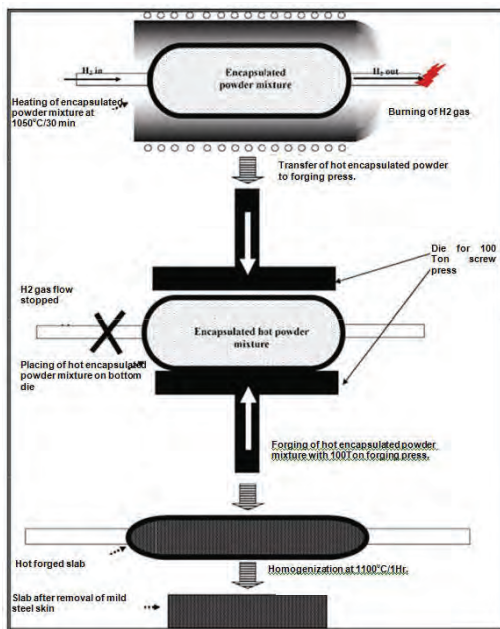


Fig.2 Schematic diagram illustrating the production of slab by hot forging of encapsulated powder mixture.

Capsule is taken out and hot forged in a 100 metric ton friction screw driven forge press. After first blow of the hammer the supply of H_2 gas is closed. Heated capsules are then forged in the press to make slabs using a channel die. Only three strokes are required to form a slab of Fe-P alloy. Fig.2 shows the schematic diagram for the production of Fe-P powder metallurgy alloy. To achieve the higher density or minimum porosity, it is needed to reforge the product at same processing parameter. The steel encapsulation was then removed by machining operations. Samples were prepared from the forged slabs after removal of mild steel skin for density measurement, hardness test, microstructural studies and wear test.

Dry sliding testing

The dry sliding tests were carried out using a pin-on-disc wear testing apparatus. The wear pins of 6mm diameter at one end of specimen of same alloys were machined on lath machine. The wear pins were rubbed against disc EN31 which was supplied by Magnum Engineers. Experiments were carried out under dry sliding conditions at a constant applied load of 2.5kg and constant sliding speed of 1.57m/s during running condition. The wear mass losses of pin specimens were measured after every 30 min sliding. Immediate prior to test, disc was cleaned lightly with alcohol to remove any loose surface debris and foreign particles. Also, the pin specimens were cleaned similarly. The friction force obtained from the continuous measurement of the friction force in the whole sliding process and wear mass loss were used to describe the tribological properties of Fe-P powder metallurgy alloys.

Results and Discussion

In accordance with the results described below, the density increases as the phosphorus content increases. The corresponding porosity was calculated by well known formula

$\epsilon=1-(\rho/\rho_t)$, where ϵ is the fractional porosity, ρ is the density of material and ρ_t is the theoretical density. The changes in porosity correspond to the changes in density.

Table 1: Calculated fraction of porosities of the alloys.

| Materials | Forged density (g/cc) | Percentage porosity in forged slabs |
|-----------|-----------------------|-------------------------------------|
| Fe-0.65P | 7.69 | 2.04 |
| Fe-0.35P | 7.64 | 2.68 |
| Fe | 7.60 | 3.18 |

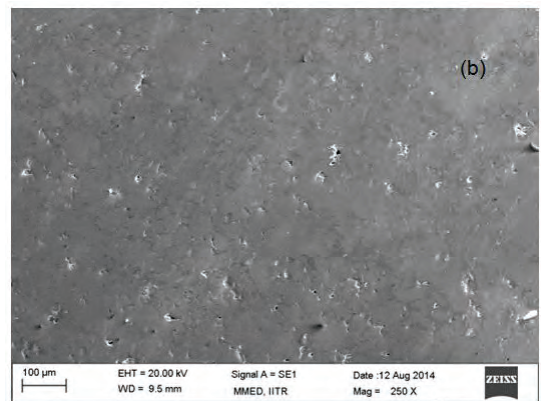
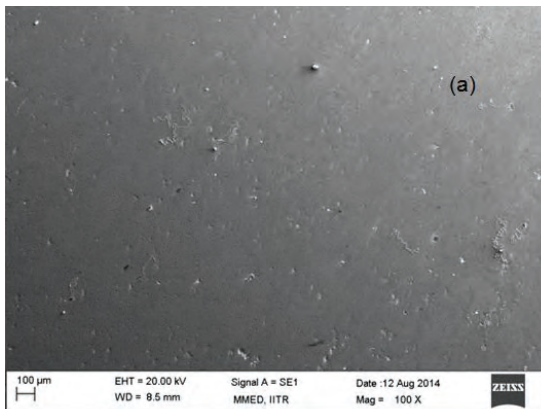


Fig.3. Pore morphology of experimental Fe-P alloys; (a) Fe-0.65wt. %P (b) Fe-0.35wt. %P.

During sintering the phosphorus iron intermetallic compounds melt at a temperature of 1050°C and diffuse into the iron, forming a

solid solution of phosphorus in iron (Fig.1). The liquid phase enhances diffusion rates and assists in the rearrangement of the pores and particle boundaries, thereby further densifying the iron. Additions of phosphorus lead to the formation of a eutectic liquid phase in the initial stages of sintering, beginning at 1050°C and stabilize ferrite. The formation of a liquid phase brings about a quick distribution of phosphorus throughout the iron skeleton by capillary action and grain boundary penetration.

Table 2. Shows the influence of phosphorus addition of iron on tribological properties. It can be seen that the increase of phosphorus addition in iron results in increase in the coefficient of friction and decrease in wear mass loss. These values are better than those reported for alloys prepared using casting route [9]. Also, the coefficient of friction is much higher than those reported for P/M alloys developed by conventional pressing and sintering route [10].

Table 2: Pin on disc wear test of P/M alloys, sliding condition:1.57m/s,0.69MPa.

| Material | Applied load (kg) | Wear track Diameter (mm) | Duration (min) | Friction force (N) | Wear mass loss (Mg/min.) | Volume loss (mm ³) | Specific wear rate($\times 10^{-6}$ mm ³ /Nm) | Coefficient of friction |
|----------|-------------------|--------------------------|----------------|--------------------|--------------------------|--------------------------------|---|-------------------------|
| Fe-0,65P | 2,5 | 100 | 30 | 10,34 | 0,33 | 1,28 | 4,38 | 0,413 |
| Fe-0,35P | 2,5 | 100 | 30 | 7,58 | 0,67 | 2,58 | 12,04 | 0,303 |
| Fe | 2,5 | 100 | 30 | 4,3 | 1,0 | 3,89 | 32,01 | 0,172 |

The addition of 0.65wt% phosphorus resulted in low wear rate at low speeds. The coefficient of friction values shown in Table 2 Indicates that the effect of phosphorus is to increase the coefficient of friction. With the higher phosphorus contents it appears that there was sufficient phosphide to carry the lowest load and the wear rates were reduced.

Fig.4 (a) and (b) show the microstructure morphology of the worn surface zone of the Fe-0.65wt%P and Fe-0.35wt%P pin specimens.

Also, it shows that the iron phosphide content increases closer to the sliding surface. The phosphorus content in the surface layer is much higher than the original phosphorus addition. Microstructure morphology of worn surface zone of Fe-0.65wt%P is clearly shown. In the sliding process, some parts of the phosphorus eutectic are abraded away; the other parts gradually accumulate on the worn surface of the pin and diffuse into the surface layer of pin.

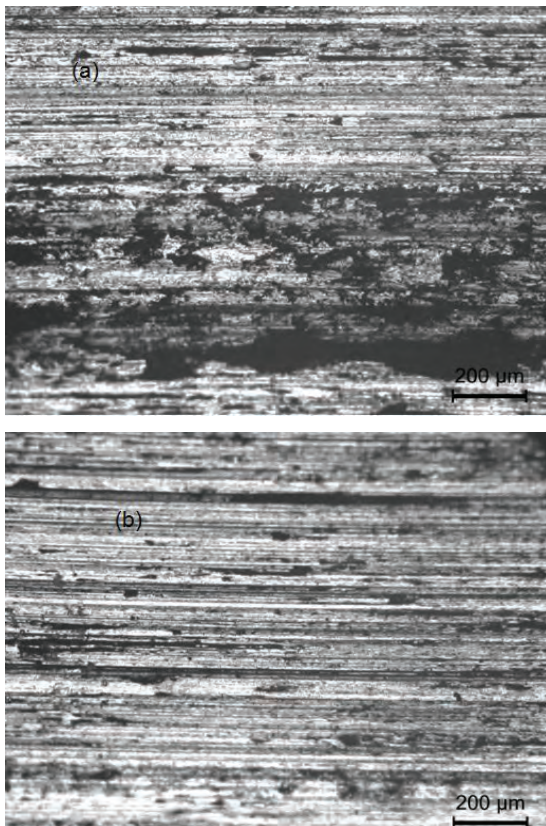


Fig.4. (a) Worn surface of Fe-0.65wt. %P. (b) Worn surface of Fe-0.35wt. %P.

As forged and homogenized microstructure were etched (4% nital) to reveal the grain boundary and shown in figure 5(a) and (b). Figures show the single phase with porosity

distributed along grain boundaries as well as inside the grains for entire range of phosphorous in these alloys. Some of them are irregular size and shape and elongated.

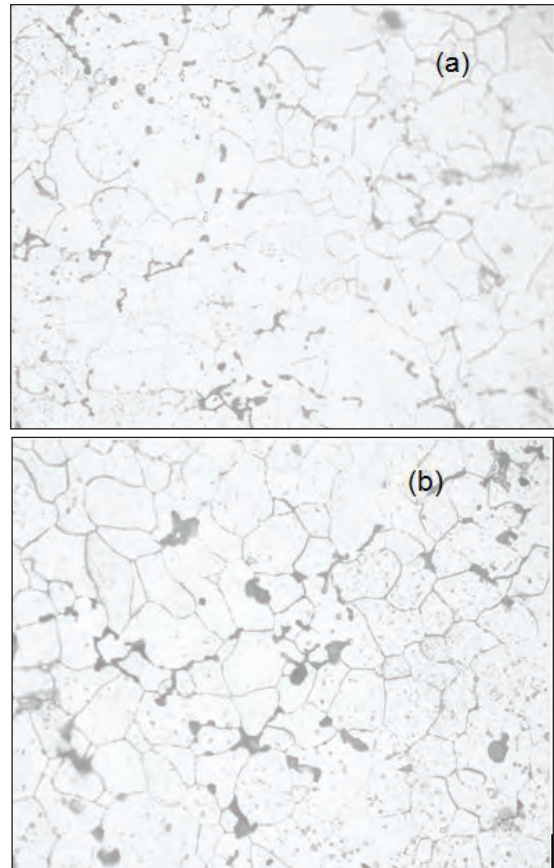


Fig.5 Microstructure (etched) of forged and homogenized samples (a)Fe-0.65wt.%P(b)Fe-0.35wt.%P.

Conclusions

1. The addition of phosphorus in the form of iron phosphate to atomized iron powder results in higher density and enhanced tribological properties.
2. The effect of 0.35wt. % and 0.65wt. %P on the dry sliding wear of P/M Fe-P alloys using a pin-on-disc technique with a speed of 1.57m/s and contact pressure of 0.69MPa has been investigated.

TRIBOLOGICAL PROPERTIES OF Fe-P POWDER METALLURGY ALLOYS

3. The presence of phosphorus reduced the wear rate progressively with increase of phosphorus content in the iron; the lowest wear rate results in the 0.65wt. % P content in the iron.
4. The coefficient of friction has been obtained from 0.172 to 0.413 with a maximum at 0.65wt. % P at 1.57m/s sliding speed and 0.69MPa contact pressure.

References

- [1] B. Bhushan, "Principles and applications of tribology," John Wiley & Sons, Inc., 1999, pp.3-4.
- [2] S.Tekeli et al., "Dry sliding wear behaviour of low carbon dual phase powder metallurgy steels," *Materials and Design*, 28, 2007, pp.1685-1688.
- [3] P. Piccardo, M. G. Ienco, R. Balasubramaniam and P. Dillmann, "Detecting non-uniform phosphorus distribution in ancient Indian iron by colour metallography," *Current Science*, vol. 87, NO. 5, 2004, pp 650-653.
- [4] G.Straffelini, V.Fontanari, A.Molinari, and B.Tesi, "Tensile and fatigue behaviour of phosphorus alloyed sintered steels," *Powder Metallurgy*, vol. 36, NO. 2, 1993, pp 135-141.
- [5] A.Molinari, G.Straffelini, V.Fontanari, and R.Canteri, "sintering and microstructure of phosphorus steels," *powder Metallurgy*, vol. 35, NO. 4, 1992, pp 285-291.
- [6] J. Lynn and P, Rosa, "Ductile Components of Phosphorous-Alloyed P/M Steel," *World Congress on Powder Metallurgy & Particulate Materials*, Montreal, Canada, 2005, pp. 1-9.
- [7] J.Nowacki, "Phosphorus in iron alloys surface engineering," *journal of achievements in Materials and Manufacturing Engineering*, vol.24, 2007, pp 57-67.
- [8] Gautama and R Balasubramaniam, "Alloy design of ductile phosphoric iron Ideas from archaeometallurgy," *Bull. Mater. Sci.*, Vol. 26, No. 5, 2003, pp.483-491.
- [9] Y.Z.Zhang et al., "Metallurgical Investigations of dry sliding surface layers in phosphorus iron/steel friction pairs," *Wear* 252, 2002, pp 269-275.
- [10] Zhengliang Shi. et.al "The Friction And Wear Characteristic Of Fe-based P/M Materials in Scroll Compressor," *International Compressor Engineering Conference School of Mechanical Engineering, purdue*, 2012, pp 1-6.

DEVELOPMENT OF β Ti-xNb ALLOYS THROUGH FIRST-PRINCIPLES DFT ANALYSIS AND P/M ROUTE FOR ORTHOPEDIC IMPLANTS

Rajamallu K¹, Manish K. Niranjana² and Suhash Ranjan Dey¹

¹Indian Institute of Technology Hyderabad, India.

²Ordnance Factory Estate, Yeddumailaram, India.

Abstract

First principle calculations based on density functional framework are employed to study the stability of β phase (bcc) with respect to α phase (hcp) in Ti-x(at.%)Nb alloys (x=6.25, 12.50, 18.75, 25, 31.25, 37.50, 50). In addition the elastic properties of all these combinations are calculated. The calculations showed that β phase in binary Ti-x(at.%)Nb is fully stabilized above 22(at.%) of Nb content. Calculated Young's modulus for Ti-25(at.%)Nb is found to be 80GPa which is lower than the α -Ti alloys and therefore suggesting reduction of 'stress shielding effect'. Thermodynamically stable β phase in binary Ti-x(at.%)Nb is experimentally achieved with P/M prepared 25(at.%) of Nb and is confirmed by X-ray diffraction analysis.

1. Introduction

Titanium based alloys are emerged as most frequently used orthopedic implants in recent years because of their exceptional properties such as superior biocompatible, high strength to weight ratio, excellent corrosion resistance in biological environment [1,2]. Ti alloys are mainly classified into α , $\alpha + \beta$ and β depending upon alloying element content and thermomechanical processing [3]. Ti alloys exhibit comparatively lower elastic modulus (110GPa) than the other metallic biomaterials such as stainless steel (200GPa) and CoCr-based (200-230GPa) alloys [4]. However, this value is quite higher than that of the human bone (20-30GPa). This mismatch in mechanical properties leads to 'stress shielding effect' resulting in bone degradation over the long period of time [5]. The β phase (bcc) Ti alloys are said to possess relatively low modulus which can enhance the mechanical compatibility [6]. In addition, several β stabilizing elements (e.g. Nb, Ta, Sn etc.) are biocompatible (non-toxic) [7]. In this paper, β phase stability are

theoretically predicted in binary Ti-x(at.%) Nb alloy system and further their Young's modulus are calculated. The aim is to develop novel β -titanium alloys suitable for orthopedic implants using first principle calculations and then to fabricate them through P/M route.

2. Calculation Methodology

The first principle calculations based on the density functional theory [8] with the Perdew-Burke-Ernzerhoff (PBE) form of the generalized gradient approximation (GGA) [9] for exchange - correlation functional is employed and the ionic potentials are approximated using projector augmented wave (PAW) [10] pseudopotentials. The bulk calculations are performed with a kinetic energy cutoff of 400 eV using the 6x6x6 and 6x6x4 Monkhorst-Pack k-point meshes for the 2x2x2 cubic bcc and hcp supercells respectively. Supercell of BCC (β phase) and HCP (α phase) contains 16 atoms with space group $Im\bar{3}m$ and $P6_3/mmc$ respectively.

2.1. Calculations of Phase stability

Thermodynamic stability of an alloy system can be expressed in terms of the free energy (F) which is given below:

$$F_f(x,T) = E_{formation}^{hcp/BCC} - T S_{config} \quad (1)$$

Where $E_{formation}$ is the formation energy, S_{config} is the configuration entropy and T is the temperature. The S_{config} can be calculated as

$$S_{config}(x) = K_B \cdot [x \cdot \ln(x) + (1-x) \cdot \ln(1-x)] \quad (2)$$

where x alloy composition in atomic fraction and k_B – Boltzmann constant. The formation energy can be calculated as

$$E_{formation}^{BCC/hcp} = \frac{1}{N_{total}} [E_{supercell}^{BCC/hcp} - N_{Ti} \frac{E_{bulk}^{hcp,Ti}}{16} - N_{Nb} \frac{E_{bulk}^{hcp,Nb}}{16}] \quad (3)$$

where N_{total} is total number of atoms in supercell
 N_{Ti} – Number of titanium atoms in supercell
 N_{Nb} – Number of niobium atoms in supercell
 $E_{supercell}^{BCC/hcp}$ – total energy of the supercell alloy

2.2. Calculation of Young’s modulus

The Young’s modulus (E) of polycrystalline alloy system is calculated from computed elastic constants. The Young’s modulus (E) can be expressed in terms of bulk modulus (B) and shear modulus (G) in Hill’s approximations as:

$$\bar{E} = \frac{9BG}{3B+G}; \quad B = \frac{1}{3}(B_1+B_2); \quad G = \frac{1}{2}(G_1+G_2)$$

$$B_1 = (C_{11}+C_{22}+C_{33}+2C_{12}+2C_{13}+2C_{23})/9; \quad B_2 = [S_{11}+S_{22}+S_{33}+2S_{12}+2S_{13}+2S_{23}]^{-1}$$

$$G_1 = \frac{1}{15}[C_{11}+C_{22}+C_{33}-C_{12}-C_{13}-C_{23}]; \quad G_2 = 15[S_{11}+S_{22}+S_{33}+3S_{12}+3S_{13}+3S_{23}+6(S_{12}+S_{13}+S_{23})]^{-1}$$

The elastic constants are calculated using methodology as described in Ref. [11]

3. Experimental details

Appropriate proportion of elemental Ti (99.5% purity, <-325 mesh) and Nb (99.9% purity, <-325 mesh) powders received from testbourne

ltd. are mixed in agate mortar for 30 mins. Green compacts (diameter: 10 mm, thickness: 2 mm) are prepared using uniaxial press loading of 500 MPa with dwell time 30 sec. In order to avoid the contamination (particularly oxidation), experiments are carried out in high purity Ar gas atmosphere Glove box (Mbraun). These binary Ti-x(at.%)Nb (x=15, 20, 25, 30 and 35) green compacts are quartz sealed in pressure of 3×10^{-6} mbar. These quartz sealed green compacts are sintered at temperature 1273K with 3hrs of holding at heating rate of 10K/min but at different cooling rates: furnace cooled (FC), air cooled (AC), water quenched (WQ). Phase analysis of the fabricated binary Ti-x(at.%)Nb alloys are performed through X-ray diffraction (PAN alytical XPro) using $Cu K_{\alpha}$ X-rays.

4. Results and discussion

The Free energies of bcc β and hexagonal α phases of binary Ti-x(at.%)Nb alloys at T=0 K, 310 K and 1154 are shown in Fig. 1a, 1b, 1c respectively. It is evident that the stability of β phase increases as the Nb content is increased. As can be seen the free energy of bcc β phase becomes lower than that of hexagonal α phase when Nb content becomes higher than 22 at.%. This indicates that bcc β phase becomes more stable than hexagonal α phase for Nb content more than 22 at.%.

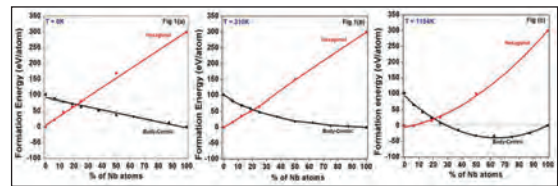


Fig. 1: The free energies of Ti-xNb alloys as function of Nb content at different temperatures (a) T = 0 K (b) T= 310 K (c) T= 1154 K

The calculated Young’s moduli for β phase are shown in Fig. 2. Blue curve indicates the Young’s modulus of stable configuration (configuration having low formation energy)

DEVELOPMENT OF β Ti-xNb ALLOYS THROUGH FIRST-PRINCIPLES DFT ANALYSIS AND P/M ROUTE FOR ORTHOPEDIC IMPLANTS

and red curve represents the average Young's modulus of all possible configurations. The β Ti-xNb alloys exhibited lower Young's modulus than that of pure α phase. These lower Young's modulus compositions in turn reduce the stress shielding effect with bone upon replacement. The electron to atom (e/a) ratio and calculated densities of each composition are also given in Fig. 2.

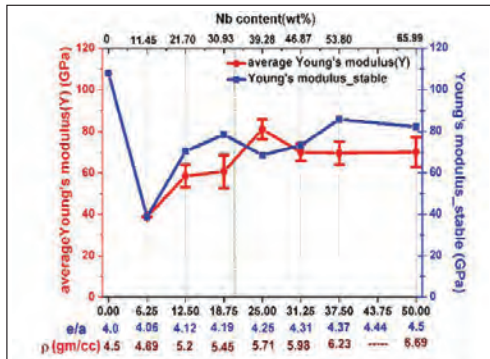


Fig-2: Calculated Young's modulus in binary Ti-xNb

The complete β phase is experimentally achieved in Ti-25(at.%)Nb with FC and Ti-20(at.%)Nb with WQ and are shown in Fig. 3. Thermodynamically stable β phase is stabilized in all compositions of Nb containing more than the 25at.%. It is noted that the compositions less than 25at.% of Nb will have $\alpha+\beta$ phases. However, the complete β phase is stabilized non-thermodynamically in Ti-20(at.%)Nb by means of water quenching.

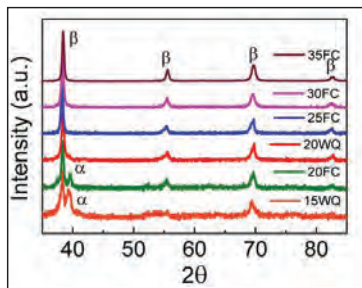


Fig. 3: XRD profiles of binary Ti-x(at.%)Nb compositions

5. Conclusions

Using first principles calculations, low Young's modulus compositions having stable β phase (bcc) of binary Ti-x(at.%)Nb alloy system are obtained. The predicted compositions are experimentally fabricated through conventional P/M route. The calculated values are found to be in good agreement with those obtained from experiments. These fabricated alloys initially designed through first principles calculations are potential candidates for orthopedic implants.

6. Acknowledgment

The authors would like to thank High Performance Computing (HPC) Center, IIT Hyderabad for computational calculations. The authors are grateful to Department of Science and Technology, India for financial assistance availed through Indo-Japan joint DST-JSPS project (DST/INT/JSPS/P-177/2014).

References

- [1] M. Geethaa, A.K. Singh, R. Asokamani, A.K. Gogia, Ti based biomaterials, the ultimate choice for orthopaedic implants – A review, Progress in Materials Science, 2009, 54, 397–425.
- [2] H.J. Rack, J.I. Qazi, Titanium alloys for biomedical applications, Materials Science and Engineering C, 2006, 26, 1269 – 1277.
- [3] Titanium and Titanium Alloys Fundamentals and Applications 2003 WILEY-VCH
- [4] Nag, S., & Banerjee, R. (2012). Fundamentals of Medical Implant Materials, ASM Handbook, Materials for Medical Devices, 23,6-17.
- [5] Niinomi, M., & Nakai, M. (2011). Titanium-Based Biomaterials for Preventing Stress Shielding between Implant Devices and Bone. International Journal of Biomaterials, 836587. doi:10.1155/2011/836587
- [6] Matsumoto, H., Watanabe, S., Masahashi, N., & Hanada, S. (2006). Composition Dependence of Young's Modulus in Ti-V, Ti-Nb, and Ti-V-Sn Alloys. Metallurgical and Materials Transactions A, 37A(November), 3239–3241.

DEVELOPMENT OF β Ti-xNb ALLOYS THROUGH FIRST-PRINCIPLES DFT ANALYSIS AND P/M ROUTE FOR ORTHOPEDIC IMPLANTS

- [7] Biesiekierski, A., Wang, J., Gepreel, M. A., & Wen, C. (2012). A new look at biomedical Ti-based shape memory alloys. *Acta Biomaterialia*, 8(5), 1661-1669. doi:10.1016/j.actbio.2012.01.018
- [8] Kohn W, Sham LJ., (1965). Self-Consistent Equations Including Exchange and Correlation Effects, *Physical Review*; 140:A1133.
- [9] Perdew JP, Burke K, Ernzerhoff M., (1996). Generalized Gradient Approximation Made Simple, *Physical Review Letters*; 77:3865
- [10] P. E. Blöchl, (1994). Projector augmented wave method, *Physical Review B*, 50, 17953-17979
- [11] Manish K. Niranjana, First principles study of structural, electronic and elastic properties of cubic and orthorhombic RhSi, *Intermetallics*, 2012, 26, 150-156.

VIRTUAL MOLDING OF PIM COMPONENTS

Mohamed Ismail Khan, Raman Kumar Jayabalan

MAGMA Engineering Asia Pacific Pte Ltd, Hyderabad, India.

Abstract

The PIM industry faces several challenges: In one hand, the complexity of the parts and the production versatility is increasing. On the other hand PIM processors need reliable and timely answers to design efficient molds. It is widely accepted that simulation is growing in relevance to the industry needs, and it is helping to achieve faster development and feasibility studies. In PIM, the quality issues in the green part must be early identified and avoided. At the same time, robust and stable production process is required. Depending on the available sintering equipment the processor must be able to easily switch from one feedstock to the other, to shorten start-up times for new products with a minimum of scrap; or he has to guarantee an exceptional constant green part quality to run his continuous sintering equipment efficiently. Anyway a complete understanding of the molding process is required to be successful and grow business. This paper throws light on the Virtual Molding approach to ensure green part quality of PIM parts using software tool SIGMASOFT® even before the mold is made. The green part quality is assessed Virtually with SIGMASOFT® and PIM producers easily get reliable information to make sound decisions about the mold configuration: weakness or undesirable aesthetic marks due to a poor positioning of welding lines, possible particle segregation associated with high shear rates or possible voids are visualized in the computer, as they would appear in the molded part. The relevance of these issues increases proportionally with the part complexity, as previous experience may not be enough to ensure a smooth and profitable production.

1. Introduction

During the last fifteen years Powder Injection Molding (PIM) has become a reliable production technology for complex shaped metallic and ceramic parts. Today the PIM industry is on the growth track world wide. Miniaturization is one of the key demands in industries like electronic, medical or automotive, but when part dimensions decline drastically, the geometrical complexity increases proportionally and functional integration comes as an additional demand. The manufacturing of such complex-shaped micro-applications becomes challenging and hence a perfect target for Powder Injection Molding (PIM) technology.

The use of design simulation tools has proved valuable to identify inefficiencies and technical issues as soon as possible in

the product development process to shorten the time into the market. Beyond this, the unique process-oriented simulation approach of SIGMASOFT® allows a complete thermal simulation of the process, a critical factor to improve the accuracy of the simulation, due to the very temperature-sensitive nature of Metal Injection Molding (MIM) feedstocks.

Being the first step in the process-chain of MIM applications, injection molding influences decisively the part quality: an error arising at this stage cannot be repaired later on. Furthermore, it is extremely difficult to exert a quality control process over the green parts, in order to allow only those which meet predefined quality standards to continue to the next process stages.

With aid of the process-oriented simulation approach of SIGMASOFT®, the quality

of the green parts can be analyzed, and dependences between part, mold and process can be thoroughly understood. The green parts and the scrap offer at least the same optimization potential as the cycle time of each one of the process steps. The simulation with SIGMASOFT® can help to identify the optimization potential at each stage during the injection molding process, and therefore to reduce cycle times and to improve part quality.

The process-oriented approach in the simulation offers the possibility to consider not only the part, but also the complete mold with all its components, such as cooling systems or inserts. Furthermore, all the process steps, such as preheating of the mold, filling, post-pressure and external cooling can be analyzed with SIGMASOFT® over several cycles. This “Virtual Production” enables to use the simulation effectively during the development of new molds, and to recognize early possible disadvantages of a given mold concept. In this way, time and costs can be saved through the optimization of each one of the process steps in the whole MIM process chain

Rheology: MIMs are no thermoplastics

Rheology is always the key factor determining article quality and processability. Measurements with a capillary rheometer at different shear rates, and additional measurements with a controlled shear stress rheometer revealed that in comparison to conventional thermoplastics, for MIM materials there is no Newtonian plateau but actually an increase of the viscosity at lower share rates. This effect cannot be predicted by the rheological models used as a standard in injection molding simulation software.

Due to the increase in viscosity at low shear rates, the MIM feedstock behaves in this low shear rate range more like a solid material

than a polymer melt. Often people think that these low shear rates never occur in actual moldings. However, if one thinks about the shear rate distribution across a flow channel, it becomes obvious that very low shear rates occur everywhere in the runner, gate and cavity. For typical thermoplastic melts this shear rate range does not influence the cavity filling and the corresponding simulation predictions significantly, but for MIM it becomes a dominating phenomenon. The flow profile differences between conventional thermoplastics and MIM can be seen in Fig.1. As a result, compared to thermoplastics, a flattened velocity profile is produced for MIM applications, well known as plug flow. The whole shear load is concentrated at a very small layer close to the mold wall and the feedstock is “slipping” at this low viscosity layer, causing the typical jetting phenomena.

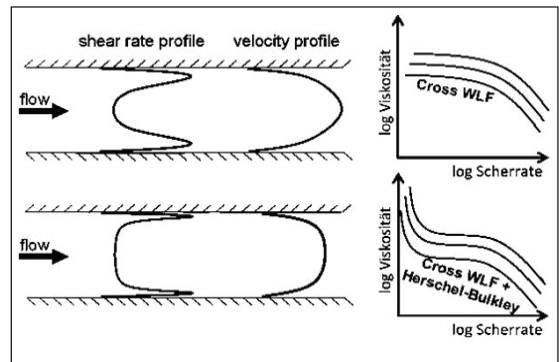


Fig.1 Flow profile differences predicted with a Cross-WLF model (above) and a Cross-WLF with Herschel-Bulkley extension model (below).

Virtual Molding of PIM components

i. Mold Performance :

Virtual Molding Technology reproduces exactly the temperature conditions in the mold after several molding cycles. As displayed in Fig.2 for example the temperature conditions

in the mold can be evaluated at any time during the process. The quality of green parts can be evaluated and the dependencies between part, mold and process become transparent.

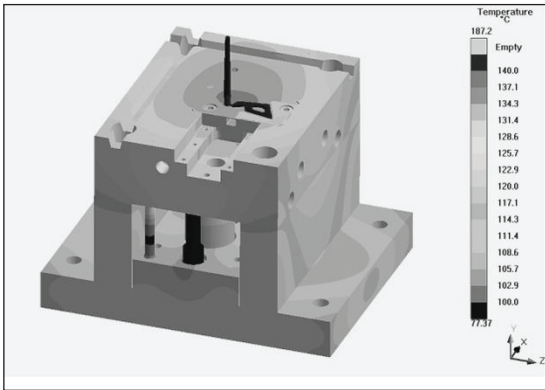


Fig.2 Temperature plot of a Mold after completing multiple injection molding cycles.

Also the complex interactions between feedstock and mold components are reproduced at every process step over several cycles. An accurate thermal calculation delivers critical information impacting cycle time and part quality

As the temperature distribution in the mold after several production cycles is drastically influenced by the conductivity of the base mold material, the right alloy can eliminate mold hotspots and shorten cycle time. So intelligent decisions can also be made to select Hot-work tool steel over conventional tool steel to eliminate hot spots and reduces cycle time

ii. Rheology :

The prediction of the rheological behavior has proved to significantly increase the reliability of simulation for PIM and CIM applications. At low shear rates it has been commonly observed that instead of the typical plateau found for thermoplastic applications an increase of the viscosity is detected. As shown

in Fig.3 a newly-integrated model which considers this increase improves the flow prediction, and particularly the jetting effect. Though extensive jetting phenomena can still appear due to the challenging CIM rheology, the general presence of jetting is however reliably predicted by the simulation, therefore allowing critical driving forces to be studied and understood early in the mold design phase. Jetting can create part defects, such as pores and visual marks, and should be avoided by principle. If simulation allows understanding the driving forces behind kinetic flow effects such as jetting, an enormous control is gained, with countable benefits.



Fig.3 Jetting in a CIM application Vs. VIRTUAL MOLDING Result

iii. Tracer Particle Applications for defect detection :

With “Tracer” technology the appearance of weld lines can be reproduced during the filling stage. The location of this weld lines can be described precisely and also an indication is given of how critical they are. The formation of the weld lines during the filling stage and the way they flow as the packing pressure is applied are predicted accurately in a 3D approach.

Weld lines occur as a consequence of the collision of two (or more) flow fronts in the cavity of a mold. This disruption in the homogeneity of the injection molded part causes optical defects, which compromise the surface quality, but also produces a weakening from the mechanical point of view and, under certain circumstances, weld lines can even act

as stress concentrators. Therefore, there is a loss in the mechanical properties in the regions where weld lines appear.

Tracer particles also show how changes in the flow channel geometry generate vortices trapping the two binder rich layers successfully in the ribs before flowing into other areas.

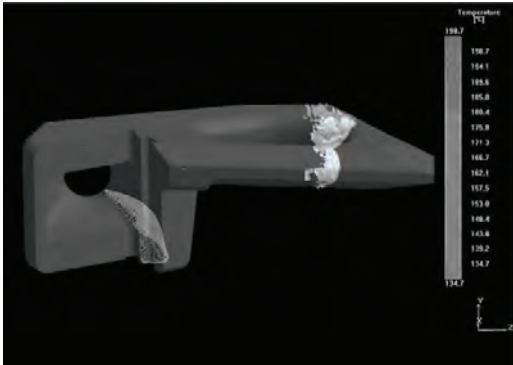


Fig.4 The tracer technology in SIGMASOFT® allows visualizing the fully 3D profile of weld lines over the part thickness.

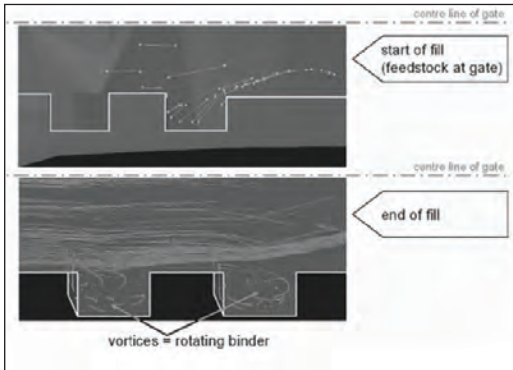


Fig.5 Trapped binder rich layers.

iv. Packing Efficiency :

The gate can freeze before the end of packing phase in an injection molding cycle thereby stopping additional pressure from reaching the cavity area. This is showcased virtually to optimize the process and reduce cycle time. Fig.6 shows the gate freeze but still molten material inside the cavity.

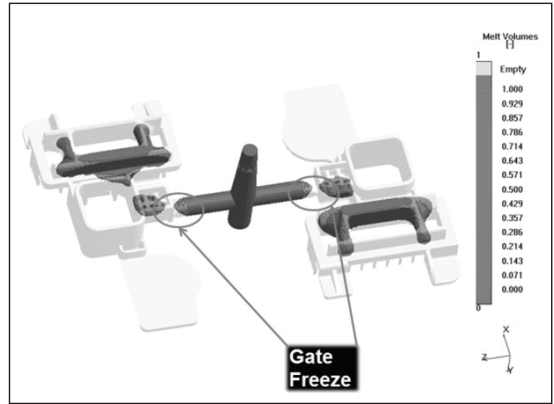


Fig.6 Gate freeze and disconnected from molten material in the cavity.

v. Shear Rate :

As explained above MIM feedstocks are not thermoplastics, they behave in this low shear rate range more like a solid material than a polymer melt. So it is critical to identify areas of high shear heating. Virtual molding technique shows clear regions of high shear rates. This is shown in Fig.7.



Fig.7 High shear rate gradients forcing powder particles to leave areas of high gradients as segregation in MIM. Accurate shear rate results are important to determine particle concentration in MIM to produce quality parts.

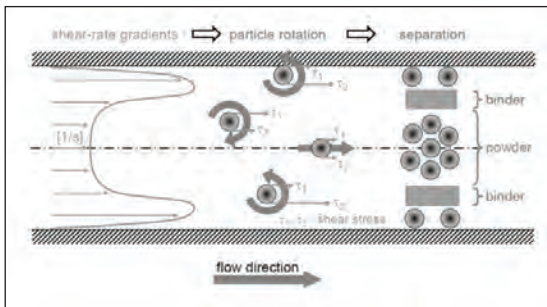


Fig.8 An increase in the shear rate can produce particle separation from the binder system. Simulation can identify the high shear rate regions susceptible to particle segregation .

vi. Air Entrapments:

The behavior of entrapped air in the cavity is often intransparent as shown in Fig. 9. Unsuspected air entrapments appear and have negative influence on the part quality. Their real position, shape and consequences usually become visible in the finished part only. With the process oriented simulation of SIGMASOFT® they can be reliably predicted from the beginning of the part and mold development. The once more enhanced venting option allows to compare different venting solutions and to evaluate their efficiency based on physical factors for various MIM/CIM applications.

Possible solutions to avoid defects can be compared in short time before changes are made to the process or mold. The influence of venting on the filling behavior is immediately visible in the simulation and in the result interpretation possible burn marks or other defects can be clearly identified.

vii. Prediction of Particle Concentration :

Feedstock flow its dynamic in the mold as shown in Fig. 10. When flowing through narrow cross sections in the mold, the feedstock may undergo high shear rates, which force particle segregation from the binder, as in Fig.7 and 9. This undesired effect can lead to pores

or differences in local density of the sintered part, which in extreme cases may lead to stress concentration and part failure. By using tracer particles the defects created by segregation can already be identified.

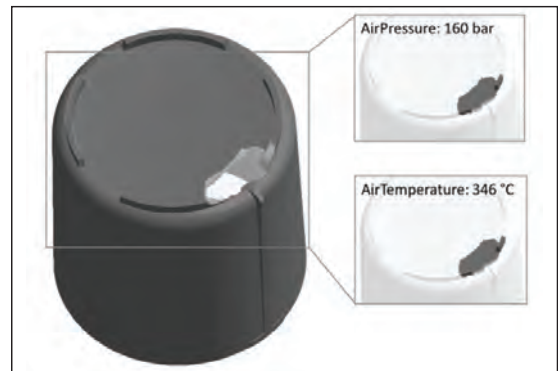


Fig.9 Air Entrapment results threw virtual molding.

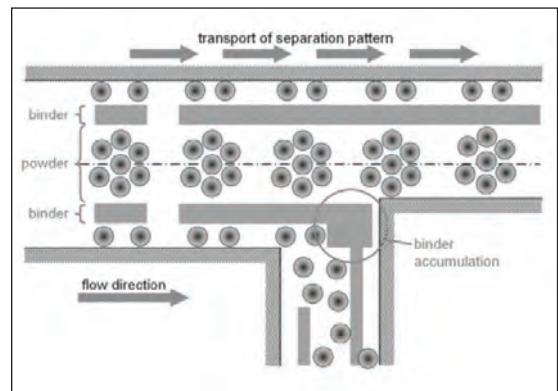


Fig.10 Feedstock flow is dynamic

Summary

PIM has become a key production technology for the manufacturing of metal and ceramic micro parts. The molding stage determines part quality, as defects induced here cannot be healed later on. Furthermore, in micro PIM the costly mold manufacturing methods make iteration on steel unviable. These arguments make simulation an important and profitable tool, to be applied early in the design stage.

VIRTUAL MOLDING technique using SIGMASOFT® has thus developed to serve the interests of PIM industry, involving several features and material models which dramatically improve reliability and accuracy of the flow and thermal behavior predicted. Even in micro-molding applications SIGMASOFT® simulation has proved to be a useful tool, up to the point of delivering first-shot success.

Virtual Molding has to be understood as a valuable tool and has to be well-established into the part and mold design process. Only then will the expected success potential for CIM and PIM be actually achieved.

References

- [1] M. Thornagel: "Injection moulding simulation: New developments offer rewards for the PIM industry". PIM International, Vol.6 No.1 March 2012, pages 65-68.
- [2] M. Thornagel: "MIM-simulation: A virtual study on phase separation". EuroPM2009, Copenhagen, October 2009
- [3] J. Heneka, T. Müller, M. Thornagel: "Micro-Molded CIM-Components: Simulation based Mold- and Process Development". EuroPM2013, Gothenburg, Sweden, September 2013
- [4] M. Thornagel: ritzgusssimulationan Werkzeugkonzepten für Nano-Kompositen. BMBF Projekt PROMI", final project presentation. Fakuma 2011, Friedrichshafen, October 2011.
- [5] SIGMASOFT internal documents.

CHARGE CARRIER REVERSAL IN LEAD MODIFIED CHALCOGENIDE GLASSES

Akhyaya K. Pattanaik

Veer Surendra Sai University of Technology, Burla, Sambalpur, India

Abstract

A systematic study of the electrical, thermal and optical properties of bulk and thin films of Pb modified chalcogenide glasses such as (a) $Pb_xGe_{42-x}Se_{58}$ ($3 \leq x \leq 15$) (series I); $x_T \approx 9$, (b) $Pb_{20}Ge_xSe_{80-x}$ ($17 \leq x \leq 24$) (series II); $x_T \approx 21$, (c) $Pb_xGe_{42-x}Se_{48}Te_{10}$ ($3 \leq x \leq 15$) (series I); $x_T \approx 9$, (d) $Pb_{20}Ge_xSe_{70-x}Te_{10}$ ($17 \leq x \leq 24$) (series II); $x_T \approx 21$ and (e) $Pb_xIn_{25-x}Se_{75}$ ($1 \leq x \leq 7$); $x_T \approx 3$, where x_T represents the composition at which p - to n - type transition is expected to occur are reported. Bulk glass samples were prepared from high purity elements by the melt quenching technique, whereas thin films of the corresponding glasses were prepared by the thermal evaporation of the respective bulk glasses. Glass transition and crystallisation temperatures, heat capacity jump at the glass transition and the activation energy for glass transition were determined using a Differential scanning calorimeter (DSC). The majority charge carrier type in each glass composition (bulk and thin film) was determined by thermoelectric power (TEP) measurements. Electrical conductivity of the glasses in bulk and film form was measured from room temperature to 400 K using the four-probe technique. Optical band gap of glasses was determined from optical absorption measurements made with a dual beam ultraviolet-visible-near infrared spectrophotometer. Microhardness of bulk glasses was measured using a Vickers microhardness tester. All the experimental results were analysed based on the existing theoretical formalism.

Key Words: Chalcogenide glasses, Meltquenching technique, Glass transition, Thermoelectric power

Introduction

The pioneering work by Tohge et al. demonstrated that majority charge carrier reversal (MCCR) could be realized in bulk (p -type) amorphous Germanium Selenide with the addition of sufficient amount of Bi [1-2] or Pb [3]. Although a lot of efforts have been made to understand the majority charge carrier reversal mechanism in Bi-modified chalcogenide glasses, a less effort has been made to understand the mechanism behind the carrier type reversal phenomenon in Pb-modified chalcogenide glasses. To exploit the applications of these glasses as a device, it is necessary to study the various physical properties, viz. optical, electrical and thermal in thin film form. The above mentioned reasons pave the way to study the Pb modified

chalcogenide glasses, viz., Pb-Ge-Se, Pb-Ge-Se-Te and Pb-In-Se glasses in bulk as well as thin film form.

Experimental

Bulk glasses of Pb modified chalcogenide glasses were prepared by melt quenching technique, whereas, thin films were by thermal evaporation of the respective bulk glasses as explained elsewhere [4]. The amorphous nature of the as prepared bulk samples and as deposited thin film samples were confirmed by the absence of any sharp peaks in the x-ray diffraction pattern. TEP measurement on both kinds of samples was carried out using an indigenously fabricated set-up [5]. Analysis of the composition of bulk as well as thin films was done using a Scanning electron

microscope (Jeol 5800) equipped with EDAX facility. The thickness of the thin films was measured using a commercial ellipsometer (Gaertner LXUV910). Optical absorbance of the films in the wavelength range of 300-900 nm was recorded in a dual-beam ultraviolet visible and near infrared spectrophotometer (Shimadzu 3101 UVPC) with a blank substrate plate as reference. Optical band gap was calculated from the plots of $(\alpha h\nu)^{1/2}$ versus $h\nu$. d.c. electrical resistivity of the bulk and thin films was measured by the four probe method under a low pressure of 10^{-4} Torr. Microhardness of the bulk Pb-Ge-Se(-Te) glasses was measured by the commercial microhardness tester (Buehler Micromet 2100).

Results and Discussion

Pb-Ge-Se glasses: DSC studies shows that T_g value exhibited a minimum value at 9 at. wt.% Pb in series I, whereas that has a maximum value at 21 at. wt.% Ge in series II bulk glasses. The first crystallization temperature (T_c) follows the same trend as the T_g for both the series of glasses. Degree of fragility (m) and excess heat capacity (ΔC_p) of both the series of glasses show minimum values at the composition at which the carrier reversal was observed indicating that these compositions are kinematically stronger and thermodynamically stronger than the rest of the compositions. From the TEP measurements, it was shown that bulk $Pb_{03}Ge_{39}Se_{58}$, $Pb_{06}Ge_{36}Se_{58}$, $Pb_{20}Ge_{17}Se_{63}$, $Pb_{20}Ge_{19}Se_{61}$ glasses were p -type semiconductor and the rest of the glasses were n -type semiconductor. However in thin films, the $Pb_{09}Ge_{33}Se_{58}$ composition showed p -type conductivity. The carrier type reversal in these glasses was explained on the basis of the change in the concentration of charged defect states with the variation in composition^[4]. The optical band gap energy is a minimum for the composition with 9 at. wt. % Pb for

series I and a maximum at the composition with 21 at. wt.% Ge for series II glasses. From d. c. electrical conductivity measurements, the electronic conduction in the temperature range 325 K to 425 K could be attributed to band transport mechanism. Microhardness of series I and series II glass show similar trends as depicted by T_g (and E_{opt}), since this property also depends on the average bond energy of the glass.

Pb-Ge-Se-Te glasses: DSC studies show that T_g does not vary much after 9 at. wt. % Pb for $Pb_xGe_{42-x}Se_{48}Te_{10}$ glasses and reaches a maximum value at 21 at. wt. % Ge for $Pb_{20}Ge_xSe_{70-x}Te_{10}$ glasses [6]. The degree of fragility (m) and the excess heat capacity (ΔC_p) showed the KS-TS behaviour at the composition where majority charge carrier reversal occurs. TEP measurement on these glasses revealed that bulk glasses with $x \geq 9$ at. wt. % Pb and $x \geq 21$ at. wt. % Ge in series I and series II glasses respectively showed n -type conduction. This carrier type reversal phenomenon is explained on the basis of change in the charge carrier concentration of charged defect states with the addition of Pb. Optical band gap energy and microhardness showed the same behaviour as that of glass transition temperature because they are all bond sensitive properties. d.c. electrical conductivity studies showed that resistivity (ρ) and activation energy (E_a) for electrical conduction decreases in $Pb_xGe_{42-x}Se_{48}Te_{10}$ glass, with a slope change at the composition at which the carrier reversal was observed. In the case of $Pb_{20}Ge_xSe_{70-x}Te_{10}$ glasses (bulk and thin films), ρ and E_a showed a maximum value at 21 at. wt. % Ge. Thin film had higher electrical conductivity value than the bulk samples. An interesting outcome of the studies on Pb-Ge-Se-Te glasses is the influence of the substitution of Se with Te. Te substitution decreases the average bond energy

of the glasses, which in turn result in lower T_g , E_{opt} and VHN values. m and ΔC_p are also lower for Pb-Ge-Se-Te glasses, which suggests that Te substitution results in kinetically and thermodynamically strong glasses.

Pb-In-Se glasses: From the sample preparation procedure it was established that bulk samples could not be prepared in completely amorphous form. Only an alloy of Pb-In-Se containing Se crystallites embedded in an amorphous matrix could be prepared. Thin films of these materials could not be prepared in completely amorphous form. However, the nucleation of the crystalline phase could be reduced by depositing the films at lower temperature. The particle size of crystallites in Pb-In-Se ranged from 75 Å to 160 Å. Particle size decreased when the films were deposited at lower temperature. However, T_g and TEP data on melt quenched bulk Pb-In-Se showed a good correspondence with the data reported in literature. p -type to n -type transition could be observed in this partially crystallized bulk samples. Thermoelectric power measurements on thin film samples with nanometer crystallites showed that the carrier reversal occurs at 3 at. wt.% Pb. The charge carrier type reversal phenomenon is attributed due to the presence of charged defect states disturbing the equilibrium of the VAPs [7]. But the presents of nanaometer size crystallites shows that an alternate model for the carrier reversal, based on percolation of sub-microscopic clusters could be ruled out. Electrical resistivity and optical band gap decreases as the Pb content was increased. This behaviour is attributed to the lowering of average bond energy on the addition of Pb in In-Se.

Conclusion

Bulk and thin films of Pb modified chalcogenide glasses have been prepared. Glass transition temperature (T_g), crystallization temperature

(T_c), and excess heat capacity at glass transition (ΔC_p) were determined using a DSC. Electrical resistivity (ρ) and optical band gap (E_{opt}) are also determined from electrical and optical measurements. Non-electronic properties such as T_g , ΔC_p , micro hardness, E_{opt} in both the bulk as well as thin films of the glass systems showed an anomalous behaviour at and around the composition where p - to n -type transition occurred. All the above properties could be described on the basis of existing models, which are related to chemical bonding and network topology of the glass. Hence not only electronic properties but also change in glassy networks are also responsible for p - to n -type conduction in these glasses.

Reference

- [1] N. Tohge, Y. Yamamoto, T. Minami, M. Tanaka, Appl. Phys. Lett. 346 (1979) 640
- [2] N. Tohge, T. Minami, Y. Yamamoto, M. Tanaka, J. Non-Cryst. Solids 37 (1980) 23
- [3] N. Tohge, H. Matsuo, T. Minami, J. Non-Cryst. Solids 95-96 (1987) 809
- [4] A. K. Pattanaik, A. Srinivasan, Proc Of VIth ATPC 2001, 1 (2001) 188
- [5] A. K. Pattanaik, C. Borgohain, A. Srinivasan, Ind. J. Phys., 74A (2000) 307
- [6] A. K. Pattanaik, A. Srinivasan, J. Mater. Sc. , 38 (2003) 2511
- [7] A. K. Pattanaik, A. Srinivasan, J. Optoelec. & Adv. Mat.,5 (2003)1161

FABRICATION OF CERAMIC PARTS BY CERAMIC MICROSTEREOLITHOGRAPHY BY DIFFERENT LAYER RECOATING TECHNIQUES

Chandrashekar Adake, Prasanna Gandhi and Parag Bhargava

IIT Bombay, Mumbai, India.

Abstract

Ceramic Microstereolithography (CMSL) is one of the solid free form fabrication (SFF) techniques which involve fabrication of 3 dimensional ceramic objects by means of space resolved photopolymerization of ceramic suspension. The spatial resolution and capability to fabricate high aspect ratio structures makes it suitable technique for the fabrication of Micro Electro Mechanical Devices (MEMS) and biomedical devices. Silicon based micromachining technique is expensive method of fabricating MEMS devices but has limitation of fabricating high aspect ratio structures. Virtually a part of any shape and of any ceramic material can be fabricated as long as the powder is dispersible in photo curable resin. Ceramic suspensions formulated in resins are highly viscous due to high solid loading and hence successful layer recoating becomes challenge. Here we have reported different layer recoating methods namely constrained surface technique and free surface techniques. Millimeter size ceramic parts are fabricated using these techniques and relative merits and limitations are reported.

Keywords: Ceramic Microstereolithography, Layer recoating, constrained surface, free surface technique

1. Introduction

Recently fabrication methods of Micro Electro Mechanical systems (MEMS) devices have attracted attention of many research groups worldwide. MEMS devices are used in applications such as temperature sensing, force sensing, actuation mechanisms and in some biomedical devices [1]. MEMS devices used for such applications should possess excellent material properties to serve their intended purpose. Traditional materials have many limitations and may not serve their function in MEMS devices. Silicon based micromachining process is one of the technologies used for fabrication of these MEMS devices. However there are certain limitations associated with traditional silicon based micromachining process. Fabrication of components with this method is quite expensive, furthermore it has limitation of fabrication of high

aspect ratio structures [2]. Recently Ceramic microstereolithography (CMSL) has been proved an alternative method of fabrication of MEMS devices. Ability to process wide range of materials, ability to fabricate high aspect ratio structures makes CMSL almost versatile technique for fabrication of MEMS devices.

Fabrication of ceramic parts in CMSL starts with photo polymerizing the suspension. Layer of different shape and size are cured by CAD controlled laser beam. Then these layers are piled one over the other and fused with each other to create a green ceramic part. This green body is sintered to remove monomer. Photopolymerizable ceramic suspension consists of UV curable monomer, photoinitiator, ceramic particles and a dispersant. Selection of monomer and photoinitiator depends upon their UV absorption characteristics. Alumina is most common ceramic material used in

FABRICATION OF CERAMIC PARTS BY CERAMIC MICROSTEREOLITHOGRAPHY BY DIFFERENT LAYER RECOATING TECHNIQUES

these suspensions. Usually ceramic particles with sub-micron size will be selected for formulating suspension as the dimension that are expected in MEMS devices are in terms of microns [3]. The solid loading in such type of suspensions should be around 40 vol. % in order to obtain defect free sintered parts [4]. With such high solid loading suspensions becomes highly viscous and become a challenge to coat a uniform layer one over the other. It has been reported that suspension should have viscosity less than 5 Pas in order to coat fresh layer over the previous one [5]. However this limitation can be overcome by synchronizing speed of layer recoating blade with viscosity of suspension [3].

We have used two different methods of layer recoating namely constrained surface and free surface MSL technique. Both techniques have certain limitation and advantages. We have fabricated millimeter size ceramic structures using with both these technique and evaluated individual performances

2. Experimental details

2.1 Materials and Methods

Following table shows materials and their properties used in this study. 1, 6 hexanediol diacrylate (HDDA) is a low viscous bifunctional UV curable monomer; Phosphate ester was used as a dispersant to improve solid loading. The method of formulating suspension is as follows.

Table 1. Properties of materials used for formulating ceramic suspensions

| Monomers/photoinitiator/dispersant | Molecular structure | Refractive index | Density (g/ml) | Molecular weight |
|--|---|------------------|----------------|------------------|
| 1, 6 Hexanediol diacrylate (Sigma Aldrich) |  | 1.45 | 1.01 | 226.27 |
| Benzoin Ethyl ether (BEE) (Sigma Aldrich) |  | 1.57 | 1.10 | 240.30 |
| Phosphate ester | Isodecyl alcohol polyethoxylate | - | 1.02 | - |

Sub- micron alumina (Almatis CT300SG, d_{50} = 0.5 micron, surface area 8.2 m²/g as measured from BET) was chosen as the starting ceramic

raw material. Initially, alumina powder was dried under vacuum at 120°C for about 8 hours to remove moisture adsorbed on particle surface. HDDA was mixed with 2.5 wt. % of phosphate ester (with respect to weight of powder) and 4 wt. % Benzoin Ethyl Ether (BEE, with respect to weight of monomer). The dried powder was added incrementally till the solid volume fraction reaches 0.40. The suspension was homogenized in a pot mill using ceria stabilized zirconia balls which were added in suspension in the ratio of 1:1 with respect to weight of powder. The suspension thus prepared was easily pourable and viscosity was well below 5P as measured by a rheometer (Physica 301) with parallel plate geometry.

2.2 Experimental setup

CMSL is equipped with solid state laser (Cobolt, Zouk) having maximum power of 20mW at 355nm. Laser spot size suspension surface is about 6microns which was calculated based on lens size, focal length of lens and wavelength of laser beam. CMSL is scanning based Microstereolithography apparatus with maximum scanning speed of 1.2 mm/sec. Fig. 1 shows actual photograph of CMSL setup. For the fabrication of ceramic part scanning speed of 1mm/sec and 2mW power (at laser source) was used. Fig. 2 shows schematic of two different methods of layer recoating.

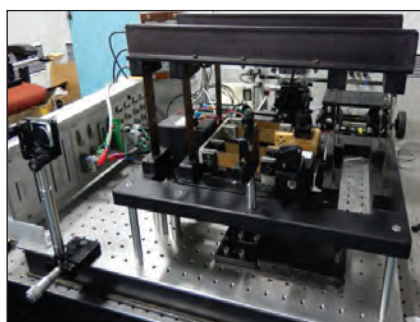


Fig. 1 CMSL set up

FABRICATION OF CERAMIC PARTS BY CERAMIC MICROSTEREOLITHOGRAPHY BY DIFFERENT LAYER RECOATING TECHNIQUES

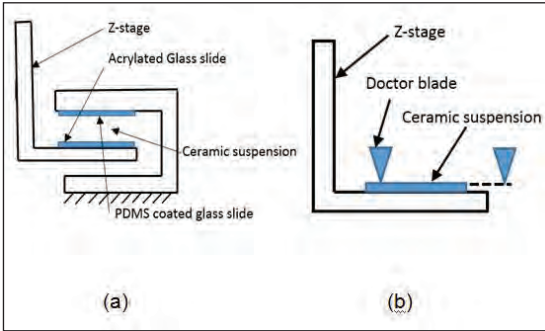


Fig. 2 (a) Constrained surface (b) Free surface MSL (doctor blade technique)

3. Results and discussion

3.1 Cure depth at different energy doses

When ceramic suspension is exposed to UV radiation the light gets scattered and absorbed partially. Due to this phenomenon there is a limited depth at which the UV radiation can reach into the resin. This depth is known as curing depth (C_d) and it is expressed as follows [5]

$$C_d = D_p \ln \frac{E_{max}}{E_c} \dots \dots \dots (1)$$

Where D_p is the depth of penetration of UV radiation and the ' E_{max} ' is the maximum energy available at the resin surface and ' E_c ' is the minimum energy required to polymerize the monomer that is the energy below which there is no polymerization. When ceramic particles are included in monomer then equation is modified to [5]

$$C_d = \frac{d}{Q \phi} \ln \frac{E_{max}}{E_c} \dots \dots \dots (2)$$

Where ' d ' is mean particle size, ' Q ' is scattering efficiency term, ' ϕ ' is solid volume fraction. In case of ceramic filled resin scattering by particle is prominent phenomenon, Most of the photons of UV light get scattered and rest of photons reach towards suspension till their

energy becomes equal to critical energy [6]. Table 2 shows cure depth obtained at different energy doses. Energy at ceramic suspension surface is calculates using following equation

$$E_{max} = \sqrt{\frac{2 P}{\pi w_o v_s}} \dots \dots \dots (3)$$

Where, ' P ' is the laser power of laser beam, ' w_o ' is the beam diameter and v_s is the scanning speed.

Table 2. Cure depth of suspension at different energy doses.

| UV Energy on suspension (mJ/cm ²) | Cure depth (microns) |
|---|----------------------|
| 441.19 | 39.59 |
| 592.18 | 47.86 |
| 710.71 | 52.02 |
| 918.11 | 58.26 |
| 1021.63 | 62.25 |

3.2 Fabrication of ceramic parts by different layer recoating techniques

A CAD file was created in Pro/E having rectangular counter of size 2mm X 2mm and converted to STL format. The thickness of model was kept 0.48 mm. Each layer thickness was about 40 microns so that total number of layers would be 12. Fig.3 (a) shows CAD model used for fabricating ceramic part. Before initiating actual fabrication of ceramic parts it is necessary check cure depth of suspension at different energy doses. Obviously cure depth should be more than 40 microns in order fuse two layers. In order to improve adhesion between two layers source power was kept at 2mW and scanning speed was maintained at 1mm/sec. As discussed two different layer re-coating methods were used schematically which are shown in Fig. 2. It was found that after 2-3 layer of fabrication the layer get attached to constrained surface itself. This was reported by many authors while fabricating polymeric objects. This limitation still exists in case of

FABRICATION OF CERAMIC PARTS BY CERAMIC MICROSTEREOLITHOGRAPHY BY DIFFERENT LAYER RECOATING TECHNIQUES

ceramic parts fabrication too. However it is to be noted here that a uniform layer thickness can be maintained with this technique. Hence it can be proved that this technique was useful for the ceramic parts having 2-3 layers and that cannot be used for fabricating high aspect ratio structures. Fig.3 (b) shows the ceramic layers attached to constrained surface.

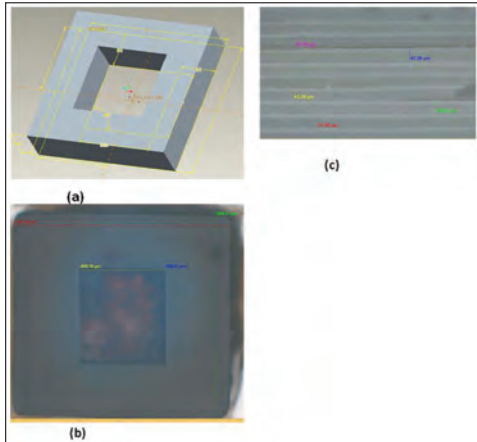


Fig. 3(a) CAD model showing the dimensions
(b) Part attached to constrained surface
(c) Front view of part fabricated using free surface technique (doctor blade technique)

On the other hand with free surface technique (doctor blade) we were able to fabricate complete structure that is 12 layers of 40 microns each. This method utilizes shear thinning behavior of ceramic suspensions. The speed of the blade can be adjusted to viscosity of suspension^[7]. It was also found that there was good adhesion between two different layers. Though it was a better recoating technique as compared to constrained surface, however this too has many limitations. The first limitation being that it is time consuming because only one side of the blade was used for recoating and one has to wait for suspension to settle down after sweeping. And the second limitation which was reported by many authors is destruction of previously fabricated layer while sweeping with doctor blade. However

this limitation was not observed by us. We have used sufficiently high laser power so that there would be greater fusion between successive layers. Hence for fabrication of ceramic parts with high aspect ratio doctor blade technique proved better over constrained surface.

Conclusion

Millimeter size ceramic parts with sub millimeter feature size were fabricated using both constrained surface as well as free surface (doctor blade technique) technique. It was found that for ceramic parts having high aspect ratio free surface technique was most suitable for layer recoating. If sufficiently high laser power is used the destruction of individual layers while sweeping with doctor blade can be eliminated.

References

- [1] X. Zhang, X. N. Jiang, C. Sun "Microstereolithography of polymeric and ceramic microstructures" Sensors and Actuators 77 1999 149-156
- [2] Håkan Elderstig and Olle Larsson "Polymeric MST - high precision at low cost" 1997 J. Micromech. Microeng. 7 89
- [3] Arnaud Bertsch, Sebastian Jiguet and Philippe Renaud "Microfabrication of ceramic components by microstereolithography" J. Micromech. Microeng.14 (2004) 197-203
- [4] M L Griffith, J W Halloran Free form fabrication of ceramics via stereolithography, Journal of American ceramic society 79(1996) 2601-2608.
- [5] A Licciulli, C. Esposito Corcione, A. Greco, V. Amicarelli, A. Maffezzoli "Laser stereolithography of ZrO₂ toughened Al₂O₃" Journal of European Ceramic society 25 (2005) 1581-1589
- [6] Michelle L. Griffith, John W. Halloran "Scattering of ultraviolet radiation in turbid suspensions" J. Appl. Phys. 81, (1997) 2538-46
- [7] Olivier Dufaud, Philippe Marchal, Serge Corbel, 2002 "Rheological properties of PZT suspensions for Stereolithography" Journal of European ceramic Society, 2081-2092

SCREEN PRINTING OF DYE SENSITIZED SOLAR CELLS

Venumadhav More, Bheem Singh and Parag Bhargava

IIT Bombay, Mumbai, India.

Abstract

Low processing cost of dye sensitized solar cells (DSSCs) and their better performance in diffuse light, slightly higher temperature makes them an attractive option for photovoltaic energy generation. Till date 13% photo conversion efficiency has been obtained for DSSCs at lab scale but commercialization of DSSCs not yet happened. Large scale production of DSSC requires manufacturing processes to be easily scalable, and cost effective. Screen printing technique has the potential of large area uniform deposition of titania film for photoanode. Titania paste used in the screen printing should have thixotropic property to obtain reproducible titania film characteristics. Properties of titania films like thickness, porosity, connectivity of particles affects efficiency of DSSC. These characteristics of titania films depend on the composition of the paste and method used for paste preparation. In present work effect of viscosity of titania paste and screen printing parameters on the morphology of screen printed titania film has been studied and Screen printing has been utilized to print large area (15 cm² active area) photoanodes. The screen printing has also been utilized in part to develop other aspects of photoanode and counter electrode of DSSCs.

Key words: Dye sensitized solar cell, Screen printing, Paste

1. Introduction:

Development of dye-sensitized solar cells (DSSCs) is inspired by the natural process of photosynthesis.^[1] DSSCs are considered to be an attractive candidate to replace the most common silicon based solar cells due to low production cost, use of environmentally friendly materials, easy fabrication process, high transparency and potential to be used as a flexible energy providing device.^[1] A discovery in 1991 which demonstrated that sensitizing titanium dioxide photoelectrode covered with organometallic dye can be useful for fabrication of photoelectrochemical cells triggered research on dye sensitized solar cells.^[2] Power conversion efficiencies of about 5 to 12 % can be achieved depending on cell size and its configuration.^[3]

Crystalline silicon solar cells still dominate the photovoltaic market due to their high efficiency.^[4] Sun is a clean source of energy as producing energy by harvesting solar

radiation does not result in production of any harmful pollutant.^[5] Solar PV is a steadily growing energy technology which is gaining tremendous popularity because it can produce electricity near the end user, avoiding transmission losses and costs. The solar PV panels operate without noise, toxicity, or greenhouse gas emissions.^[6]

Continuous use of fossil fuels has degraded natural resources as well as had undesirable environmental impact on human life like greenhouse effect.^[7] Increasing energy demand of society in future may be solved by solar photovoltaics which avoid problems that arise due to conventional energy sources. The ease of processing dye sensitized solar cells over that of silicon solar cells, has created interest in academia as well as industries.^{[7][8]}

Dye sensitized solar cells have not yet been commercialized due to issues with their long term stability and low efficiency compared with silicon solar cells. As size of the dye

sensitized solar cell increases efficiency rapidly decreases due to high resistance of conducting oxides(TCO).^[9]One of the key advantage of dye sensitized solar cell is that the efficiency of cell remains practically unchanged under diffused light and slightly elevated temperature. While efficiency of silicon solar cells depends on the intensity of light.^[10]

The present article describes work carried out towards fabrication of dye sensitized solar cells by screen printing. Screen printing is utilized for masking of the substrate at different stages of coatings and printing of the mesoporous titania layer using pastes. Understanding the rheology of titania pastes is critical to successful screen printing of mesoporous titania layer. The learning from the systematic studies on screen printing is applied towards development of large area dye sensitized solar cells.

2. Experimental details

2.1 Materials

The following materials were used in the present study. Fluorine doped tin oxide coated glass (FTO) (TEC7, sheet resistance 8-9Ω/□ from Pilkington) used as substrates. TiO₂ nanopowder (P25, Degussa) used as active component in paste. Ethylcellulose (Aldrich) used to adjust viscosity as well as it acts as binder. Terpineol (99% Spectrochem) used as solvent for paste. Ethanol was (Name of company, China) used as solvent for mixing during paste preparation. RuL₂(NCS)₂ (L=2,2'-bipyridyl-4,4'-dicarboxylic acid) known as N3 dye (Dyesol) is used to adsorb on titania particles. 1-methyl-3-propylimidazolium iodide (PMII)(98% Aldrich), Lithium iodide (anhydrous Merck), acetonitrile (Merck 98%) are used to prepare electrolyte for cell.

2.1.1. Preparation of screen printable titania paste

6 gm titania powder was taken in a propylene bottle to which 2 ml of glacial acetic acid and 100 gm grinding media was added. The powder was mixed on the roller mill for 30 minutes at 90 rpm. Distilled water (2ml) was added to the propylene bottle containing titania powder and milled for another 30 minutes. Ethanol (30 ml) was added to the polypropylene bottle and mixed for 30 minutes. After 30 minutes of milling another 100 ml of ethanol added and milling continued for 30 another minutes. To the bottle containing titania slurry 21.5 ml of terpineol added slurry mixed for 30 minutes on roller mill. After milling 3 gm of ethylcellulose (10 weight percent solution in ethanol) was added to the titania slurry and milled for 24 hours. After roller milling for 24 hours slurry was removed from the bottle and grinding media separated using sieve. Ethanol from the slurry is evaporated using a rotary evaporator. Evaporation of ethanol is done initially at 35°C with vacuum 120 mbar and vacuum level increased till 10 mbar to completely evaporate ethanol. After evaporation of ethanol paste formed is characterized using rheology and laser diffraction to determine the viscosity and the particle size of the titania in paste. Effect of the ethanol amount in the paste on rheological characteristics and the morphology of screen printed film was also studied.

Table 1: Composition of screen printable paste

| Components of paste | Wt. percent after evaporation of alcohol |
|---------------------|--|
| TiO ₂ | 19.8 |
| Acetic acid | 6.60 |
| Water | 6.60 |
| Ethylcellulose | 0.99 |
| Terpineol | 66.0 |

2.2 Screen printing of titania (TiO₂) paste

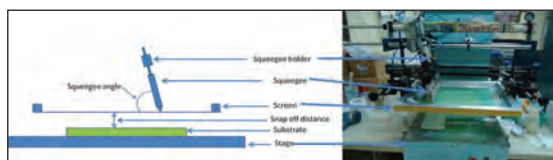


Fig.1 Schematic and photo of screen printer

Screen printing was done by using the titania paste after evaporation of ethanol to determine the effect of screen printing parameters on the morphology and thickness of screen printed film. To understand the effect of ethanol present in the paste on the morphology, thickness of screen printed titania films, intentionally 0 to 15 weight percentage of ethanol was added to the paste (from which ethanol was completely evaporated earlier) and then screen printing was carried out.

2.3 Characterization

To check adsorption of acetic acid on TiO₂ particles FTIR (Jasco) instrument was used. Particle size of TiO₂ particle in screen printable paste was determined by DelsaNanoC (Beckman Coulter). Rheological characteristics of screen printable paste were determined using Rheometer (Brookfield), Photo current measurement of cell was done by Newport solar simulator and Keithley source meter (2420), dye loading measured by UV-Vis spectrometer (Jasco V650). Images of screen printed films were taken using a stereo microscope (Leika)

2.4 Results and discussion

2.4.1 Deagglomeration of TiO₂

During slurry preparation water added helps in dissociation of acetic acid. Dissociated acetic acid must adsorb on the titania particles and act as dispersing agent. Peaks at 1447-1452 cm⁻¹

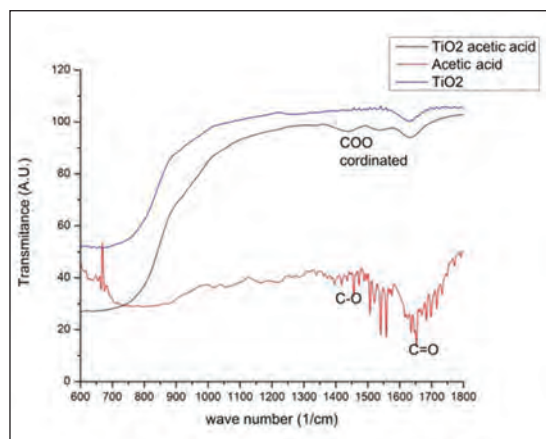


Fig.2 IR spectra Acetic acid mixed with TiO₂

region (surface-coordinated acetate) and the 1418-1423 cm⁻¹ region (aqueous acetate ions) in IR spectra confirm adsorption of acetic acid on TiO₂ shown in figure 2.^[11] Ethyl cellulose acts as a viscosity controller in the paste as well as a pore former at later stage of heat treatment. Terpineol added acts as a solvent in which TiO₂ particles are dispersed. Ethanol is added to ensure mixing of all components of the paste though ethanol is removed from the paste prior to screen printing. TiO₂ particle size of 391 nm was observed when acetic acid was used in paste preparation. While when acetic acid was not used in paste preparation then TiO₂ particle size of 535 nm was observed. Zeta potential of TiO₂ particles was higher when acetic acid used in paste preparation in comparison with zeta potential obtained when acetic acid was not used in paste preparation.

Table 2: Particle size and zeta potential of TiO₂ obtained in particle size analysis

| Paste | Particle Size d ₅₀ (nm) | Zeta potential (mV) |
|---------------------------|------------------------------------|---------------------|
| Paste with acetic acid | 391 | -9.34 |
| Paste without acetic acid | 535 | -3.59 |

2.4.2 Rheological study of screen printable paste

2.4.2.1 Rheology of titania slurry at different time of ethanol evaporation.

Screen printable slurry without evaporation of ethanol shows Newtonian behavior. Prior to evaporation and after half of ethanol was removed evaporation viscosity was so low that it could not be measured in the rheometer. Slurry showed similar Newtonian behavior, with viscosity remaining lower than the minimum measurement value. (Fig. 3) Complete removal of ethanol increased viscosity of paste and paste showed shear thinning behavior. At lower shear rates below 10 s^{-1} paste had higher viscosity (around 7 Pa.s) with increase in shear rate, viscosity decreased drastically. At shear rate higher than 100 s^{-1} paste behaves like Newtonian fluid. At 100 s^{-1} shear rate paste shows constant viscosity of 0.9 Pa.s . Ethyl cellulose solution used was added in paste to control viscosity. A $10 \text{ wt } \%$ ethyl cellulose solution in ethanol shows Newtonian behavior at all applied shear rates.

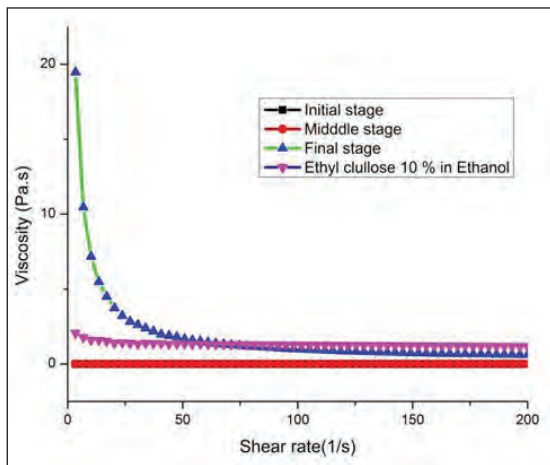


Fig.3 Viscosity change at different stages of ethanol evaporation from the titania paste.

During evaporation of ethanol it was difficult to control how much quantity of ethanol got removed. To understand effect of ethanol on the viscosity of paste all ethanol in paste was removed and then intentionally 5, 10 and 15 weight percentage of ethanol were added in the paste. After addition of ethanol, paste mixed using pot milling and then viscosity of all pastes was measured. Viscosities of paste with different amount of ethanol added externally are shown in Fig. 4.

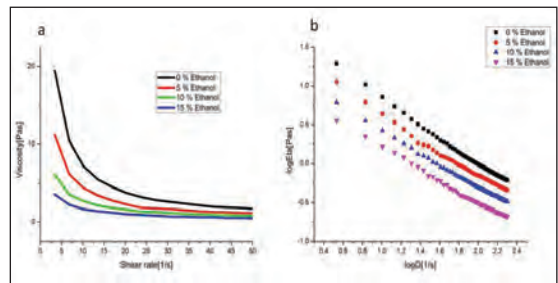


Fig.4 Viscosity of screen printable paste with 0, 5, 10 and 15% of ethanol (a). log-log plot for pastes with 0, 5, 10 and 15% of ethanol

Table 3: Effect of ethanol amount on rheological parameters of screen printable paste

| Ethanol wt percentage (%) | Viscosity at 50 s^{-1} (Pa.s) | Slope value | n value |
|---------------------------|---|-------------|---------|
| 0 | 1.6 | -0.8288 | 0.1712 |
| 5 | 1.0 | -0.7479 | 0.2521 |
| 10 | 0.6 | -0.7071 | 0.2929 |
| 15 | 0.4 | -0.702 | 0.298 |

During screen printing when the squeegee moves it will apply shear on the paste. Due to application of shear paste became flowable or viscosity of paste decreases and it flows through the perforated part of screen forming a pattern on the substrate. When squeegee stops viscosity of paste increases to maintaining printed pattern as well as avoid bleeding of the paste.

2.4.3 Effect of viscosity of paste on the screen printed film

2.4.3.1 Effect on the morphology of screen printed film.

With increase in ethanol weight percentage from 0 to 15 %, non uniformity of the printed film increased as shown in Fig.13. During screen printing bleeding was observed in case of 15% ethanol paste due to its low viscosity. In other pastes with 5% and 10% ethanol addition bleeding was less, but deposition of paste was not uniform. Some paste was removed from deposited portion by screen when it lifted after squeegee action. As viscosity of 0 % ethanol paste is higher than other pastes less amount of paste was removed from deposited part. Due to this 0% ethanol paste showed better uniformity than 5, 10 and 15 % ethanol paste (Fig. 5).

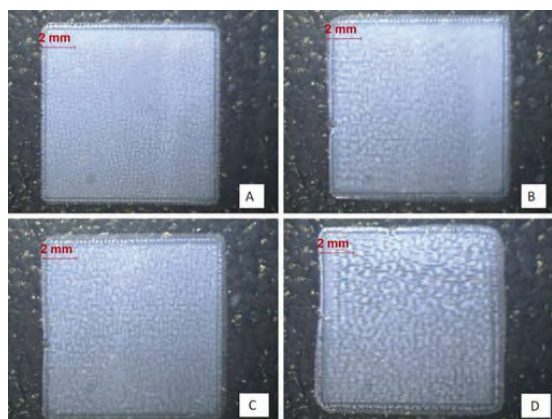


Fig.5 Appearance of screen printed and sintered (450o) films made from paste with 0% (A), 5% (B), 10% (C) and 15% (D) weight percent ethanol.

2.4.3.2 Effect on the thickness of screen printed film

Change in viscosity of paste also affected thickness of the screen printed film. Thickness of screen printed films increased with increase

in the viscosity of paste. Paste with 0% ethanol has a viscosity 1.6 Pa.s(at 50 s⁻¹) and film thickness obtained from 0 % ethanol paste was 2.6 micrometer. As viscosity decreased from 1.6 to 0.4 Pa.s(at 50 s⁻¹) with increase in ethanol, thickness of screen printed film decreased to 1.9 micrometer.

Table 4: Effect of viscosity of paste on the thickness of sintered screen printed films and on cell efficiency

| Ethanol content (%) | Viscosity at 50 s ⁻¹ (Pa.s) | Film thickness (μm) | Efficiency (%) | Dye loading (mM/cm ²) |
|---------------------|--|---------------------|----------------|-----------------------------------|
| 0 | 1.6 | 2.6 | 2.29 | 1.95 × 10 ⁻⁸ |
| 5 | 1.0 | 2.4 | 2.30 | 1.80 × 10 ⁻⁸ |
| 10 | 0.6 | 2.2 | 2.11 | 1.90 × 10 ⁻⁸ |
| 15 | 0.4 | 1.9 | 1.84 | 1.6 × 10 ⁻⁸ |

Along with viscosity of paste screen printing parameters like snap off distance, squeegee pressure, squeegee angle, speed of squeegee affect the uniformity of screen printed film.

2.4.4 Effect of screen printer parameters on morphology of the screen printed film

2.4.4.1 Effect of snap off distance

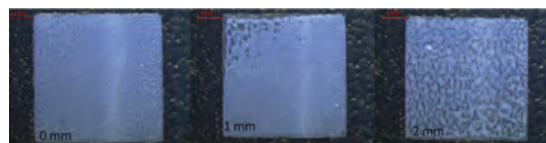


Fig.6 Effect of the snap off distance 0 mm, 1mm and 2mm on morphology of screen printed film.

To study the effect of snap off distance on the morphology, screen printing was done using paste with 0% ethanol and snap off distance was varied from 0 to 3 mm. Other screen printer parameters such as squeegee angle (45°), speed (40mm/s), pressure (5mm) are kept constant. Snap off distance of 0 mm is not actually 0 but is the lowest distance possible to adjust. When snap off distance was above 2mm distance, no print could be obtained.

During screen printing, screen touches to the substrate by squeegee pressure and as squeegee moves, paste passes through the perforated part of screen and prints on the substrate. When squeegee moves, portion of screen behind the squeegee lift upwards due to tension of screen. When snap off distance is 0 mm, screen directly touches to the substrate without squeegee pressure and when it lifts off after squeegee movement, screen will take out some paste from deposition. When snap off distance is 2 mm then screen does not touch the substrate and deposits only small amount of paste. 1 mm snap off distance is optimum for good film deposition by screen printing. For further experiments snap off distance was kept as 1mm. Effect of snap off distance on the appearance of screen printed film is shown in Fig.6.

2.4.4.2 Effect of squeegee pressure

Squeegee pressure mainly decides thickness of the screen printed film. Along with the thickness, morphology of the screen printed film depends on the squeegee pressure. To study the effect of squeegee pressure screen printing was done on FTO glass using 0 % ethanol paste. Squeegee pressure was varied from 0 mm to 10 mm, all other parameters - snap off distance (1mm), squeegee angle (45°), speed (40 mm/ s) were kept constant as shown in Table 5.

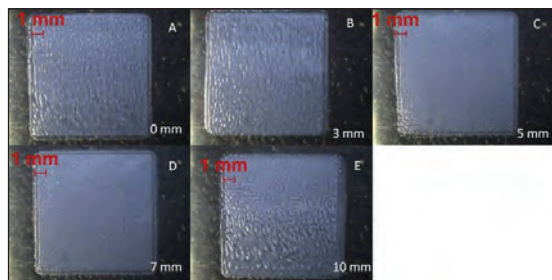


Fig.7 Variation of squeegee pressure from 0 mm to 10 mm on the morphology of screen printed film.0mm(A), 3mm (B), 5mm(C),7mm(D) and 10mm(E)

In experiment actual squeegee pressure was not measured but height of squeegee was varied from 0 mm to 10 mm which increases squeegee pressure on screen. If squeegee pressure is in between 0 mm to 3 mm, this pressure is insufficient to stretch the screen and touch to substrate then very small amount of paste is deposited on the substrate as shown in Fig. 7 A and 7 B. But if the squeegee pressure is sufficiently large (10 mm) such that it will deform squeegee then, amount of paste passed through the screen changes and non uniform film is obtained as shown in Fig.7 E. When squeegee pressure was between 5 mm to 7 mm it formsa continuous film as shown in Fig. 7 C and 7 D.

Table 5: Effect of squeegee pressure on the thickness of screen printed film.

| Squeegee pressure(mm) | Film thickness (µm) | Ra(A) |
|-----------------------|---------------------|-------|
| 0 | 2.70 | 6337 |
| 3 | 2.85 | 5745 |
| 5 | 2.90 | 6679 |
| 7 | 3.07 | 6149 |

Based on the experiments carried out with varying screen printer parameters the conditions identified for best screen printed film in terms of appearance were

Table 6: Optimized parameters of screen printer

| Parameters | Values |
|-------------------------------------|----------|
| Viscosity of paste at 50 shear rate | 1.6 Pa.s |
| Snap off distance | 1mm |
| Squeegee angle | 45° |
| Squeegee pressure | 5mm |
| Squeegee speed | 40 mm/s |

Screen printed titaniafilm obtained from the paste with 0% ethanol and optimized parameters and sintered to 450°C is shown in Fig.8.

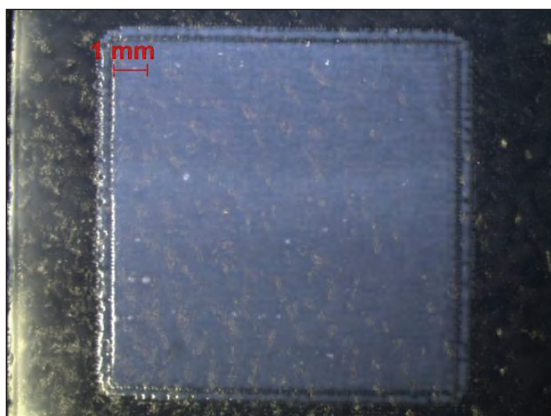


Fig.8 Screen printed film with optimize composition and parameters of screen printer

3 Fabrication of large area dye sensitized solar cell

3.1 Photoanode

A] Substrate preparation:

Fluorine doped tin oxide coated glass (FTO) was cut into rectangular shape 7mm×6mm dimensions. After cutting of FTO they were cleaned by using bath sonication in different solvents to remove organic contamination. Solvent used in cleaning was soap solution, ethyl alcohol and distilled water. For cleaning of the substrates sonication was carried out for 15 minutes in each solvent, used in sequence one after another as listed. After sonication substrates were dried at 100°C in a recirculating oven.

B] Compact later deposition

Compact layer was deposited on cleaned substrate by dip coating technique. Dip coating was done by using TiO_2 sol and UTM machine. Substrate was dipped in the sol and withdrawn at uniform speed using UTM machine. TiO_2 sol used in dip coating was prepared by hydrolysis of Titanium iso-propoxide. Coating of compact layer is needed only on the area

where active layer has to be deposited later. For making compact layer only on certain areas, all other areas of substrate were masked by coating ethylcellulose on it. Coating of ethylcellulose was done by screen printing. For screen printing, 10 weight percentage ethylcellulose solution in ethanol was used. After coating ethylcellulose on the cleaned substrate, it was heated for 30 minutes at 100°C in oven to improve adhesion of ethyl cellulose on the FTO. After heating, ethylcellulose coated substrate is cooled to room temperature, and attached to holder of UTM machine. By using UTM machine, substrate was inserted in beaker containing TiO_2 sol. Substrate remain dipped for 5 minutes and after 5 minute substrate was removed from container with uniform speed of 500 mm per minutes. Substrates was removed with speed of 500 mm per minute gives thickness of compact layer around 150 nm (Fig.9). After removing substrate from sol it was dried at room temperature for 30 minutes and then heat treated to 450°C. Heat treatment is essential for sintering of compact later as well as removing of ethylcellulose from substrate. After heat treatment substrate was furnace cooled and after cooling it was used for screen printing of active layer.

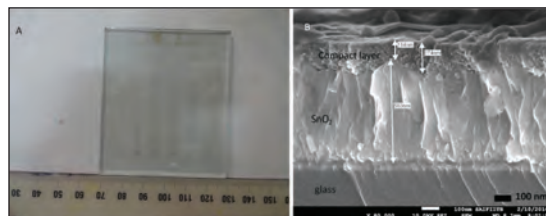


Fig.9 Photo of compact FESEM image of sintered compact layer deposited on FTO

C] Screen printing of TiO_2 active layer

Substrate containing compact layer was taken and active layer of mesoporous TiO_2 was screen printed over the already deposited compact layer. Screen printing of active layer was done

by using TiO_2 paste. Paste used for active layer coating was prepared by mixing TiO_2 powder with acetic acid, water, ethanol, terpineol and ethylcellulose as described earlier. Finally ethanol was evaporated to obtain paste of printable viscosity. After screen printing of active layer, substrate was heated to 450°C for sintering of active layer (Fig.10). Heat treatment increased interconnection of TiO_2 particles by neck formation as well as during heat treatment organics in paste were burnt off. After heat treatment of substrate containing compact and active layer it was furnace cooled to room temperature. The substrates when above 100°C during the cooling cycle were taken out and dipped in dye solution for dye adsorption (Fig. 10 B).

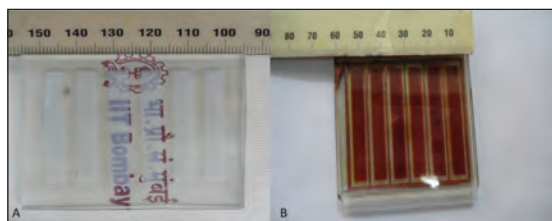


Fig.10 Titania screen printed films (A) Sintered (450°C) TiO_2 film, (B) Sintered (450°C) with cu current collecting fingers and dye,

3.2 Counter electrode

A] Substrate preparation

Fluorine doped tin oxide coated glass (FTO) was cut into rectangular shape $7\text{mm} \times 6\text{mm}$ dimensions. After cutting of FTO they were cleaned as described in section 3.1 A

B] Dip coating of platinum

Cleaned substrate was taken and it was immersed in the beaker containing platinum sol. Platinum sol was prepared from reduction of hexa-chloro platinum acid in Isopropanol and polyvinyl pyrrolidene (PVP). Platinum sol contains PVP capped platinum nanoparticles of size 2 to 5 nm (Fig.11). Substrate was kept

dipped for 15 minutes and after 15 minutes removed from beaker and heated to 450°C . Heating was helpful for enhancing adherence of platinum nanoparticles to FTO substrate and removal of organics from nanoparticles. After heat treatment of substrate, it was furnace cooled to room temperature.



Fig.11 Dip counter electrode after heat treatment at 450°C (A), Counter electrode with Cu current collecting fingers(B), TEM image of platinum solused for dip coating(C)

On the substrates copper was electrodeposited as current collection fingers. The prepared electrodes were put together using a spacer cum sealant (Surlyn, DuPont thermoplastic sealant). The sealed cells with predrilled holes on the conterelectrode were filled with the liquid electrolyte followed by sealing of the holes to complete the fabrication.

Conclusion

To obtain continuous and uniformly thick titania films by screen printing both screen printer as well as paste parameters has to be optimized. Paste used in the screen printing has to be thixotropic and the titania in the paste. The best paste was from the view of screen printing was the one from which entire ethanol was evaporated away using a rotary evaporator. Individual titania layers of thickness around $2 - 3 \mu\text{m}$ can be screen printed. Screen printing was demonstrated to be suited for fabrication of large area dye sensitized solar cells..

Reference

- [1] H. J. Choi, J. E. Shin, G.-W. Lee, N.-G. Park, K. Kim, and S. C. Hong, "Effect of surface modification of multi-walled carbon nanotubes on the fabrication and performance of carbon nanotube based counter electrodes for dye-sensitized solar cells," *Curr. Appl. Phys.*, vol. 10, no. 2, pp. S165-S167, Mar. 2010.
- [2] H. Tributsch, "Dye sensitization solar cells: a critical assessment of the learning curve," *Coord. Chem. Rev.*, vol. 248, no. 13-14, pp. 1511-1530, Jul. 2004.
- [3] J. Walter and D. Mierzwi, "Properties of screen-printed modified graphite layers," *ARCHIVES of FOUNDRY ENGINEERING*, vol. 10, no. 3, pp. 153-156, 2010.
- [4] J. Xia and S. Yanagida, "Strategy to improve the performance of dye-sensitized solar cells: Interface engineering principle," *Sol. Energy*, vol. 85, no. 12, pp. 3143-3159, Dec. 2011.
- [5] N. S. Lewis, "A perspective on forward research and development paths for cost-effective solar energy utilization," *ChemSusChem*, vol. 2, no. 5, pp. 383-6, Jan. 2009.
- [6] P. Joshi, L. Zhang, D. Davoux, Z. Zhu, D. Galipeau, H. Fong, and Q. Qiao, "Composite of TiO₂ nanofibers and nanoparticles for dye-sensitized solar cells with significantly improved efficiency," *Energy Environ. Sci.*, vol. 3, no. 10, p. 1507, 2010.
- [7] L. J. Brennan, M. T. Byrne, M. Bari, and Y. K. Gun'ko, "Carbon Nanomaterials for Dye-Sensitized Solar Cell Applications: A Bright Future," *Adv. Energy Mater.*, vol. 1, no. 4, pp. 472-485, Jul. 2011.
- [8] Y. Zhao and C. Burda, "Development of plasmonic semiconductor nanomaterials with copper chalcogenides for a future with sustainable energy materials," *Energy Environ. Sci.*, vol. 5, no. 2, p. 5564, 2012.
- [9] H. Seo, M. Son, J. Hong, D.-Y. Lee, T.-P. An, H. Kim, and H.-J. Kim, "The fabrication of efficiency-improved W-series interconnect type of module by balancing the performance of single cells," *Sol. Energy*, vol. 83, no. 12, pp. 2217-2222, Dec. 2009.
- [10] M. Grätzel, "Solar energy conversion by dye-sensitized photovoltaic cells," *Inorg. Chem.*, vol. 44, no. 20, pp. 6841-51, Oct. 2005.
- [11] Y. Cheng, J. Guo, X. Liu, A. Sun, G. Xu, and P. Cui, "Preparation of uniform titania microspheres with good electrorheological performance and their size effect," *J. Mater. Chem.*, vol. 21, no. 13, p. 5051, 2011.

STUDY ON EFFECT OF ADU CALCINED U_3O_8 ADDITIVE ON UO_2 PELLET CHARACTERISTICS

N. Santra, T. K. Sinha, A. K. Singh, Dr. D. S. Setty, G. Kalyana Krishnan & N. Saibaba

Nuclear Fuel Complex, Hyderabad, India.

Abstract

Uranium dioxide (UO_2) in the form of cylindrical pellet is widely used as nuclear fuel material for generating nuclear power all over the world. Indian pressurized heavy water reactor (PHWR) uses natural UO_2 pellets (0.7% U^{235}) as its fuel material. PHWR requires very stringent quality specification of its fuel pellets in terms of pellet integrity, density and chemical purity. Maintaining required quality of the pellet consistently is one of the most challenging tasks for the fuel fabricators around the world. Nuclear Fuel Complex (NFC) manufactures natural UO_2 pellets by powder metallurgy (PM) route i.e. powder compaction, high temperature sintering followed by centreless wet grinding method from the stabilized UO_2 powder derived through ADU-route. The pelletizing plant frequently come across the chronic problem of physical integrity of the pellets in terms of end caps, chips, cracks, pits etc. Those defects are generated due to various attributes like the change in UO_2 powder fabrication parameters, lot characteristics and consequent pelletizing parameters etc. The physical defects of the pellet affect the performance of the reactor adversely in many ways. Those defective pellets get rejected without further processing in the plant. Thus the overall recovery of the plant goes down significantly due to poor visual recovery of the pellets. To overcome the physical defects of the pellet, NFC has introduced an innovative technique of doping U_3O_8 powder into UO_2 granule before final compaction operation. The U_3O_8 powders are produced from the calcination of ammonium diuranate (ADU) at about $700^\circ C$ temperature. The trials were carried out with different quantities of U_3O_8 addition in number of UO_2 powder lots. The pellets were sintered in high temperature ($1700^\circ C$) continuous sintering furnace, batch sintering furnace and dilatometer for comparison purpose. The U_3O_8 doped green pellets have exhibited excellent sintering behavior in every case. Encouraging results of the physical integrity and density of the UO_2 finished pellets were observed after addition of U_3O_8 powder in optimum quantity at about 4-6 wt%. The plant has so far produced about 300 MT of UO_2 fuel pellets in this route without any adverse effect. U_3O_8 powder modifies the UO_2 pellet characteristics in different ways. The paper discusses the various experimental trials, observation and discussion on the effect of U_3O_8 powder on UO_2 pellet characteristics viz. physical integrity, sintered density, and microstructure.

Key words: PM route, natural UO_2 pellet characteristics, ex-ADU, U_3O_8 doping, physical integrity, pellet density etc.

1. Introduction:

Nuclear fuel complex (NFC), an industrial unit of Department of Atomic Energy (DAE) has been manufacturing natural UO_2 fuel assembly for supplying all the PHWR's in

India. Powder metallurgy route is followed for the fabrication of fuel pellets. Achieving tightly specified quality of the finished pellet depends both on UO_2 powder fabrication variables and subsequent pelletizing parameters.

STUDY ON EFFECT OF ADU CALCINED U_3O_8 ADDITIVE ON UO_2 PELLET CHARACTERISTICS

The brief process flow sheet for the production of UO_2 powder and fuel pellets shown in Fig. 1

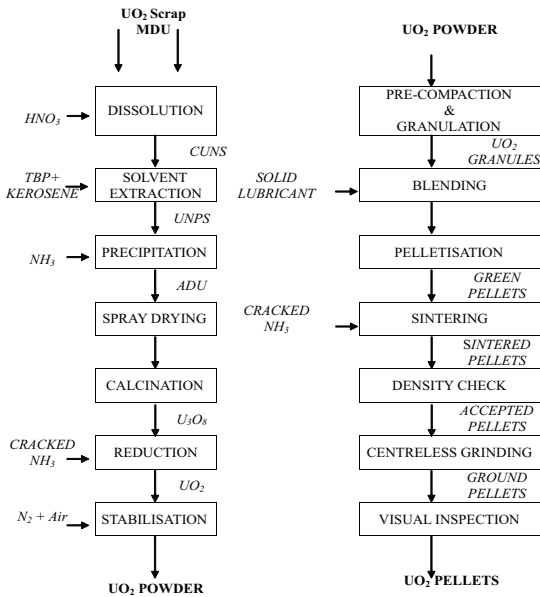


Fig. 1 Flow sheet for the production of UO_2 pellets

Physical integrity, density and the chemical purity are the most significant characteristics of the UO_2 fuel pellets. The pelletizing plant occasionally land up with the problem of physical defects like end caps, chippings, cracks, pits of the pellets. Those defective pellets are getting rejected and recycled later in the powder fabrication plant. Thus the overall recovery of the pelletizing plant gets affected badly due to poor visual recovery of the pellets. To overcome the problem of visual defects of the pellets, plant has introduced an innovative technique of doping of U_3O_8 powder into the UO_2 granule before final compaction stage followed by regular operation of sintering and wet grinding. This has tremendously improved the quality of the finished pellets by enhancing the fuel integrity and sintered density. U_3O_8 powder generated from the calcinations of ammonium diuranate (ADU) helps to remove

the defects like end caps and cracks of the UO_2 pellets significantly. The plant has so far produced about 300 MT of finished UO_2 pellets in this route with higher overall recovery at above 80%. So far, much study has not been reported earlier on this aspect [1].

2. Experimental:

- a) Selected UO_2 powder lot number: NU 921
- b) Dopant U_3O_8 powder lot number: NU 867
- c) Quantity of U_3O_8 addition: 2%, 4%, 6%, 8% and 10% by weight

Five categories of blend were prepared by adding 2%, 4%, 6%, 8% and 10% U_3O_8 powder into UO_2 granules. The granules were obtained by pre-compaction and granulation of as received virgin UO_2 powder at about 80-100 MPa pressure to make it free flowable for final compaction. The maximum size of UO_2 granule was about 1-1.5 mm. The initial O/U ratio of the virgin powder was 2.045 and BET specific surface area was 2.9 m^2/g . U_3O_8 powder additives were produced through calcinations of ammonium diuranate (ADU) at about 700 C temperature. The BET specific surface area of the dopant U_3O_8 was 3.4 m^2/g . Homogenization of U_3O_8 mixing was ensured by checking the O/U ratio of each blend. The various U_3O_8 quantities are chosen in view that the optimum results should be obtained with the minimum quantity addition. Mechanical mixing of such less quantity additive was done by preparing master blend with highest quantity of U_3O_8 addition i.e. 10% and then making dilution by adding UO_2 granules as per the various percentages required for the trials. Powder blends were final compacted in double acting die compaction with solid admixed lubricant (0.3wt %) at a pressure of about 275-300 MPa. In a single cycle of final compaction,

STUDY ON EFFECT OF ADU CALCINED U_3O_8 ADDITIVE ON UO_2 PELLET CHARACTERISTICS

twelve green pellets were produced from each category of blend. The green densities of the pellets were in the range of 52-54%TD which was similar as in the regular production. Thus total sixty numbers of green pellets were produced with five category blends. From each category of green pellets, four were sintered in high temperature (1700°C) continuous pusher type sintering furnace, four were sintered in batch sintering furnace and two were sent for dilatometer analysis along with regular conventional UO_2 pellets without any dopants for comparison. Soaking period of 8-10 hrs was ensured at the temperature of 1700°C in batch sintering furnace and continuous sintering furnace. Cracked ammonia gas atmosphere were maintained inside the furnace as reducing atmosphere. Ar-8% H_2 atmosphere were maintained in dilatometer for pellet sintering. All the other parameters of powder compaction and sintering were maintained same as in the regular commercial production. The sintered pellet samples were analysed for sintered densities and metallographic examination after centreless wet grinding operation. Visual inspection was carried out to observe the physical integrity of the pellets. The surface roughness was also measured for the ground pellets. The ground pellet samples from different source were cut through longitudinal direction i.e. pellet axis, polished up to diamond finish and etched with 10% H_2SO_4 + 90% H_2O_2 solution to reveal the microstructure in SEM. Chemical compositional analysis, O/U ratio etc of the sintered pellets were carried out for confirming the homogenization of mixing, extent of reduction of U_3O_8 , retention of any additives etc.

3. Results and observation:

The sintering characteristics of the green pellets were studied by sintering in high temperature dilatometer at 1700°C followed by measurement of sintered densities through

immersion technique. The dilatometer shrinkage behavior is shown in Fig 2. The microstructures were observed in SEM to reveal the grain size, size of the pore, porosity content etc as shown in Fig 3. The presence of coring defect of the pellet was also studied through metallographic examination. Table 1 shows the green densities, sintered densities, grain sizes with respect to various quantity U_3O_8 additions. Few types of common visual defects of the pellets generated occasionally in regular fabrication route are shown for comparison with the accepted pellets. The surface roughness measured were about 1.2-1.4 μ r.m.s. which is comparable with regular pellet. Visually accepted pellets are shown in Fig. 4.

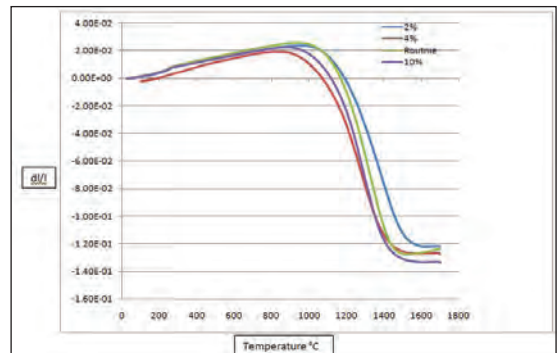


Fig. 2 Dilatometer data showing (d/l) Vs temperature for different pellets

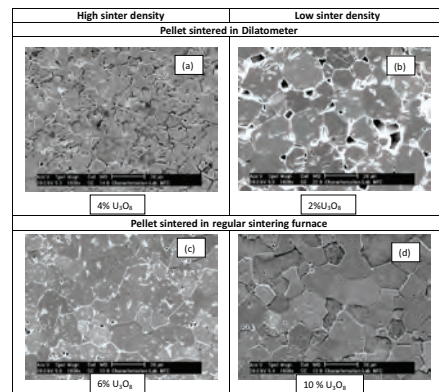


Fig. 3 SEM micrograph of various sintered pellets

STUDY ON EFFECT OF ADU CALCINED U_3O_8 ADDITIVE ON UO_2 PELLET CHARACTERISTICS

Table 1 shows sintered densities and average grain sizes

| % U_3O_8 | Green density | Sintered density (g/cc) | | Average Grain Size (μm) | |
|--------------|---------------|-------------------------|-----------------|--------------------------------|---------|
| | | Dilatometer | Regular furnace | Dilatometer | Furnace |
| 2 | 5.7 | 10.30 | 10.65 | 20 | 16 |
| 4 | 5.7 | 10.59 | 10.69 | 10 | 13 |
| 6 | 5.7 | 10.58 | 10.70 | 12 | 17 |
| 8 | 5.6 | 10.55 | 10.66 | 9 | 15 |
| 10 | 5.5 | 10.52 | 10.63 | 9 | 15 |
| Regular (0%) | 5.7 | 10.31 | 10.65 | 15 | 12 |



End Caps

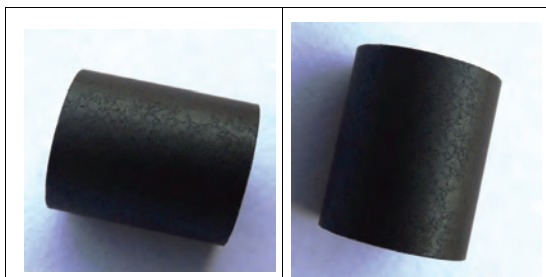


Cracks



Chipping

Pit



Visually Accepted Pellets

Fig.4. Visually accepted pellets

4. Analysis of sintering behavior:

- Sintering of 4% U_3O_8 doped pellet starts early, at lowest temperature among all i.e. at around 850°C. The percentage of shrinkage is around 12.7%.
- Sintering of 2% U_3O_8 and regular pellets started at around 1000°C. The percentage of shrinkage is around 12.2%.

Table 2 Observations on sintered densities and grain size w.r.t doping

| Dilatometer sintering | Regular sintering |
|--|---|
| <ul style="list-style-type: none"> 4% and 6% doped pellets gave the highest density and 2% doping gave the lowest density. | <ul style="list-style-type: none"> 4% and 6% doped pellets gave the highest density and 10% doping gave the lowest density. The density variation is negligible |
| <ul style="list-style-type: none"> Grain size variation with respect to doping was observed. | <ul style="list-style-type: none"> Samples sintered in plant were having nearly similar grain sizes |
| <ul style="list-style-type: none"> Average grain size was decreased as doping amount was increased. (20 μm for 2% and 9 μm for 10%) | <ul style="list-style-type: none"> Average grain size was having no particular trend with respect to doping. (16 μm for 2%, 15 μm for 10%, highest 17 μm for 4%) |

5. Discussion:

U_3O_8 acts like a cementing compound for the natural UO_2 pellet during powder compaction, sintering and grinding operations. Though the exact mechanism of U_3O_8 inside UO_2 lattice is yet to be investigated further, the tremendous improvement in the visual recovery of the finished pellet has been revealed for the optimum addition of 4-6%. Some studies were carried out in similar line by Pramanik et al^[2]. The following phenomena may take place during pressing and sintering:

- U_3O_8 being orthorhombic in structure compensates strain recovery during final compaction and ejection of UO_2 pellet having FCC structure.
- Orthorhombic U_3O_8 converts in to FCC UO_2 in reducing H_2 atmosphere and thus about 30% volume reduction occurs. Thus, it works as a pore former and produces number of open and closed pores inside UO_2 lattice that may reduce the stresses generated during sintering.

However, the sintered densities of the UO_2 pellets are not affected directly by U_3O_8 doping.

STUDY ON EFFECT OF ADU CALCINED U_3O_8 ADDITIVE ON UO_2 PELLET CHARACTERISTICS

There is a probability of reducing sintered density by U_3O_8 being itself a low density pore former inside UO_2 lattice during sintering. The microstructure shows bigger porosities in comparison with the regular pellet without U_3O_8 dopant. It has been observed that besides improving visual integrity of the pellets, U_3O_8 may help in achieving good sintered density also indirectly for particular type of UO_2 powder lots. The probable reason behind this phenomenon is given below:

Occasionally, the pelletizing plant suffers the problem of low sintered density of pellet due to coring defects in the pellets. It occurs generally for chemically active UO_2 powder as received lot. The outer surface of the pellet gets sintered at very fast rate without allowing sufficient time for the inner portion to get sintered due to lower inherent thermal conductivity of the pellet. The outer sintered impervious layer may not allow the pores, gases etc to come out of the pellet. The results is coring defect of the pellet. Addition of U_3O_8 gives porous structure inside the sintered pellet during conversion of U_3O_8 to UO_2 during pre-heating in H_2 atmosphere. Once porous structure is created thru out the cross section, sintering becomes uniform by letting the pores, gases to go out easily and hence restricting coring structure leading to low sinter density. At the same time sintered density of the U_3O_8 mixed pellet show lower density value within acceptance due to creation of more porous structure compare to normal density value of regular pellet without dopant. Extensive studies have been carried out with U_3O_8 dopant derived through calcinations of rejected UO_2 pellet earlier^[3] and sufficient reports on grain growth by the author's earlier study^[4]. U_3O_8 powder generated from calcinations of ADU have completely different morphology than the rejected UO_2 calcined U_3O_8 . In this study, ex-ADU U_3O_8 powders have much higher BET specific surface area than other route. Sintering

atmosphere being reducing, the beneficial effect of the sintering diffusivity due to higher O/U ratio is not utilized here. The added U_3O_8 powder gets reduced into UO_2 at the pre-heating zone of the furnace before entering into the sintering zone. This is evidenced from the O/U ratio measured after sintering. More future studies are required to investigate the effect of the dopant.

6. Acknowledgement:

The work was made possible thanks to Shri S.V. Ramana Rao, Characterization facility, NFC for his scientific contribution during metallographic sample preparation and SEM analysis at their laboratory. He gave valuable comments during preparation of this report. The author wish to extend thank to Shri Shashank Reddy, NFC also for carrying out the experimental trials along with his regular plant production activity.

7. References:

- [1] T.R.G. Kutty et al "Characterization and densification studies on ThO_2-UO_2 pellets derived from ThO_2 and U_3O_8 powders"- Journal of Nuclear Materials 335 (2004) 462-470
- [2] Pramanik et al "Innovative process technique to optimize quality and microstructure of UO_2 fuel for PHWR's in India"-conference proceeding at IAEA meeting, Switzerland'2009
- [3] Kun Woo Song et al "Sintering of mixed UO_2 and U_3O_8 powder compacts"- Journal of Nuclear Materials 277 (2000) 123±129
- [4] Santra et al "Metallurgical structure modification of UO_2 pelle during sintering-experience at NFC, Hyderabad-conference proceeding at CANDU, Canada, 2013.

EFFECT OF ZINC DOPING AT Cu^{2+} - SITE IN $\text{Y}_{2/3}\text{Cu}_3\text{Ti}_4\text{O}_{12}$ CERAMIC SYNTHESIZED BY SEMI-WET ROUTE

Sunita Sharma and K. D. Mandal

Indian Institute of Technology, (Banaras Hindu University), Varanasi, India.

Abstract

Undoped $\text{Y}_{2/3}\text{Cu}_3\text{Ti}_4\text{O}_{12}$ ceramic is analogous to $\text{CaCu}_3\text{Ti}_4\text{O}_{12}$ (CCTO) ceramic. Aim in the background is to develop a material potentially suitable for capacitor, resonator and filler applications in various microelectronic devices. This article discusses the most recent fabrication of Iron doped yttrium copper Titanate ceramic with composition, $\text{Y}_{2/3}\text{Cu}_{2.90}\text{Zn}_{0.10}\text{Ti}_4\text{O}_{12}$ (YCZTO), synthesized by Semi-wet route along with its microstructure and dielectric studies. Polycrystalline phase structure was identified by XRD showing the presence of all normal peaks of YCTO along with secondary phase CuO in minor. SEM images of the fractured surfaces of $\text{Y}_{2/3}\text{Cu}_{2.90}\text{Zn}_{0.10}\text{Ti}_4\text{O}_{12}$ sample sintered at 950°C for 12h revealed the presence of morphologically smooth surfaced bimodal grains having size in the range of 0.5-1.5 μm . The most intriguing feature is its dielectric response. Dielectric measurement of sintered YCZTO pellets exhibited considerably high dielectric constant $\epsilon_r \sim 2057$ - at room temperature and 36,348 at 500K at 100 Hz frequency.

Keywords: Perovskite; Dielectric dispersion; Grain boundary; Relaxation; Impedance spectroscopy.

1. Introduction

Scientific community are making their long term efforts to develop dielectric materials possessing high dielectric constant with low dielectric loss. The ultimate goal for such efforts is to miniaturize a variety of electronic devices with the same time upgrading their quality and performance. In contrast to regular ferroelectric, BaTiO_3 also exhibit high dielectric constant but is strongly temperature dependent with some phase transitions. But recently invented $\text{CaCu}_3\text{Ti}_4\text{O}_{12}$ (CCTO) has got advantage over BaTiO_3 , as its dielectric constant remains independent of both temperature (100 - 600K) and frequency (102-106 Hz) without any structural phase transition. The stunning discovery of high-dielectric-constant in $\text{CaCu}_3\text{Ti}_4\text{O}_{12}$ type perovskite has raised considerable interest for various research groups owing to its giant dielectric constant despite its centrosymmetric nature (space group Im_3) with BCC structure

(lattice parameter $a = 7.391\text{\AA}$). It shows typically high static dielectric constant value ($\epsilon_r \sim 104$ for bulk and 105 for single crystals) and moderately low dielectric loss (~ 0.10)^[1-7]. This behaviour is technically noticeable due to its various possible applications like enhancing the performance of capacitive elements ideally suitable for Multi-Layer Ceramic Capacitors (MLCC), super-capacitors, resonators and fillers applications. A lot of research activities have been carried out in order to understand its physical origin^[6-9]. The origin of high dielectric constant phenomena in CCTO is due to an extrinsic mechanism, arising from an internal barrier layer capacitance (IBLC)^[7,10] or a surface barrier layer capacitance (SBLC)^[8-9]. In spite of several controversies, IBLC mechanism is universally accepted. But it has some irrelevant basis from application point of view.

But $\text{CaCu}_3\text{Ti}_4\text{O}_{12}$ is not an exceptional at all, rather various isostructural materials based on

complex perovskite structure, like ACu₃Ti₄O₁₂ (A=Sr, Bi_{2/3}, Y_{2/3}, La_{2/3}, Nd_{2/3}, Sm_{2/3}, Gd_{2/3}, Dy_{2/3}) also exhibit with similar dielectric properties with good thermal stability possessing. Each of them could also be a promising candidate to replace relaxors as dielectrics [6, 9, 11]. Apart from this, a wide variety of doping or partial substitution may be carried out at the A, Cu or Ti-site of ACu₃Ti₄O₁₂, which may be suitable for different industrial applications. The choice of substituent to modify the physical properties of the material is based on many factors including charge neutrality, tolerance factor, the ionic radius and solubility. As we know partial isovalent substitution of metal cations in different interstices can improve properties associated with ferroelectricity and dielectric response in these materials due to the partial modification of mixed-valent structure. Further, structural flexibility and chemical versatility of the materials make them more suitable for device applications [12, 15] and it is quite inspiring to investigate systematically new ACu₃Ti₄O₁₂ like materials. Y_{2/3}Cu₃Ti₄O₁₂ (YCTO) is very much similar to CCTO and has the same crystal structure. Very few research articles are available on YCTO ceramic [16]. We have reported earlier the dielectric properties of Y_{2/3}Cu₃Ti₄O₁₂ ceramic by semi-wet route using solid TiO₂ at comparatively low sintering temperature and in short duration. It exhibits high dielectric constant ($\epsilon_r \sim 8434$) at room temperature and 100 Hz frequency. But it shows fairly high dielectric loss ($\tan\delta \sim 1.5-2.04$) in temperature range from 308-428 K which must be controlled [17].

A detail literature survey shows that not much work has been reported on Y_{2/3}Cu₃Ti₄O₁₂ (YCTO) compound which is isostructural to CCTO which may offer a large database to search for high dielectric constant materials. Being non-ferroelectric, lead-free and eco-friendly too, YCTO material exhibits a high dielectric constant with good thermal stability.

Presently, we have worked out to control the dielectric loss factor by doping of Zn²⁺ at Cu²⁺ site. In the present communication, we further explore this avenue and report on the microstructure and dielectric properties of Y_{2/3}Cu_{2.90}Zn_{0.10}Ti₄O₁₂ (YCZTO) with its microstructural investigations by X-ray Diffraction, Scanning electron microscopy and Transmission electron Microscopy. YCZTO compound shows fairly high dielectric constant with somewhat low dielectric loss. We hope this work will stress further the implementation of perovskites as a source of inspiration for designing eco-friendly capacitor material.

2. Experiment

Y_{2/3}Cu_{2.90}Zn_{0.10}Ti₄O₁₂ (YCZTO) powder was synthesized by semi-wet route using analytical grade chemicals Y(NO₃)₃·6H₂O [obtained from HiMedia, India], Cu(NO₃)₂·3H₂O, Zn(NO₃)₂, titanium dioxide (TiO₂) and glycine [obtained from Merk, India] having purity $\geq 99\%$ as starting materials. The crystalline phase structure of the sintered YCZTO was identified using an X-ray diffractometer (D/max-2550/PC, Rigaku, Tokyo, Japan) employing Cu-K _{α} radiation ($\lambda=1.5414 \text{ \AA}$). The morphology of the fractured surfaces of sintered YCZTO ceramic were characterized by scanning electron microscopy (SEM, Model JEOL JSM5410) and transmission electron microscopy (TEM, FEI Tecnai-20G²) with an accelerating voltage of 200 kV. Dielectric measurement data were taken by LCR meter (PSM1735-NumetriQ, Newton 4th Ltd, U.K.) with variation of temperature (300-500K) and frequency (100 Hz- 5 MHz).

3. Results and discussion

3.1 Microstructural details

X-ray diffraction pattern of YCZTO ceramic sintered at 950°C for 12 h is illustrated in Fig. 1(a) which clearly shows YCTO phase

along with the presence of minor secondary phase of CuO (JCPDS 80-1917). The main XRD diffraction peaks of YCZTO were found to have a good matching with CaCu₃Ti₄O₁₂ (JCPDS card no. 75-2188). XRD data were indexed on the basis of a cubic unit cell similar to CCTO. The lattice parameter and unit cell volume of YCZTO ceramic. The value of lattice parameter and unit cell volume was found to be 7.5339 Å and 427.6257 Å³ respectively as per least squares refinement method. The crystallite size obtained by Scherrer's formula was found to be 56 ± 6 nm^[18].

with the stoichiometric of YCZTO which is also supported by EDX results. The variation in grain size thereby leading to abnormal grain growth may be due to the presence of CuO rich phase in their samples of YCZTO ^[19-20]. No peaks due to liquid phase of CuO were observed in the powder XRD pattern. The CuO phase may contribute significant effects to promote the grain growth and densification of YCZTO ceramic. It is also established that increase in sintering temperature significantly promote the grain growth and microstructural densification. It is also clear from the Fig. 1(b) that YCZTO ceramic shows high degree of porosity. The high porosity may be attributed to the formation of oxygen vacancies during sintering. It may be also due to lower sintering temperature. Increase in sintering temperature may lead to decrease in porosity owing to the grain growth phenomena.

The bright field TEM image of sintered YCZTO ceramic is represented in Fig.1(c) which confirms its polycrystalline nature. The particles are well dispersed with high extent of agglomeration. The average particles are in the range of 39 ± 6 nm. However, the particle size obtained by TEM analysis is lesser than XRD results because a crystallite may consist of several particles.

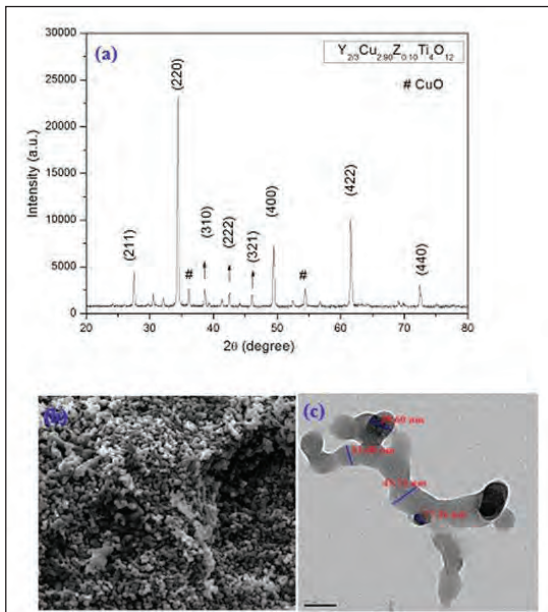


Fig. 1(a) XRD patterns (b) Scanning Electron Micrograph (c) Bright Field Transmission Electron Micrograph of Y_{2/3}Cu_{2.90}Zn_{0.10}Ti₄O₁₂ (YCZTO) ceramic sintered at 950°C for 12h.

Fig. 1(b) shows scanning electron micrograph of the fractured surface of sintered CCZTO ceramic which exhibits bimodal, smooth surfaced grains with frequent pores. The microstructure is dominated by small spherical, cylindrical and some cubical grains of sized 0.5-1.5 μm. The composition of grains coincides

3.2 Dielectric studies

Plots of dielectric constant (ε_r) and dielectric loss (tanδ) as a function of temperature for YCZTO ceramic at 0.1, 1, 10, 100 kHz are shown in the Fig. 2(a). It is clearly observed from the plot that dielectric constant at higher frequency (10 kHz and 100 kHz) is almost temperature independent under the investigated temperature ranges. But at lower frequencies (100 Hz and 1 kHz), a dielectric dispersion peaks were observed below 350 K, and thereafter the value of dielectric constant increases sharply to a higher value. At 100

EFFECT OF ZINC DOPING AT Cu^{2+} - SITE IN $\text{Y}_{2/3}\text{Cu}_3\text{Ti}_4\text{O}_{12}$ CERAMIC SYNTHESIZED BY SEMI-WET ROUTE

Hz, the value of dielectric constant increases from 886 at 303 K to 3775 at 327 K and then decreases to 826 at 347 K. However YCZTO ceramic shows exceptionally very high dielectric constant ($\epsilon_r \sim 20774$ at 100 Hz and 500 K) compared to other frequencies [17]. Increase in the value of dielectric constant with increase in temperature may be attributed to fact that as temperature increases, the orientation of interfacial polarisation get facilitated which enhances dielectric constant value. Increase in dielectric constant value is always accompanied with loss tangent peaks which signify the presence of the high temperature dielectric relaxation in YCZTO ceramic. The high temperature dielectric relaxation may arise from an extrinsic mechanism as well as the presence of defects or oxygen vacancies produced during sintering and cooling mechanisms. The presence of broad dielectric peak obtained for 100 Hz and 1 kHz below 350 K, which gets suppressed at higher frequency, confirms the presence of ferroelectric relaxor behaviour in the YCZTO. Such behaviour of a ferroelectric relaxor are usually characterized by diffuse phase transition and strong relaxational dispersion in dielectric constant and loss tangent ($\tan\delta$) which may be due to thermally activated relaxation.

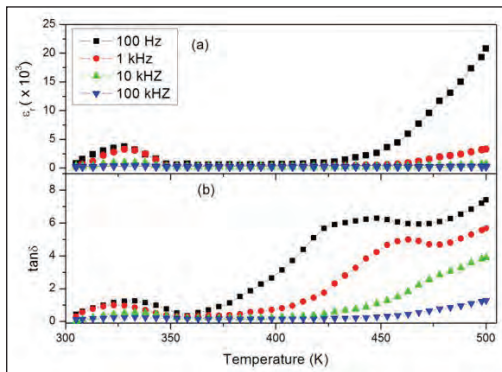


Fig. 2 Plots of (a) dielectric constant (ϵ_r) and (b) loss tangent ($\tan\delta$) vs temperature at different frequency for $\text{Y}_{2/3}\text{Cu}_{2.90}\text{Zn}_{0.10}\text{Ti}_4\text{O}_{12}$ (YCZTO) ceramic sintered at 950°C for 12h.

The same type of dispersion peak, below 350 K, was also observed in loss tangent vs temperature plot. The variation of dielectric loss ($\tan\delta$) as a function of temperature is shown Fig. 2(b). The dielectric loss for YCZTO ceramic at 350 K were found to be 0.47, 0.32, 0.10, and 0.02 at 0.1, 1, 10, 100 kHz, respectively which is fairly less the pure YCTO ceramic [17]. The presence of dispersion peaks in both the figures below 350 K and at lower frequencies confirmed the presence of Debye type relaxation behaviour in the ceramic. The presence of low frequency relaxation may be attributed to the occurrence of space charge polarization arising at the interface of grain and grain boundary which have a large difference in their electrical conductivity. It is clearly seen that $\tan\delta$ increases with increases with increases in temperature and increase smoothly and stepwise beyond 350 K. A rapid increase in $\tan\delta$ at higher temperatures may be due to exponential increase of conductivity with temperature as observed normally.

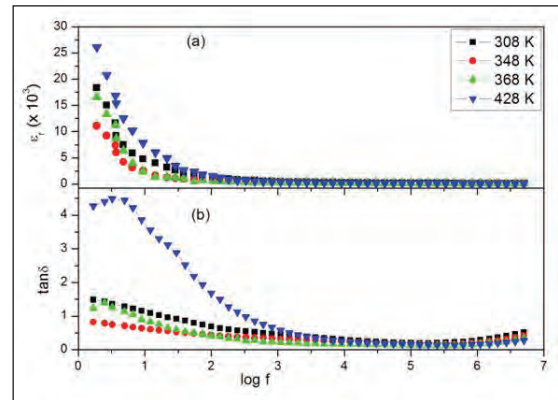


Fig. 3 Plots of (a) dielectric constant (ϵ_r) and (b) loss tangent ($\tan\delta$) vs frequency at different temperature for $\text{Y}_{2/3}\text{Cu}_{2.90}\text{Zn}_{0.10}\text{Ti}_4\text{O}_{12}$ (YCZTO) ceramic sintered at 950°C for 12h.

Fig. 3 illustrates the frequency dependence of dielectric constant (ϵ_r) and loss tangent ($\tan\delta$) of sintered YCTO ceramic at a few selected

temperature. The value of ϵ' for YCTFO ceramic was found to be 18390 at 308 K and 100 Hz while undoped YCTO ceramic, which is in fact undoped, exhibits the dielectric constant value equals to 8434 at 308 K and 100 Hz which is much higher than the value reported earlier [16-17]. Further, it can also be inferred that doping of YCTO at Cu²⁺ site by Zn²⁺ enhances the dielectric constant value more than twice its original value. It is quite significant from technological point of view. It is also clear from the Fig. 3 that the value of dielectric constant (ϵ_r) decreases steeply in lower frequency range whereas in higher frequency range (1 kHz -5 MHz) it decreases slowly. The decrease in dielectric constant with frequency may be due to the contribution of space charge accumulation at the interface which leads to polarization of the ionic medium and hence increases the value of ϵ_r . In high frequency regions, the periodic reversal of the field takes place so rapidly that there is no charge accumulation at the interface, resulting into a constant ϵ_r value [21].

Dielectric absorption in a material is usually characterized by loss tangent ($\tan\delta$). Fig. 3(b) shows the variation of loss tangent ($\tan\delta$) with frequency. It is evident from the figure that the value of $\tan\delta$ decreases with increase in frequency in lower frequency region while it decreases smoothly in higher frequency region. Relaxation peaks are also observed at all measured temperature. But it is more conspicuous in 368-428K temperature regimes. The dielectric loss of YCZTO ceramic was found to be 0.2 to 1.03 at 1 kHz from 308 to 428 K, however, it shows a high dielectric loss at higher temperature and low frequency region.

4. Conclusion

Nano-sized Y_{2/3}Cu_{2.90}Zn_{0.10}Ti₄O₁₂ (YCZTO) ceramic was synthesized by semi-wet route

using metal nitrate solution and solid TiO₂ powder. Single phase formation was confirmed by XRD along with the presence of secondary phase of CuO in minor. The particle size of the YCTO ceramic was found to be 56± 6 nm by XRD and 39 ± 6 nm by TEM studies which are in good agreement. sintered YCZTO pellets sintered at 950 °C for 12h exhibits considerably high dielectric constant $\epsilon_r \sim 2057$ at room temperature and 36,348 at 500K at 100 Hz frequency. Dielectric constant and loss tangent ($\tan\delta$) are temperature independent in higher frequency region but temperature dependent in low frequency region. Temperature dependent Relaxation phenomena in YCZTO ceramic was also observed at all measured temperature. Doping of YCTO at Cu²⁺ site by Zn²⁺ enhances the dielectric constant value more than twice its original value which is quite significant from technological point of view.

Reference

- [1] A. J. Moulson, J.M. Herbert. *Electroceramics*, 2nd ed. Wiley, England, 2003.
- [2] YuHongtao, LiuHanxing, HaoHua, GuoLiling, JinChengjun et al. *Appl. Phys. Lett.* 91 (2007) 222911.
- [3] M.A. Subramanian, D. Li, N. Duan, B.A. Reisner, A.W. Sleight, *J. Solid State. Chem.* 151 (2000) 323.
- [4] M.A. Subramanian, A.W. Sleight, *Solid State Sci.* 4 (2002) 347.
- [5] A.P. Ramirez, M.A. Subramanian, M. Gardel, G. Blumberg, D. Li, T. Vogt, S.M. Shapiro, *Solid State Comm.* 115 (2000) 217.
- [6] C.C. Homes, T. Vogt, S.M. Shapiro, S. Wakimoto, A.P. Ramirez, *Science* 293 (2001) 673;
- [7] D.C. Sinclair, T.B. Adams, F.D. Morrison, A.R. West, *Appl. Phys. Lett.* 80 (2002) 2153.

EFFECT OF ZINC DOPING AT Cu²⁺- SITE IN Y_{2/3}Cu₃Ti₄O₁₂ CERAMIC SYNTHESIZED BY SEMI-WET ROUTE

- [8] P. Lunkenheimer, V. Bobnar, A.V. Pronin, A.I. Ritus, A.A. Volkov, A. Loidl, Phys. Rev. B 66 (2002) 052105.
- [9] P. Lunkenheimer, R. Fichtl, S.G. Ebbinghaus, A. Loidl, Phys. Rev. B 70 (2004) 172102.
- [10] S.-Y. Chung, I.-D. Kim, S.-J.L. Kang, Nature Mat. 3 (2004) 774
- [11] Zhang L, Appl. Phys.Lett.87 (2005) 022907.
- [12] Mandal KD, RaiAlok Kumar, Kumar D, Parkash Om, J. Alloy Comp.478 (2009)771.
- [13] Rai AK, Mandal KD, Kumar D, Parkash O, J. Phys.Chem. Solids, 70 (2009) 834.
- [14] Adams TB, Sinclair DC, West AR, J Am Ceram Soc89(2006)2833.
- [15] Li M, Cai G, Zhang DF, Wang WY, Wang WJ, Chen XL, J. Appl. Phys. 104(2008)074107.
- [16] L. Pengfei, Y. Zupei, C. Xiaolian, L. Zonghua, J. Am. Ceram.Soc., 95(2012) 2218.
- [17] Sharma SunitaYadav Shiv Sundar, Singh M. M., Mandal K.D,J. Adv. Dielectr., 4 (2014)1450030-1-8 DOI: 10.1142/S2010135X14500301.
- [18] Cullity BD, Stock SR, Elements of X-ray Diffraction, Prentice Hall, New Jersey; Chapt1, 2001.
- [19] D.W. Kim, T.G. Kim, K.S. Hong, Mater. Res. Bull. 34 (1999) 771-781.
- [20] C.L. Huang, Y.C. Chen, Mater. Res. Bull. 37 (2002) 563-574.
- [21] B. Tareev, Physics of Dielectric Materials, Mir Publication, Moscow, (1975).